

UC San Diego

UC San Diego Electronic Theses and Dissertations

Title

Molecular-scale Simulations of Dynamic DNA nanostructures

Permalink

<https://escholarship.org/uc/item/56v7v2pq>

Author

Shi, Ze

Publication Date

2018

Peer reviewed|Thesis/dissertation

UNIVERSITY OF CALIFORNIA SAN DIEGO

Molecular-scale Simulations of Dynamic DNA nanostructures

A dissertation submitted in partial satisfaction of the
requirements for the degree
Doctor of Philosophy

in

Nanoengineering

by

Ze Shi

Committee in charge:

Professor Gaurav Arya, Chair
Professor Yi Chen
Professor Xiaohua Huang
Professor Ratnesh Lal
Professor Shyue Ping Ong

2018

Copyright
Ze Shi, 2018
All rights reserved.

The dissertation of Ze Shi is approved, and it is acceptable in quality and form for publication on microfilm and electronically:

Chair

University of California San Diego

2018

DEDICATION

This document is dedicated to my parents.

EPIGRAPH

Towering genius disdains a beaten path.

It seeks regions hitherto unexplored.

—Abraham Lincoln

TABLE OF CONTENTS

Signature Page		iii
Dedication		iv
Epigraph		v
Table of Contents		vi
List of Figures		ix
Acknowledgements		xi
Vita		xii
Abstract of the Dissertation		xiii
Chapter 1	Introduction	1
	1.1 Structural DNA nanotechnology	1
	1.2 Dynamic DNA nanostructures	4
	1.2.1 Stimuli based on DNA strands	4
	1.2.2 Other stimuli	5
	1.3 Computer-aided design	6
	1.3.1 Design interface	7
	1.3.2 Molecular simulation of DNA nanostructures	8
	1.4 Motivation and Outline of Dissertation	12
	1.5 References	14
Chapter 2	Conformational Dynamics of Mechanically-Compliant DNA Nanostructures from Coarse-Grained Molecular Dynamics Simulations	21
	2.1 Abstract	21
	2.2 Introduction	22
	2.3 Results	25
	2.3.1 Equilibrium conformations	25
	2.3.2 Structural stability	27
	2.3.3 Global motions	31
	2.3.4 Hinge angle predictions from force-balance	37
	2.4 Discussion	44
	2.5 Conclusions	48
	2.6 Methods	49
	2.6.1 Hinge designs	49
	2.6.2 Generation of initial hinge 3D conformations	49
	2.6.3 MD simulations	50

	2.6.4	Principal component analysis	50
	2.6.5	Large deformation behavior	50
	2.6.6	Force-deformation curves	51
	2.6.7	Simulation codes and data	51
	2.7	Acknowledgements	52
	2.8	Appendix	53
	2.9	References	61
Chapter 3		Cation-Activated Avidity for Rapid Reconfiguration of DNA Nanodevices	64
	3.1	Abstract	64
	3.2	Introduction	65
	3.3	Cation-Activated Actuation.	69
	3.4	Theoretical model of actuation response.	72
	3.5	Model Development	76
	3.6	Analysis of the Range and Sharpness of Actuation	79
	3.7	Acknowledgements	80
	3.8	References	81
Chapter 4		Free Energy Landscape of Cation-mediated Actuation of Overhang-modified DNA origami Nanostructures	85
	4.1	Abstract	85
	4.2	Introduction	86
	4.3	Results and discussion	90
		4.3.1 Effect of design parameters	102
		4.3.2 Zip mode and sheer mode	103
		4.3.3 Bare hinge and total free energy of the system	104
	4.4	Discussion	106
	4.5	Conclusion	108
	4.6	Methods	109
	4.7	Acknowledgements	110
	4.8	Appendix	111
	4.9	References	112
Chapter 5		Additional Studies	115
	5.1	Mechanics of the Holliday junction	115
	5.2	Modeling of a DNA crystal	119
	5.3	References	121
Chapter 6		Concluding remarks	122
	6.1	Summary	122
	6.2	Directions for future research	123
		6.2.1 Database of DNA mechanical components	123
		6.2.2 Free energy landscape of DNA overhang connections	124

6.2.3	Newer actuation strategies for DNA nanodevices	124
6.2.4	New mechanisms for mechanical DNA nanomachines . . .	124
6.2.5	Optimized design tools of dynamic DNA nanodevices . . .	124

LIST OF FIGURES

Figure 1.1:	DNA nanostructures based on 4-way junction	2
Figure 1.2:	DNA nanostructures based on DNA origami	3
Figure 1.3:	Dynamic DNA nanostructure	5
Figure 1.4:	OxDNA model	10
Figure 2.1:	Coarse-grained (CG) modeling of DNA origami hinges	23
Figure 2.2:	Hinge angles Φ predicted from MD simulations	26
Figure 2.3:	Stability of the origami hinges	28
Figure 2.4:	Local bending of the hinge joints	30
Figure 2.5:	Principal component analysis (PCA) of the five hinges	32
Figure 2.6:	Local bending of hinge joint	34
Figure 2.7:	Hinge bending behavior under large deformations	36
Figure 2.8:	Force-deformation behavior of the joint and the spring	39
Figure 2.9:	Additional relationships of the force-deformation curve	40
Figure 2.10:	Equilibrium hinge angle from force-deformation behavior	44
Figure 2.11:	Normalized distributions of hinge angles	53
Figure 2.12:	Equilibrium hinge angles predicted with CanDo	54
Figure 2.13:	Representative snapshot of the joint and the springs	54
Figure 2.14:	Root mean square fluctuations of hinge	55
Figure 2.15:	DNA-backbone representation of hinges	55
Figure 2.16:	Distance between adjacent bases of the staple strands	56
Figure 2.17:	Correlation between dynamic modes of hinge	57
Figure 2.18:	Average structure of the hinge	57
Figure 2.19:	Electrostatic repulsion energy of hinge	58
Figure 2.20:	CaDNAno design of the 0b hinge	58
Figure 2.21:	CaDNAno design of the 11b hinge	58
Figure 2.22:	CaDNAno design of the 32b hinge	59
Figure 2.23:	CaDNAno design of the 53b hinge	59
Figure 2.24:	CaDNAno design of the 74b hinge	59
Figure 2.25:	Hinge angle distribution under different salt concentrations	60
Figure 2.26:	Correlation time of the hinge angle	61
Figure 3.1:	Ion-activated reconfigurable DNA nanostructures	69
Figure 3.2:	Experimental measured actuation responses of hinge	70
Figure 3.3:	Model fits to experimental actuation response curves	73
Figure 3.4:	Model fits to actuation responses obtained with NaCl	74
Figure 3.5:	Cumulative angular distribution for Hinge1	76
Figure 4.1:	DNA origami hinge design	88
Figure 4.2:	Computational strategy for hinge actuation free energies	92
Figure 4.3:	Representative free energy landscape of a single overhang pair	94

Figure 4.4:	Total free energy landscape of overhangs	95
Figure 4.5:	Free energy landscape under different ion concentrations	96
Figure 4.6:	Free energy landscape under different confinements	99
Figure 4.7:	Interaction probability under different confinements	101
Figure 4.8:	Free energy landscape for different overhang sequences	102
Figure 4.9:	Free energy landscape of two different binding modes	104
Figure 4.10:	Free energy landscape of the bare hinge	105
Figure 4.11:	Total free energy of the system	106
Figure 4.12:	Correlation between hinge angle and distance	111
Figure 4.13:	Relaxation time of the bare hinge	111
Figure 4.14:	Free energy landscape of overhangs under 0.4M and 1.2M	112
Figure 5.1:	Stretching the Holliday junction	116
Figure 5.2:	Potential of mean force and snapshots of the Holliday junction	117
Figure 5.3:	H-bond binding rate in the stretching process	118
Figure 5.4:	Assembly of DNA tiles	120
Figure 5.5:	H-bonds in DNA crystal	121

ACKNOWLEDGEMENTS

I am greatly indebted to Dr. Gaurav Arya for his guidance and support, and I sincerely thank Dr. Yi Chen, Dr. Xiaohua Huang, Dr. Ratnesh Lal and Dr. Shyue Ping Ong for serving on my doctoral committee.

Thanks to our collaborator Dr. Carlos Castro, Alexander E. Marras, and Lifeng Zhou for providing detailed information of their nanostructures and countless help on my research project.

Thanks to Hanmei Tang for giving inspirations on my research project and her companion in improving programming skill.

Thanks to Reem Mokhtar for the pleasant conversations on FNANO2018, which is the most precious memory in my Ph.D. experience.

I also thank the countless other people who helped me in one way or another throughout my Ph.D. experience at UC San Diego. Among these people I recall (in no special order): Dario Meluzzi, Murthy R. Chaitanya, Amy D. Migliori, Gi-Moon Nam, Tsungyeh Tang, Stephanie Lauback and certainly more.

Chapter 2, in full, is a reprint of the material as it appears in ACS Nano 2017. Shi, Ze; Arya, Castro, Carlos E., Gaurav, ACS Publication, 2017. The dissertation author was the primary investigator and author of this paper.

Chapter 3, in full, is a reprint of the material as it appears in ACS Nano 2018. Marras, Alexander E.; Shi, Ze; Lindell, Michael G.; Patton, Randy A.; Huang, Chao-Min; Zhou, Lifeng; Su, Hai-Jun; Arya, Gaurav; Castro, Carlos E., ACS Publication 2018. The dissertation author was one of the primary investigators and authors of this paper.

Chapter 4, in full is currently being prepared for submission for publication of the material. Shi, Ze; Arya, Gaurav. The dissertation author was the primary investigator and author of this material.

VITA

2012 B. S. in Material Science, Fudan University

2014-2018 Graduate Research Assistant, University of California, San Diego

2018 Ph. D. in Nanoengineering, University of California, San Diego

PUBLICATIONS

Shi, Ze; Castro, Carlos E.; Arya, G. “Conformational Dynamics of Mechanically Compliant DNA Nanostructures from Coarse-Grained Molecular Dynamics Simulations”. *ACS Nano*, 11, 2017

Marras, Alexander E.; Shi, Ze; Lindell, Michael G. III; Patton, Randy A.; Huang, Chao-Min; Zhou, Lifeng; Su, Hai-Jun; Arya, Gaurav; Castro, Carlos E.; “Cation-Activated Avidity for Rapid Reconfiguration of DNA Nanodevices”. *ACS Nano*, in press, 2018

ABSTRACT OF THE DISSERTATION

Molecular-scale Simulations of Dynamic DNA nanostructures

by

Ze Shi

Doctor of Philosophy in Nanoengineering

University of California San Diego, 2018

Professor Gaurav Arya, Chair

Structural DNA nanotechnology, the assembly of rigid 3D structures of complex yet precise geometries, has recently been used to design dynamic, mechanically-compliant nanostructures with tunable equilibrium conformations and conformational distributions. Introduction of additional stimuli-responsive behavior in such dynamic nanostructures should further widen the possible applications of DNA nanotechnology. The overarching goal of this dissertation is to explore the potential of coarse-grained molecular modeling and simulations as a design tool for predicting the mechanical properties, the free energy landscape, and stimuli-responsive behavior of dynamic DNA nanostructures. In the first part of this dissertation, coarse-grained molecular dynamics simulations are used to provide insights into the conformational dynamics of

a set of mechanically compliant DNA nanostructures, namely, DNA origami hinges. An approach is also proposed for rapidly predicting equilibrium hinge angles from individual force-deformation behaviors of their single- and double-stranded DNA components. In the second part, molecular basis for the mechanism of salt-actuation of such DNA hinges is provided by computing their free energy landscape with respect to the hinge angle using a novel methodology. A simple analytical statistical-mechanical model is also introduced to model the actuation response curves obtained experimentally. This work provides some of the first molecular-scale insights into the conformational dynamics and ion-activated actuation of mechanically compliant DNA nanostructures, which should help guide the design and optimization of new nanodevices.

Chapter 1

Introduction

1.1 Structural DNA nanotechnology

In the early 1980s, Nadrian Seeman proposed the concept of the 4-way junction of DNA (1) that would spawn the field of DNA nanotechnology (Figure 1.1a). Indeed, because of its many advantageous features including programmability, self-assembly, and molecular recognition, DNA serves as a promising building block for nanofabrication. Based on such DNA 4-way junctions, a variety of more complex nanostructures including DNA cube (2) (Figure 1.1b), double-crossover tile-based 2D DNA crystal (3) (Figure 1.1c), triple-crossover tile-based 2D DNA crystal and DNA nanotube (4), 3D DNA crystals (5) (Figure 1.1d), DNA sheets based on programmed self-assembly (6), and DNA octahedron (7) (Figure 1.1e) have been fabricated. Generally, the only design input in such DNA nanostructures is the sequence of DNA strands used for hybridizing them and folding the resulting skeleton into the desired geometry. For small structures and relatively large structures self-assembled from small DNA motifs, the sequence design is fairly intuitive. However, it becomes tedious to design large and complicated structures with such a basic design strategy.

Therefore, towards achieving more programmable large structures, a breakthrough design

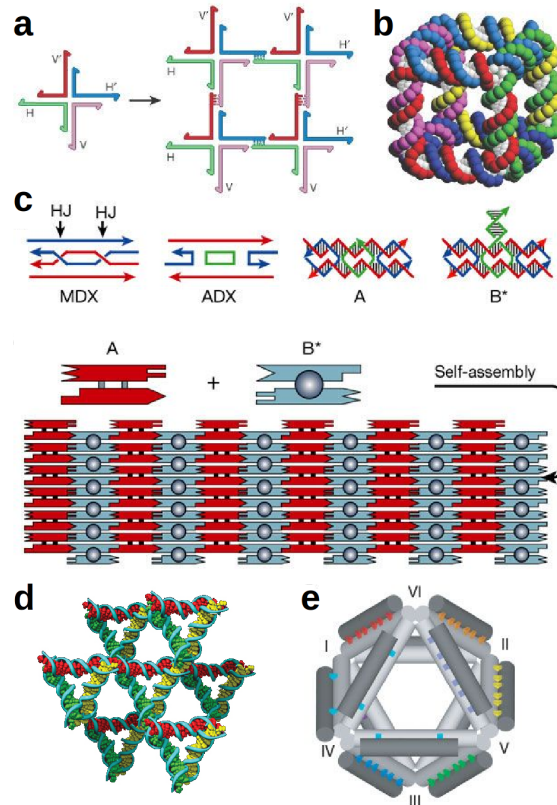


Figure 1.1: DNA nanostructures based on 4-way junction. **a:**4-way junction of DNA with sticky-ends (1). **b:** DNA cube (2). **c:**2D DNA crystal, adapted from (5), with permission from Nature Publishing Group. **a–c** are adapted from (8), with permission from Nature Publishing Group. **d:**3D DNA octahedron, adapted from (5), with permission from Nature Publishing Group.**e:**DNA octahedron, adapted from (7), with permission from Nature Publishing Group.

strategy, DNA origami, was proposed by Paul Rothemund in 2006 (9) (Figure 1.2a). In DNA origami, a long scaffold strand passing through the entire structure is employed and a periodic array of staple strands are incorporated to connect DNA duplex bundles. Instead of decomposing the sequence design into design of binding sites on DNA tiles, the DNA origami strategy simplified the sequence design to the design of the connections between DNA duplex strands, and converting them to space relationships between different parts of the scaffold strands. In this way, researchers could design more complex structures compared to structure designs based on DNA tiles. In the past decade, structures including DNA origami sheets (9; 10) (Figure 1.2b), DNA origami capsules (11; 12; 13) (Figure 1.2c), lattice-based 2.5D DNA origami (14) (Figure 1.2d) and its

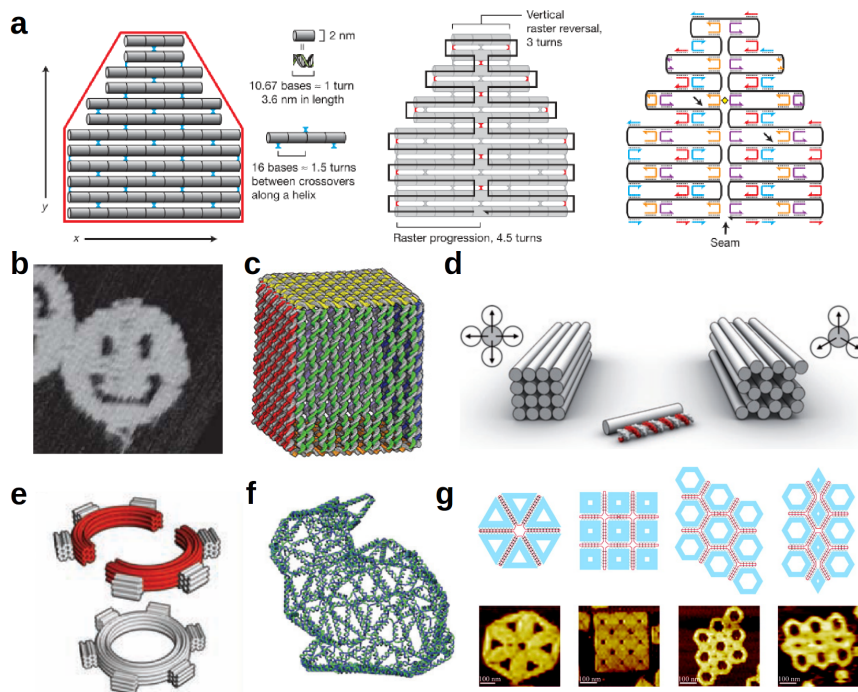


Figure 1.2: DNA nanostructures based on DNA origami. **a:** Design of DNA origami (9), adapted from (9), with permission from Nature Publishing Group. **b:** 2D DNA origami sheet (9), adapted from (9), with permission from Nature Publishing Group. **c:** DNA origami capsules, (11), adapted from (11), with permission from Nature Publishing Group. **d:** 2.5D DNA crystal (14), adapted from (23), with permission from Nature Publishing Group. **e:** twisted 2.5D DNA origami structure (15), adapted from (15), with permission from American Association for the Advancement of Science. **f:** wire-frame-based 3D DNA origami shells (16), adapted from (16), with permission from Nature Publishing Group. **g:** superorigami (19), adapted from (19), with permission from American Chemical Society.

modified version with curvature through insertion and deletion of DNA bases (15) (Figure 1.2e), wire-frame-based 3D DNA origami shells (16; 17; 18; 13) (Figure 1.2f), and superorigami (19) (Figure 1.2g). In practice, the size of DNA origami nanostructures is always limited by the length of the scaffold; Recent efforts (20; 21; 22) on extending the length of scaffolds have enabled the bottom-up fabrication of micron-sized DNA structures, though this strategy also introduces a larger number of defects into the structure.

Apart from structures fabricated according to the strategies introduced above, researchers have also developed variants or combinations of these methods as a possible way of fabricating

large DNA structures, such as 2D origami lattice (24), DNA brick crystal (25), and self-assembly through staking interaction between blunt ends exploiting weak interactions in DNA self-assembly (26; 27).

1.2 Dynamic DNA nanostructures

Apart from static structures fabricated with the above mentioned design strategies, dynamic DNA nanostructures are also coming into the forefront due to the many additional applications they may potentially promise, for instance in sensing and actuation, drug delivery, robotics, and nanomanufacturing. Designs of dynamic nanostructures can be put into several categories according to the stimuli that induces the conformational change or motion in the DNA nanostructure.

1.2.1 Stimuli based on DNA strands

Most dynamic DNA nanodevices are based on DNA-DNA interactions, especially small DNA structures like DNA walkers (28; 29; 30; 31; 32). The toe-hold mediated strand displacement (TMSD) method (33) (Figure 1.3a), which is a base-pairing based method using externally added DNA strands to change the hybridization status of DNA within the DNA structure, is one of the main actuation methods used for actuating dynamic DNA nanostructures. Apart from hybridizing and dissociating two DNA strands, TMSD also enables conformation and stiffness changes of DNA strands in DNA origami structures.

By controlling the hybridization states of certain DNA strands with TMSD, a series of two-state dynamic DNA devices have been achieved, such as DNA containers (34; 35; 36) (Figure 1.3b), rotary DNA origami device (37), DNA origami beacon (38), and DNA origami machines capable of large conformational changes (39; 40; 41; 42; 43; 44; 45; 46; 47)(Figure 1.3c and d). Such conformation changes can then be translated into linear or rotary motion of DNA

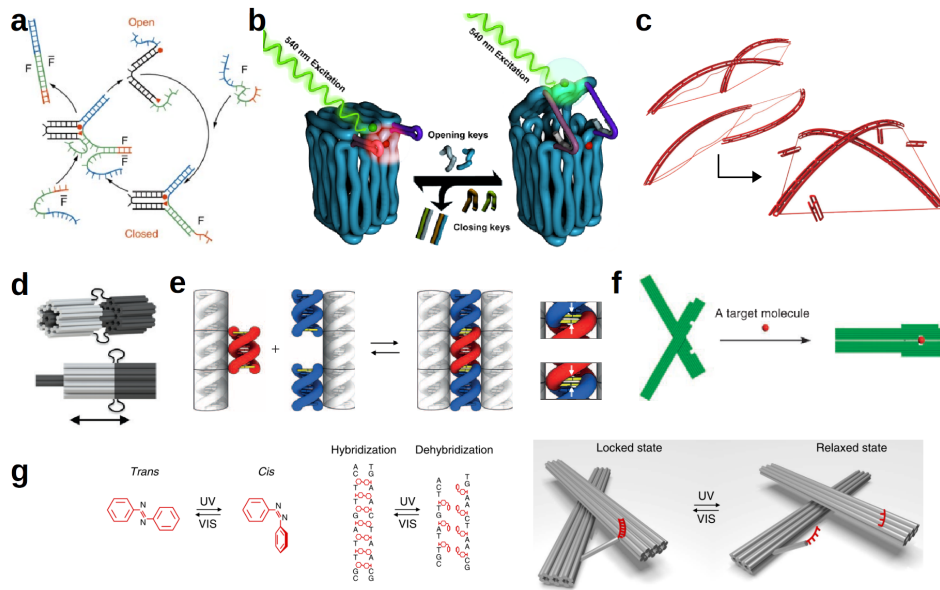


Figure 1.3: Dynamic DNA nanostructures. **a:**TMSD method (33), adapted from (33), with permission from Nature Publishing Group. **b:** Two-state DNA container (35), adapted from (35), with permission from American Chemical Society. **c:**DNA tensegrity structure capable of large conformational change (39), adapted from (39), with permission from Nature Publishing Group. **d:** DNA pinston (40), adapted from (40), with permission from American Chemical Society. **e:** DNA nanostructure actuated by ion concentration (43), adapted from (43), with permission from American Association for the Advancement of Science. **f:** DNA nanostructure actuated by aptamers targeting (44), adapted from (44), with permission from Nature Publishing Group. **g:** DNA nanostructure actuated by light stimuli (50), adapted from (50), with permission from Nature Publishing Group.

devices through clever strategies involving precisely placed DNA binding sites on appropriate templates such DNA origami. DNA origami has provided an excellent template for controlling the direction and movement of such dynamic nanostructures (48; 46; 43). Recently, Ketterer *et al* (49) also introduced a tight-fitting DNA components-based rotary apparatus with random motion.

1.2.2 Other stimuli

For stimuli involving DNA strands, a hybridization and dissociation process is always required for actuating the DNA structures. Therefore, two main shortcomings of this method are the relative long time scales of actuation and waste strands generated in such process. Recently,

weaker interactions such as base stacking of blunt-ended double-stranded DNA segments have been used to latch components together in a tunable manner based on ion concentration (43) (Figure 1.3e). Apart from the effect on base stacking, varying effects of ion concentration on the stability of Hoogsteen interactions in triplex DNA (51) and on the hybridization energy of short DNA strands (52) have also been considered as actuation strategies for dynamic DNA nanostructures.

Apart from DNA-DNA interactions, interactions between DNA and other molecules have also been considered for actuation (Figure 1.3f); These include binding of small moieties like miRNA, G-quadruplexes, and ATP molecules (44; 53), DNA aptamers targeting (44; 53; 54; 55) and protein-protein interactions (56; 57). In addition, stimuli such as light (58; 50) (Figure 1.3g), as well as electrical (59) or magnetic (60) actuation methods have also been utilized, which have the added advantage of being noninvasive.

For most of these dynamic structures, the mechanical properties of DNA are extremely important in determining the magnitude of conformational fluctuations or the motion path of such nanostructures. To this end, several studies have begun to examine the mechanical properties of DNA components based on classical mechanics theories, e.g, Euler elastic beams (61; 62). However, analytical models based on classical mechanics have various limitations as described further below, and therefore, computer-aided design strategies incorporating more detailed biophysics of DNA structures may provide more accurate design approaches.

1.3 Computer-aided design

Due to the complexity of assigning sequence to DNA strands that fold uniquely into the desired geometry and topology, the design tools are typically developed at the same time a new design strategy of DNA nanostructures is proposed. The computer-aided design tools generally have two functions: interpretation of a high-level design input into DNA sequence, and prediction

of various properties of the designed structure (e.g., shape, stability) to give feedback on the input design. The first function always updates with the development of a new structural design strategy, while the second one is typically a simplified version of a computer simulation of the input structure.

1.3.1 Design interface

The design interface, usually a software package, is always based on implementing design rules using some type of algorithm that operates on the input design parameters. In DNA nanostructures, the input design parameters, in general, are the shape and function of the structures.

After Nadrian Seeman proposed the four-way junctions, a design tool named GIDEON (63) was developed in 2006 by his lab. The package has a simple interface, and simple design rules including hybridization of double-stranded DNA and assembly of four-way junctions. What GIDEON provides is an interface necessary for bottom-up design of simple wire-frame and tile-based DNA nanostructures.

After Paul Rothemund invented the DNA origami design strategy, Andersen *et al* (64) developed the SARSE toolbox to provide an interface for designing 2D DNA origami structures. The top-down concept of a structure shape input is incorporated in this package as it accepts a bitmap file input for the 2D shape of targeted structure. Furthermore, this package also provides an atomic structure output, which can be directly used to perform all-atom simulations.

caDNAno developed by Douglas *et al.* (14) is a widely used bottom-up design package for 3D DNA origami design. This package is based on a 2.5 dimension lattice frame to define the helix bundle and highlight possible connection points. Although caDNAno offers enough freedom within the DNA origami lattice framework for designing nonlinear structures such as circular gears, it is still inconvenient for designing complex 3D structures because of the 2.5D strategy inherent in their source code.

Tiamat (65) developed by Hao Yan's lab is essentially an updated version of GIDEON. It offers a platform for freely drawn small DNA structure design.

VHelix (16) is a package developed by Högberg lab with a top-down method that converts a 3D design input into a DNA mesh grid. Compared to SARSE, the design input is evolved from 2D to 3D and works as a plug-in of Autodesk Maya, which would be an ideal design input for complex structures as it takes the advantage of 3D modeling platform. However, the design strategy is limited to polyhedral 3D mesh, which would not be suitable for most applications of DNA origami. Combining different design strategies into this package could be a potential improvement of the package.

DAEDALUS (13) is similar to vHelix, but the design strategy is more optimized. Also, it takes a CAD file as an input, which is closer to macroscopic structure design. However, this approach still suffers from the same limitations vHelix, that is, it only creates 3D DNA meshes instead of a combination of bricks, shells and wire frames. For designs with other applications like drug delivery or mechanical objects, DAEDALUS is not the best choice.

Apart from design strategies, simple thermodynamics relaxation procedure for obtaining rough predictions of the 3D shape of the structures are also typically incorporated in many design interfaces. For caDNAo, because of the relatively large structure and the inconvenience of 2.5D lattice structure, a simulation package implementing a finite-elements model, CanDo (23; 66) has been developed together with the design interface. The simple relaxation simulation incorporated in the design tools will give a gist of the shape and the structure of the design input, but for molecular- and energetics-level understanding of DNA nanostructures, performing computational simulations at different level of detail would be an ideal choice.

1.3.2 Molecular simulation of DNA nanostructures

In the past, the nearest-neighbor model of DNA base-pairing (67) has been used to predict the native secondary structure, and the associated free energy, of DNA nanostructures or their

motifs (7; 68). To predict 3D tertiary conformations, methods have been developed that impose geometrical restraints on DNA nucleotides which are minimized using relaxation algorithms to yield conformations with minimal mechanical, planar, and torsional strains (63). Continuum mechanics formulations treating DNA base-pairs as finite elements of an elastic rod, connections between dsDNA helices as rigid crossovers, and ssDNA components as nonlinear springs have also been developed to predict conformations of DNA origami structures designed with typical honeycomb or square lattice cross-sections. (23; 66). Recent extensions to this approach (69; 70) account for lattice-free structures with multiway junctions, topologically-closed structures, and Brownian dynamics of the structures.

While these continuum-mechanics-based approaches enable rapid predictions of the global conformations of rigid to semi-flexible structures, they do not possess the resolution required to capture molecular-scale effects, such as inelastic deformation and partial unzipping of dsDNA components, and conformational flexibility, steric interactions, and secondary-structure formation of ssDNA components. Such effects likely become important in dynamic structures like the DNA hinges discussed earlier that contain long, flexible ssDNA connections and strongly deformed dsDNA components. These approaches are also unable to model structures with complex energy landscapes that exhibit multiple stable conformational states. Lastly, the approaches cannot capture structural “dynamics”, that is, the real-time molecular-scale motions accompanying conformational fluctuations and transitions across states. While these motions are mostly restricted to near-harmonic oscillations in the case of rigid structures, they may become large and lead to more complex, coupled motions in compliant structures

All-atom models provide an ideal resolution for capturing the conformation and mechanics of the single- and double-stranded components of DNA nanostructures, and molecular dynamics (MD) simulations provide a powerful approach for simulating their conformational dynamics. Indeed, all-atom MD simulations has increasingly being used to study DNA nanostructures (72; 73; 74; 70; 75; 76; 77). However, many of these structures contain thousands of nucleotides,

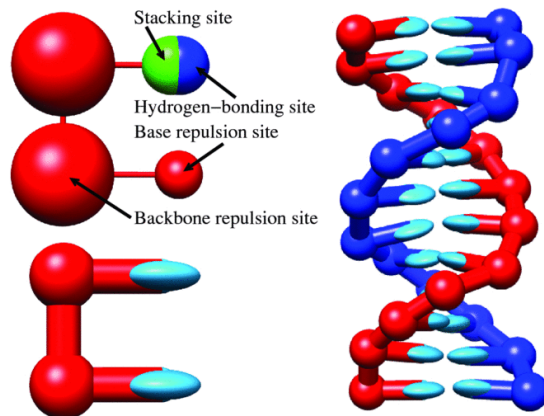


Figure 1.4: Model interaction sites and double helix structure of oxDNA. Adapted from (71), with permission from American Institute of Physics.

which equates to simulation systems containing millions of atoms in explicit solvent. Despite rapid advances in computing power, simulating such structures with all-atom models remains highly computationally demanding.

To overcome this challenge, a number of coarse-grained (CG) models have been developed that provide simpler representations of DNA while still retaining enough details to reproduce its key properties (78). *OxDNA* (71) is one such CG model that was recently developed specifically for DNA nanotechnology and reproduces various thermodynamic and conformational properties of ssDNA and dsDNA (Figure 1.4). This model represents each nucleotide as a rigid body with three interaction sites and accounts for Watson-Crick base pairing, base stacking, excluded volume, and backbone connectivity. *OxDNA* has already been successfully used to study a variety of DNA nanostructures (79; 80; 81; 82; 83; 84; 85; 86), including those built *via* DNA origami (87; 88; 89).

In this model, each DNA strand is treated as a chain of rigid bodies representing nucleotides, and the surrounding solvent and ions are treated implicitly. Each nucleotide is represented by three interaction sites—one site for each pair of phosphate and sugar groups and two sites for each base. The noncollinearity of the three interaction sites enables the model to capture the asymmetric shape of the dsDNA helix with distinct major and minor grooves. Each nucleotide

is also represented by a vector perpendicular to the notional plane of each base whose direction enables the model to capture the orientational dependence of base-stacking and Watson-Crick base-pairing interactions.

The total potential energy of a multi-strand system is given by the sum of eight pairwise interaction terms:

$$\begin{aligned}
 U_{\text{tot}} = & \sum_{\text{nearest neighbors}} (U_{\text{bb}} + U_{\text{stack}} + U'_{\text{ev}}) \\
 & + \sum_{\text{other pairs}} (U_{\text{HB}} + U_{\text{cs}} + U_{\text{ev}} + U_{\text{coax}} + U_{\text{DH}}), \quad (1.1)
 \end{aligned}$$

where the first sum accounts for interactions between *adjacent* nucleotides on the same strand, and contains U_{bb} , U_{stack} , and U'_{ev} terms that describe the connectivity between adjacent backbone sites, stacking interactions across neighboring base sites, and excluded volume interactions between neighboring nucleotide sites, respectively. The second sum accounts for interactions between *all other* pairs of nucleotides in which U_{HB} describes hydrogen-bonding interactions between complementary bases, U_{cs} describes cross-stacking interactions between bases on opposite DNA strands, U_{ev} describes excluded volume interactions, U_{coax} describes coaxial stacking of non-neighboring bases on the same strand, and U_{DH} describes salt-screened electrostatic interactions between non-neighboring backbone sites. All interaction potentials, except the excluded volume, backbone, and electrostatic terms, depend on the relative orientations of the nucleotides, in addition to depending on distances between interaction sites. The interaction-potential parameters, such as the location and depth of energy minima, force constants, and charges, were fitted to reproduce experimentally measured properties of DNA: the stacking transition of ssDNA; length- and salt-dependent melting transition curves and melting temperature of short dsDNA duplexes; persistence lengths of ssDNA and dsDNA; and elastic torsional and stretching moduli of dsDNA. Further details on model development, parameterization, and application are provided elsewhere (71; 90; 87).

1.4 Motivation and Outline of Dissertation

As discussed above, the past few decades have witnessed a rapid growth in the field of DNA nanotechnology, both in the development of new design strategies to increase the size and complexity of DNA nanostructures and in the development of automated design software. One of the main visions of this field is to create dynamic, functional devices that mimic the exquisite complexity and efficiency of biomolecular machines that exist in nature (e.g., polymerase, ribosomes), but also macroscopic machines that are part of our daily lives (e.g., automobile engine). The work in this dissertation focuses on an emerging class of dynamic, mechanically compliant DNA nanostructures developed over the last few years (91; 47; 46; 92; 40; 39).

These structures exploit differences in the mechanical properties of single- and double-stranded DNA, as well as bundles of interconnected double-stranded DNA helices to create mimics of joints and links found in macroscopic machines. Some unique aspects of these devices are the large fluctuations that they exhibit about an equilibrium conformation, and high tunability of their equilibrium conformation as well as the size of these fluctuations. The fact that these structures exhibit fluctuations typically in a specific direction makes them useful for mechanical sensing and actuation. However, as discussed above, current design tools are either not well suited to modeling such dynamic and compliant nanostructures, or are limited to the modeling small-scale hybridization processes (93).

One of the goals of this dissertation is to investigate the viability of molecular-scale modeling and simulations in reproducing the conformational dynamics of such dynamic, mechanically-compliant structures and to provide insights into their mechanical properties. Because of the relatively large size of these nanostructures, a coarse-grained representation of these structures is required. While a rigorously-developed coarse-grained model of DNA nanostructures has recently become available, this model has not so far been tested on large, mechanically compliant DNA nanostructures.

Another goal is to develop simple design rules based on molecular-scale and statistical models for predicting the conformational dynamics of these nanostructures and their actuation response to potential stimuli such as ion concentration. The sample structures studied in this dissertation could be also counted as part of a database of dynamic DNA nanostructure designs, which could in the future serve as a strong design tool for complex mechanical nanodevices made from DNA.

The rest of this dissertation is organized as follows. Chapter 2 investigates the potential of predicting the conformational dynamics of a set of DNA origami hinge designs with coarse-grained modeling and simulations. A force-balanced method is also proposed to enable rapid prediction of such dynamics for studying large sets of designs in a high-throughput manner.

Chapter 3 introduces a modified DNA origami hinge that can be actuated by changes in ion concentration. A simple statistical mechanical model is described to explain the actuation response profiles obtained experimentally and to elucidate the role of various hinge design parameters.

The analytical model developed above, however, involves two fitting parameters, which makes the model less predictive. Therefore, in Chapter 4, a thorough study of the free energy landscape of the modified DNA origami hinge is presented, yielding important molecular-level understanding of the behavior of the hinges under different salt conditions and also providing guidance for design optimization for possible future applications.

Apart from these research projects on the DNA origami hinges, other systems studied during my graduate study are presented in Chapter 5, including stretching mechanics of the Holliday junction in a DNA origami and all-atom molecular dynamics simulation of a DNA crystal.

Finally, Chapter 6 summarizes the work presented in this dissertation and provides several possible directions for future research.

1.5 References

- [1] N. C. Seeman, “Nucleic acid junctions and lattices,” *J. Theor. Biol.*, vol. 99, no. 2, pp. 237–247, 1982.
- [2] J. H. Chen and N. C. Seeman, “Synthesis from DNA of a molecule with the connectivity of a cube.,” *Nature*, vol. 350, pp. 631–633, apr 1991.
- [3] E. Winfree, F. Liu, L. A. Wenzler, and N. C. Seeman, “Design and self-assembly of two-dimensional DNA crystals,” *Nature*, vol. 394, no. 6693, pp. 539–544, 1998.
- [4] D. Liu, S. H. Park, J. H. Reif, and T. H. LaBean, “DNA nanotubes self-assembled from triple-crossover tiles as templates for conductive nanowires.,” *Proc. Natl. Acad. Sci. U. S. A.*, vol. 101, no. 3, pp. 717–722, 2004.
- [5] J. Zheng, J. J. Birktoft, Y. Chen, T. Wang, R. Sha, P. E. Constantinou, S. L. Ginell, C. Mao, and N. C. Seeman, “From molecular to macroscopic via the rational design of a self-assembled 3D DNA crystal,” *Nature*, vol. 461, pp. 74–77, sep 2009.
- [6] K. Fujibayashi, R. Hariadi, S. H. Park, E. Winfree, and S. Murata, “Toward Reliable Algorithmic Self-Assembly of DNA Tiles: A Fixed-Width Cellular Automaton Pattern,” *Nano Lett.*, vol. 8, pp. 1791–1797, jul 2008.
- [7] W. M. Shih, J. D. Quispe, and G. F. Joyce, “A 1.7-kilobase single-stranded DNA that folds into a nanoscale octahedron.,” *Nature*, vol. 427, no. 6975, pp. 618–621, 2004.
- [8] N. C. Seeman, “DNA in a material world,” *Nature*, vol. 421, no. 6921, pp. 427–431, 2003.
- [9] P. W. K. Rothemund, “Folding DNA to Create Nanoscale Shapes and Patterns.,” *Nature*, vol. 440, no. 7082, pp. 297–302, 2006.
- [10] B. Wei, M. Dai, and P. Yin, “Complex shapes self-assembled from single-stranded DNA tiles,” *Nature*, vol. 485, pp. 623–626, may 2012.
- [11] A. Kuzuya and M. Komiyama, “Design and construction of a box-shaped 3D-DNA origami,” *Chem. Commun.*, vol. 0, p. 4182, jul 2009.
- [12] Y. Ke, J. Sharma, M. Liu, K. Jahn, Y. Liu, and H. Yan, “Scaffolded DNA Origami of a DNA Tetrahedron Molecular Container,” *Nano Lett.*, vol. 9, pp. 2445–2447, jun 2009.
- [13] R. Veneziano, S. Ratanalert, K. Zhang, F. Zhang, H. Yan, W. Chiu, and M. Bathe, “Designer nanoscale DNA assemblies programmed from the top down.,” *Science (80-.)*, vol. 352, p. 1534, jun 2016.
- [14] S. M. Douglas, A. H. Marblestone, S. Teerapittayanon, A. Vazquez, G. M. Church, and W. M. Shih, “Rapid prototyping of 3D DNA-origami shapes with caDNAo,” *Nucleic Acids Res.*, vol. 37, no. 15, pp. 5001–5006, 2009.

- [15] H. Dietz, S. M. Douglas, and W. M. Shih, "Folding DNA into twisted and curved nanoscale shapes.," *Science*, vol. 325, no. 5941, pp. 725–730, 2009.
- [16] E. Benson, A. Mohammed, J. Gardell, S. Masich, E. Czeizler, P. Orponen, and B. Högberg, "DNA rendering of polyhedral meshes at the nanoscale," *Nature*, vol. 523, no. 7561, pp. 441–444, 2015.
- [17] D. Han, S. Pal, J. Nangreave, Z. Deng, Y. Liu, and H. Yan, "DNA origami with complex curvatures in three-dimensional space.," *Science*, vol. 332, no. 6027, pp. 342–346, 2011.
- [18] D. Han, S. Pal, Y. Yang, S. Jiang, J. Nangreave, Y. Liu, and H. Yan, "DNA Gridiron Nanostructures Based on Four-Arm Junctions," *Science (80-.)*, vol. 339, pp. 1412–1415, mar 2013.
- [19] Z. Zhao, Y. Liu, and H. Yan, "Organizing DNA origami tiles into larger structures using preformed scaffold frames," *Nano Lett.*, vol. 11, no. 7, pp. 2997–3002, 2011.
- [20] H. Zhang, J. Chao, D. Pan, H. Liu, Q. Huang, and C. Fan, "Folding super-sized DNA origami with scaffold strands from long-range PCR," *Chem. Commun.*, vol. 48, p. 6405, may 2012.
- [21] B. Kick, F. Praetorius, H. Dietz, and D. Weuster-Botz, "Efficient Production of Single-Stranded Phage DNA as Scaffolds for DNA Origami," *Nano Lett.*, vol. 15, pp. 4672–4676, jul 2015.
- [22] A. N. Marchi, I. Saaem, B. N. Vogen, S. Brown, and T. H. LaBean, "Toward Larger DNA Origami," *Nano Lett.*, vol. 14, pp. 5740–5747, oct 2014.
- [23] C. E. Castro, F. Kilchherr, D.-N. Kim, E. L. Shiao, T. Wauer, P. Wortmann, M. Bathe, and H. Dietz, "A primer to scaffolded DNA origami.," *Nat. Methods*, vol. 8, no. 3, pp. 221–229, 2011.
- [24] W. Liu, H. Zhong, R. Wang, and N. C. Seeman, "Crystalline two-dimensional DNA-origami arrays," *Angew. Chemie - Int. Ed.*, vol. 50, no. 1, pp. 264–267, 2011.
- [25] Y. Ke, L. L. Ong, W. Sun, J. Song, M. Dong, W. M. Shih, and P. Yin, "DNA brick crystals with prescribed depths," *Nat. Chem.*, vol. 6, no. 11, pp. 994–1002, 2014.
- [26] R. Iinuma, Y. Ke, R. Jungmann, T. Schlichthaerle, and J. B. Woehrstein, "Polyhedra Self-Assembled from DNATripods and Characterized with 3DDNA-PAINT," *Science (80-.)*, no. March, pp. 1–9, 2014.
- [27] S. Woo and P. W. K. Rothemund, "Programmable molecular recognition based on the geometry of DNA nanostructures," *Nat. Chem.*, vol. 3, pp. 620–627, aug 2011.
- [28] J. Bath and A. J. A. J. Turberfield, "DNA Nanomachines," *Nat. Nanotechnol.*, vol. 2, no. Box 1, p. 275, 2007.

- [29] H. Gu, J. Chao, S. J. Xiao, and N. C. Seeman, “A Proximity-Based Programmable DNA Nanoscale Assembly Line,” *Nature*, vol. 465, p. 202, 2010.
- [30] T. Omabegho, R. Sha, and N. C. Seeman, “A Bipedal DNA Brownian Motor with Coordinated Legs,” *Science (80-.)*, vol. 324, pp. 67–71, apr 2009.
- [31] J. Pan, F. Li, T.-G. Cha, H. Chen, and J. H. Choi, “Recent progress on DNA based walkers,” *Curr. Opin. Biotechnol.*, vol. 34, pp. 56–64, aug 2015.
- [32] A. J. Thubagere, W. Li, R. F. Johnson, Z. Chen, S. Doroudi, Y. L. Lee, G. Izatt, S. Wittman, N. Srinivas, D. Woods, E. Winfree, and L. Qian, “A cargo-sorting DNA robot,” *Science (80-.)*, vol. 357, no. 6356, 2017.
- [33] B. Yurke, A. J. Turberfield, A. P. Mills, F. C. Simmel, and J. L. Neumann, “A DNA-fuelled molecular machine made of DNA,” *Nature*, vol. 406, pp. 605–608, aug 2000.
- [34] E. S. Andersen, M. Dong, M. M. Nielsen, K. Jahn, R. Subramani, W. Mamdouh, M. M. Golas, B. Sander, H. Stark, C. L. P. Oliveira, J. S. Pedersen, V. Birkedal, F. Besenbacher, K. V. Gothelf, and J. Kjems, “Self-assembly of a nanoscale DNA box with a controllable lid,” *Nature*, vol. 459, no. 7243, pp. 73–76, 2009.
- [35] R. M. Zadegan, M. D. E. Jepsen, K. E. Thomsen, A. H. Okholm, D. H. Schaffert, E. S. Andersen, V. Birkedal, and J. Kjems, “Construction of a 4 zeptoliters switchable 3D DNA box origami,” *ACS Nano*, vol. 6, no. 11, pp. 10050–10053, 2012.
- [36] G. Grossi, M. Dalgaard Ebbesen Jepsen, J. Kjems, and E. S. Andersen, “Control of enzyme reactions by a reconfigurable DNA nanovault,” *Nat. Commun.*, vol. 8, p. 992, dec 2017.
- [37] T. Tomaru, Y. Suzuki, I. Kawamata, S.-i. M. Nomura, and S. Murata, “Stepping operation of a rotary DNA origami device,” *Chem. Commun.*, vol. 53, pp. 7716–7719, jul 2017.
- [38] D. Selnihhin, S. M. Sparvath, S. Preus, V. Birkedal, and E. S. Andersen, “Multifluorophore DNA Origami Beacon as a Biosensing Platform,” *ACS Nano*, vol. 12, pp. 5699–5708, jun 2018.
- [39] T. Liedl, B. Högberg, J. Tytell, D. E. Ingber, and W. M. Shih, “Self-assembly of three-dimensional prestressed tensegrity structures from DNA,” *Nat. Nanotechnol.*, vol. 5, no. 7, pp. 520–524, 2010.
- [40] C. E. Castro, H.-J. J. Su, A. E. Marras, L. Zhou, and J. Johnson, “Mechanical design of DNA nanostructures,” *Nanoscale*, vol. 7, pp. 5913–21, apr 2015.
- [41] Y. Ke, T. Meyer, W. M. Shih, and G. Bellot, “Regulation at a distance of biomolecular interactions using a DNA origami nanoactuator,” *Nat. Commun.*, vol. 7, p. 10935, 2016.
- [42] Y. Choi, H. Choi, A. C. Lee, H. Lee, and S. Kwon, “A Reconfigurable DNA Accordion Rack,” *Angew. Chemie - Int. Ed.*, vol. 57, no. 11, pp. 2811–2815, 2018.

- [43] T. Gerling, K. F. Wagenbauer, A. M. Neuner, and H. Dietz, “Dynamic DNA devices and assemblies formed by shape-complementary, non-base pairing 3D components,” *Science* (80-.), vol. 347, pp. 1446–1452, mar 2015.
- [44] A. Kuzuya, Y. Sakai, T. Yamazaki, Y. Xu, and M. Komiyama, “Nanomechanical DNA origami ‘single-molecule beacons’ directly imaged by atomic force microscopy,” *Nat. Commun.*, vol. 2, p. 449, sep 2011.
- [45] A. Kuzyk, R. Schreiber, H. Zhang, A. O. Govorov, T. Liedl, and N. Liu, “Reconfigurable 3D Plasmonic Metamolecules,” *Nat. Mater.*, vol. 13, no. July, p. 862, 2014.
- [46] A. E. Marras, L. Zhou, H.-J. Su, and C. E. Castro, “Programmable motion of DNA origami mechanisms,” *Proc. Natl. Acad. Sci. U. S. A.*, vol. 112, no. 3, pp. 713–718, 2015.
- [47] L. Zhou, A. E. Marras, H. J. Su, and C. E. Castro, “Direct design of an energy landscape with bistable DNA origami mechanisms,” *Nano Lett.*, vol. 15, no. 3, pp. 1815–1821, 2015.
- [48] J. List, E. Falgenhauer, E. Kopperger, G. Pardatscher, and F. C. Simmel, “Long-range movement of large mechanically interlocked DNA nanostructures,” *Nat. Commun.*, vol. 7, p. 12414, 2016.
- [49] P. Ketterer, E. M. Willner, and H. Dietz, “Nanoscale rotary apparatus formed from tight-fitting 3D DNA components,” *Sci. Adv.*, vol. 2, no. 2, pp. e1501209–e1501209, 2016.
- [50] A. Kuzyk, Y. Yang, X. Duan, S. Stoll, A. O. Govorov, H. Sugiyama, M. Endo, and N. Liu, “A Light-Driven Three-Dimensional Plasmonic Nanosystem That Translates Molecular Motion into Reversible Chiroptical Function,” *Nat. Commun.*, vol. 7, p. 10591, 2016.
- [51] A. Kuzyk, M. J. Urban, A. Idili, F. Ricci, and N. Liu, “Selective Control of Reconfigurable Chiral Plasmonic Metamolecules,” *Sci. Adv.*, vol. 3, p. e1602803, 2017.
- [52] A. E. Marras, Z. Shi, M. G. Lindell, R. A. Patton, C.-M. Huang, L. Zhou, H.-J. Su, G. Arya, and C. E. Castro, “Cation-Activated Avidity for Rapid Reconfiguration of DNA Nanodevices,” *ACS Nano*, vol. 0, p. acsnano.8b04817, sep 2018.
- [53] S. M. Douglas, I. Bachelet, and G. M. Church, “A Logic-Gated Nanorobot for Targeted Transport of Molecular Payloads,” *Science* (80-.), vol. 335, p. 831, feb 2012.
- [54] H. K. Walter, J. Bauer, J. Steinmeyer, A. Kuzuya, C. M. Niemeyer, and H. A. Wagenknecht, “DNA Origami Traffic Lights with a Split Aptamer Sensor for a Bicolor Fluorescence Readout,” *Nano Lett.*, vol. 17, p. 2467, 2017.
- [55] J. Yang, S. Jiang, X. Liu, L. Pan, and C. Zhang, “Aptamer-Binding Directed DNA Origami Pattern for Logic Gates,” *ACS Appl. Mater. Interfaces*, vol. 8, p. 34054, 2016.
- [56] J. V. Le, Y. Luo, M. A. Darcy, C. R. Lucas, M. F. Goodwin, M. G. Poirier, and C. E. Castro, “Probing Nucleosome Stability with a DNA Origami Nanocaliper,” *ACS Nano*, vol. 10, no. 7, pp. 7073–7084, 2016.

- [57] J. J. Funke, P. Ketterer, C. Lieleg, S. Schunter, P. Korber, and H. Dietz, “Uncovering the forces between nucleosomes using DNA origami,” *Sci. Adv.*, vol. 2, no. 11, pp. e1600974–e1600974, 2016.
- [58] Y. Yang, R. Tashiro, Y. Suzuki, T. Emura, K. Hidaka, H. Sugiyama, and M. Endo, “A Photoregulated DNA-Based Rotary System and Direct Observation of Its Rotational Movement,” *Chem. - Eur. J.*, vol. 23, p. 3979, 2017.
- [59] E. Kopperger, J. List, S. Madhira, F. Rothfischer, D. C. Lamb, and F. C. Simmel, “A Self-Assembled Nanoscale Robotic Arm Controlled by Electric Fields,” *Science (80-.)*, vol. 359, p. 296, 2018.
- [60] S. Lauback, K. R. Mattioli, A. E. Marras, M. Armstrong, T. P. Rudibaugh, R. Sooryakumar, and C. E. Castro, “Real-Time Magnetic Actuation of DNA Nanodevices Via Modular Integration with Stiff Micro-Levers,” *Nat. Commun.*, vol. 9, p. 1446, 2018.
- [61] L. Zhou, A. E. Marras, C. E. Castro, and H.-J. Su, “Pseudorigid-Body Models of Compliant DNA Origami Mechanisms,” *J. Mech. Robot.*, vol. 8, no. 5, p. 51013, 2016.
- [62] L. Zhou, A. E. Marras, H. J. Su, and C. E. Castro, “Direct design of an energy landscape with bistable DNA origami mechanisms,” *Nano Lett.*, vol. 15, no. 3, pp. 1815–1821, 2015.
- [63] J. J. Birac, W. B. Sherman, J. Kopatsch, P. E. Constantinou, and N. C. Seeman, “Architecture with GIDEON, a program for design in structural DNA nanotechnology,” *J. Mol. Graph. Model.*, vol. 25, no. 4, pp. 470–480, 2006.
- [64] E. S. Andersen, M. Dong, M. M. Nielsen, K. Jahn, A. Lind-Thomsen, W. Mamdouh, K. V. Gothelf, F. Besenbacher, and J. Kjems, “DNA origami design of dolphin-shaped structures with flexible tails,” *ACS Nano*, vol. 2, no. 6, pp. 1213–1218, 2008.
- [65] S. Williams, K. Lund, C. Lin, P. Wonka, S. Lindsay, and H. Yan, “Tiamat: A three-dimensional editing tool for complex DNA structures,” *Lect. Notes Comput. Sci. (including Subser. Lect. Notes Artif. Intell. Lect. Notes Bioinformatics)*, vol. 5347 LNCS, pp. 90–101, 2009.
- [66] D.-N. N. Kim, F. Kilchherr, H. Dietz, and M. Bathe, “Quantitative Prediction of 3D Solution Shape and Flexibility of Nucleic Acid Nanostructures.,” *Nucleic Acids Res.*, vol. 40, no. 7, pp. 2862–2868, 2012.
- [67] J. SantaLucia and D. Hicks, “The thermodynamics of DNA structural motifs.,” *Annu. Rev. Biophys. Biomol. Struct.*, vol. 33, pp. 415–40, 2004.
- [68] S. M. Copp, D. E. Schultz, S. Swasey, and E. G. Gwinn, “Atomically Precise Arrays of Fluorescent Silver Clusters: A Modular Approach for Metal Cluster Photonics on DNA Nanostructures.,” *ACS Nano*, vol. 9, no. 3, pp. 2303–2310, 2015.

- [69] K. Pan, D.-N. Kim, F. Zhang, M. R. Adendorff, H. Yan, and M. Bathe, “Lattice-free prediction of three-dimensional structure of programmed DNA assemblies,” *Nat. Commun.*, vol. 5, p. 5578, 2014.
- [70] R. S. Sedeh, K. Pan, M. R. Adendorff, O. Hallatschek, K.-J. Bathe, and M. Bathe, “Computing Nonequilibrium Conformational Dynamics of Structured Nucleic Acid Assemblies,” *J. Chem. Theory Comput.*, vol. 12, no. 1, pp. 261–273, 2015.
- [71] T. E. Ouldridge, A. a. Louis, and J. P. K. Doye, “Structural, mechanical, and thermodynamic properties of a coarse-grained DNA model,” *J. Chem. Phys.*, vol. 134, p. 085101, feb 2011.
- [72] J. Yoo and A. Aksimentiev, “In situ structure and dynamics of DNA origami determined through molecular dynamics simulations.,” *Proc. Natl. Acad. Sci. U. S. A.*, vol. 110, no. 50, pp. 20099–20104, 2013.
- [73] V. Maingi, M. Lelimosin, S. Howorka, and M. S. P. Sansom, “Gating-like Motions and Wall Porosity in a DNA Nanopore Scaffold Revealed by Molecular Simulations,” *ACS Nano*, vol. 9, no. 11, pp. 11209–11217, 2015.
- [74] C. Y. Li, E. A. Hemmig, J. Kong, J. Yoo, S. Hernández-Ainsa, U. F. Keyser, and A. Aksimentiev, “Ionic conductivity, structural deformation, and programmable anisotropy of DNA origami in electric field,” *ACS Nano*, vol. 9, no. 2, pp. 1420–1433, 2015.
- [75] H. Joshi, A. Kaushik, N. C. Seeman, and P. K. Maiti, “Nanoscale Structure and Elasticity of Pillared DNA Nanotubes,” *ACS Nano*, vol. 10, no. 8, pp. 7780–7791, 2016.
- [76] S. M. Slone, C.-Y. Li, J. Yoo, and A. Aksimentiev, “Molecular mechanics of DNA bricks: in situ structure, mechanical properties and ionic conductivity,” *New J. Phys.*, vol. 18, no. 5, p. 55012, 2016.
- [77] F. Iacovelli, M. Falconi, B. R. Knudsen, and A. Desideri, “Comparative simulative analysis of single and double stranded truncated octahedral DNA nanocages,” *RSC Adv.*, vol. 6, no. 42, pp. 35160–35166, 2016.
- [78] D. A. Potoyan, A. Savelyev, and G. A. Papoian, “Recent successes in coarse-grained modeling of DNA,” *Wiley Interdiscip. Rev. Comput. Mol. Sci.*, vol. 3, no. 1, pp. 69–83, 2013.
- [79] T. E. Ouldridge, R. L. Hoare, A. A. Louis, J. P. K. Doye, J. Bath, and A. J. Turberfield, “Optimizing DNA nanotechnology through coarse-grained modeling: A two-footed DNA walker,” *ACS Nano*, vol. 7, no. 3, pp. 2479–2490, 2013.
- [80] P. Šulc, F. Romano, T. E. Ouldridge, J. P. K. Doye, and A. a. Louis, “A nucleotide-level coarse-grained model of RNA,” *J. Chem. Phys.*, vol. 140, no. 23, 2014.
- [81] F. Romano, A. Hudson, J. P. K. Doye, T. E. Ouldridge, and A. A. Louis, “The effect of topology on the structure and free energy landscape of DNA kissing complexes,” *J. Chem. Phys.*, vol. 136, no. 21, p. 215102, 2012.

- [82] C. Matek, T. E. Ouldridge, A. Levy, J. P. K. Doye, and A. A. Louis, “DNA cruciform arms nucleate through a correlated but asynchronous cooperative mechanism,” *J. Phys. Chem. B*, vol. 116, pp. 11616–11625, sep 2012.
- [83] N. Srinivas, T. E. Ouldridge, P. Šulc, J. M. Schaeffer, B. Yurke, A. A. Louis, J. P. K. Doye, and E. Winfree, “On the biophysics and kinetics of toehold-mediated DNA strand displacement,” *Nucleic Acids Res.*, vol. 41, pp. 10641–10658, dec 2013.
- [84] L. Rovigatti, F. Bomboi, and F. Sciortino, “Accurate phase diagram of tetravalent DNA nanostars,” *J. Chem. Phys.*, vol. 140, p. 154903, apr 2014.
- [85] C. Matek, T. E. Ouldridge, J. P. K. Doye, and A. A. Louis, “Plectoneme tip bubbles: Coupled denaturation and writhing in supercoiled DNA,” *Sci. Rep.*, vol. 5, p. 7655, jul 2015.
- [86] J. S. Schreck, T. E. Ouldridge, F. Romano, P. Šulc, L. P. Shaw, A. A. Louis, and J. P. Doye, “DNA hairpins destabilize duplexes primarily by promoting melting rather than by inhibiting hybridization,” *Nucleic Acids Res.*, vol. 43, pp. 6181–6190, jul 2015.
- [87] J. P. K. Doye, T. E. Ouldridge, A. a. Louis, F. Romano, P. Šulc, C. Matek, B. E. K. Snodin, L. Rovigatti, J. S. Schreck, R. M. Harrison, and W. P. J. Smith, “Coarse-graining DNA for simulations of DNA nanotechnology,” *Phys. Chem. Chem. Phys.*, vol. 15, pp. 20395–20414, dec 2013.
- [88] T. E. Ouldridge, “DNA nanotechnology: understanding and optimisation through simulation,” *Mol. Phys.*, vol. 113, pp. 1–15, jan 2015.
- [89] B. E. K. Snodin, F. Romano, L. Rovigatti, T. E. Ouldridge, A. A. Louis, and J. P. K. Doye, “Direct Simulation of the Self-Assembly of a Small DNA Origami,” *ACS Nano*, vol. 10, no. 2, pp. 1724–1737, 2016.
- [90] B. E. K. Snodin, F. Randisi, M. Mosayebi, P. Šulc, J. S. Schreck, F. Romano, T. E. Ouldridge, R. Tsukanov, E. Nir, A. A. Louis, and J. P. K. Doye, “Introducing improved structural properties and salt dependence into a coarse-grained model of DNA,” *J. Chem. Phys.*, vol. 142, no. 23, p. 234901, 2015.
- [91] L. Zhou, A. E. Marras, H. J. Su, and C. E. Castro, “DNA origami compliant nanostructures with tunable mechanical properties,” *ACS Nano*, vol. 8, no. 1, pp. 27–34, 2014.
- [92] A. E. Marras, L. Zhou, V. Koliopoulos, H. J. Su, and C. E. Castro, “Directing folding pathways for multi-component DNA origami nanostructures with complex topology,” *New J. Phys.*, vol. 18, no. 5, p. 55005, 2016.
- [93] D. C. Khara, J. S. Schreck, T. E. Tomov, Y. Berger, T. E. Ouldridge, J. P. K. Doye, and E. Nir, “DNA bipedal motor walking dynamics: an experimental and theoretical study of the dependency on step size,” *Nucleic Acids Res.*, no. January, pp. 1–9, 2017.

Chapter 2

Conformational Dynamics of Mechanically-Compliant DNA Nanostructures from Coarse-Grained Molecular Dynamics Simulations

2.1 Abstract

Structural DNA nanotechnology, the assembly of rigid 3D structures of complex yet precise geometries, has recently been used to design dynamic, mechanically-compliant nanostructures with tunable equilibrium conformations and conformational distributions. Here we use coarse-grained molecular dynamics simulations to provide insights into the conformational dynamics of a set of mechanically compliant DNA nanostructures—DNA hinges that use single-stranded DNA “springs” to tune the equilibrium conformation of a layered double-stranded DNA “joint” connecting two stiff “arms” constructed from DNA helix bundles. The simulations reproduce the experimentally measured equilibrium angles between hinge arms for a range of

hinge designs. The hinges are found to be structurally stable, except for some fraying of the open ends of the DNA helices comprising the hinge arms and some loss of base-pairing interactions in the joint regions coinciding with the crossover junctions, especially in hinges designed to exhibit a small bending angle that exhibit large local stresses resulting in strong kinks in their joints. Principal component analysis reveals that while the hinge dynamics are dominated by bending motion, some twisting and sliding of hinge arms relative to each other also exists. Forced deformation of the hinges reveals distinct bending mechanisms for hinges with short, inextensible springs *versus* those with longer, more extensible springs. We also introduce an approach for predicting equilibrium hinge angles from individual force-deformation behaviors of its single- and double-stranded DNA components. Such an approach that provides rapid, quantitative predictions could find applications in the design of compliant structures with programmed mechanical behavior. Taken together, these results demonstrate that coarse-grained modeling is a promising approach for designing, predicting, and studying dynamic DNA nanostructures, where conformational fluctuations become important, multiple deformation mechanisms exist, and continuum approaches may not yield accurate properties.

2.2 Introduction

The concept of scaffolded DNA origami (1) has accelerated the progress in DNA nanotechnology by enabling faster and more efficient design of structures with complex geometries. An exquisite array of 2D and 3D nanostructures have been created by DNA origami that include templated nanotubes (2; 3), nanoribbons(4), nanopores (5), nanoparticles (6; 7), nanoscale molds (8) and drug delivery vehicles (9; 10), just to name a few. With the advent of computer-aided design tools like caDNAo (11), Tiamat (12), CanDo (13; 14), and DAEDALUS (15), the design and fabrication of such DNA nanostructures is now a relatively fast and well-developed process. Though a majority of structures built *via* DNA origami are mechanically rigid, researchers have

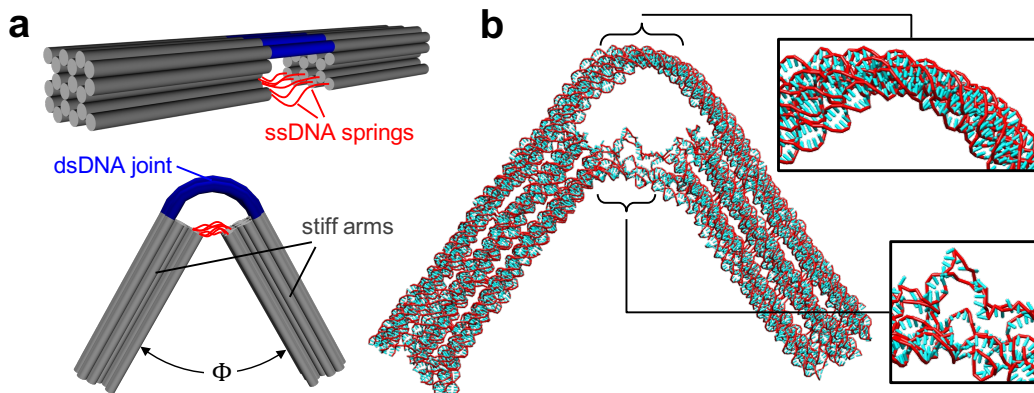


Figure 2.1: Coarse-grained (CG) modeling of DNA origami hinges. (a) Schematic of the hinge illustrating its three main components: a compliant “joint” (blue) composed of 6×1 layer of interconnected 84-base long dsDNA helices; a pair of stiff “arms” (gray), each composed of a stacked 6×3 bundle of interconnected dsDNA helices arranged in a honeycomb lattice; and six flexible ssDNA “springs” (red). Altering the length of the ssDNA springs from 0 to 74 bases leads to an increase in the hinge angle Φ (defined as the angle subtended by two arms) from $\sim 55^\circ$ to $\sim 130^\circ$. (b) CG model of a hinge (with 32-base long springs) used for simulating its conformational dynamics; also shown are closeup views of the joint and the springs. The model was rendered using the UCSF Chimera program (20).

begun to create “dynamic structures” that exhibit large-scale thermal fluctuations about a stable conformational state or transitions across multiple stable states, features synonymous with biological molecular motors and enzymes. For instance, by exploiting differences in the mechanical properties of single-stranded DNA (ssDNA), double-stranded DNA (dsDNA), and bundles of interconnected dsDNA helices, researchers have created a new class of nanostructures such as hinges and pistons whose equilibrium conformational distributions and mechanical compliance is determined by the competition between tension in the ssDNA components and compressive or bending resistance of the dsDNA components (16; 17; 18). These structures can be designed to exhibit specific conformational changes with tunable energy landscape and mechanical stiffness (17; 18; 19).

Much like compliant mechanisms have expanded the functional scope of macroscopic machines, these dynamic structures can be used as the building blocks of next-generation nanodevices and nanomachines with programmed response to physical interactions with the local environment.

Critical to this vision is the availability of modeling tools that would allow researchers to predict the molecular-scale conformation, dynamics, structural stability, and mechanical behavior of structural designs. Due to the large size of the system, we choose oxDNA as the modeling tool for investigating the behavior of the hinge.

In this study, we investigate the ability of the oxDNA model and MD simulations to predict the conformational dynamics of mechanically compliant DNA devices. For our analysis, we chose the set of compliant DNA origami hinges designed, fabricated and studied experimentally by Castro and coworkers (18). The hinges exhibit an angular bending degree-of-freedom ubiquitous in macroscopic machines, especially in compliant mechanisms, and therefore they are an excellent prototype for dynamic, functionally-relevant nanodevices. In particular, the hinges are composed of stiff “arms”, comprised of a bundle of interconnected dsDNA helices, connected by a compliant dsDNA “joint” and flexible ssDNA “springs”, and the angle between the arms could easily be tuned by changing the length of the springs (see Figure 2.1 and caption). The hinges were extensively characterized, providing a wealth of experimental data for comparison. Our results demonstrate excellent agreement between the predicted hinge angles and those measured experimentally, suggesting that CG modeling and simulations could be an effective predictive tool for designing dynamic DNA nanostructures. We also used the model to elucidate the conformational fluctuations, global dynamics, base-pairing stability, and large-deformation behavior of the DNA hinges, revealing useful nanoscopic insights into the properties of mechanically compliant DNA devices. Lastly, we demonstrate how macroscopic machine design principles could be coupled with microscopic behavior of individual DNA components obtained from CG models to make rapid predictions about the equilibrium behavior of dynamic nanodevices, a key advantage to speeding up the design process. More broadly speaking, this work establishes a methodology for the quantitative analysis of nanomechanical DNA devices and the rational design of next-generation dynamic DNA nanomachines with programmed mechanical behavior.

2.3 Results

2.3.1 Equilibrium conformations

We first tested whether our MD simulations of the five DNA-origami hinge designs (with different spring lengths) based on the oxDNA model (Figure 2.1b) could predict the equilibrium angle distributions obtained from transmission electron microscopy (TEM) images of the experimental hinges (18). Representative snapshots of the hinges captured from the simulations are shown in Figure 2.2a. The “hinge angle” Φ was calculated as the angle subtended between linear fits through the two hinge arms in accordance with the experimental definition (18). Using this definition we computed the distribution of bending angles exhibited by each hinge design (Figure 2.2b). The angle distributions exhibit roughly Gaussian shapes with a standard deviation that seems to increase as the length of the spring increases from 0 to 74 bases, consistent with experiments. Furthermore, a clear shift towards larger Φ with increasing spring length is observed, also consistent with experiments. A qualitative comparison of these distributions against those gathered from experiments reveals good agreement (Figure 2.11).

To more quantitatively compare the simulated and experimental hinge angle distributions, we determined Gaussian fits of each distribution and obtained: the location of their peaks Φ_0 , denoting hinge “equilibrium” angles, and their full-width-at-half-maximum (FWHM), characterizing the size of bending fluctuations exhibited by each hinge. The equilibrium angles obtained from simulations show excellent agreement with the corresponding angles obtained from experiments (Figure 2.2c), except for the 0b hinges, where simulations overpredict the experimentally observed angle by roughly 10° . The FWHM values obtained from simulations also show good overall agreement with the experimentally obtained values, though the simulations seem to always underpredict experiments by 1° to 8° (Figure 2.2c inset). We also investigated whether the CanDo software (13; 14) could predict the equilibrium hinge angles based on an underlying finite elements description of rigid components and a worm-like-chain description of flexible

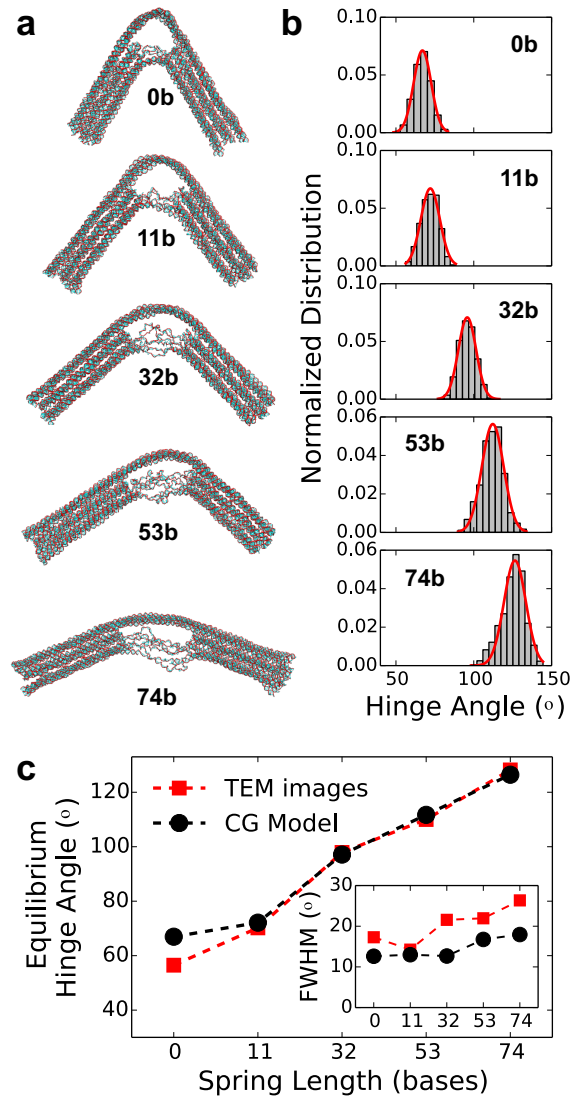


Figure 2.2: Hinge angles Φ predicted from MD simulations. (a) Representative snapshots of CG DNA hinges captured from simulations of the five hinge designs (with springs of lengths 0, 11, 32, 53, and 74 bases). (b) Normalized distribution of hinge angles obtained from simulations. Red lines represent Gaussian fits to the distributions. (c) Comparison of the equilibrium hinge angle Φ_0 and the size of angle fluctuations for the five designs obtained from simulations *versus* those measured experimentally. Statistical uncertainties in Φ_0 and FWHM are smaller than the symbol size.

components. While the computed angles reproduce the experimental trend of increasing Φ_0 with spring length, the angle predictions are much smaller than the experimental angles (Figure 2.12). Thus, for dynamic DNA nanostructures such as the DNA hinges examined here, CG modeling

and simulations seems to be a viable approach for predicting both equilibrium conformations and their fluctuations.

The slight discrepancy in the predicted and experimentally measured bending angle of Ob hinges (Figure 2.2c) is likely related to the especially strong deformation exhibited by these hinges. Specifically, in these hinges, the three lowermost springs connecting the two hinge arms are effectively dsDNA helices harboring a single nick in the middle (see Figure 2.13 or the origami designs provided in Supporting Information). To yield the small bending angles, these nicked dsDNA connections have to undergo a large deformation over a short ~ 10 bp stretch. We speculate that the experimental hinges accommodate this large deformation by forming a sharp kink at the nick, which is likely facilitated by the rearrangement of internal bond and torsional angles of the nucleotides and/or by the formation of non-canonical base pairing and stacking interactions. These finer-scale effects are not properly captured in the oxDNA model due to its low resolution and the rigid nature of its nucleotides. We therefore propose that some of the strong bending in these connections is achieved by other deformations, most likely by their bending at the exit points of the hinge arms, where the connections are not directly connected to other dsDNA helices of the hinge arms (see Figure 2.13). Such bending increases the effective length of the connections, leading to a slight increase in the hinge angle of the oxDNA model as compared to experiments. The reason for the smaller angular fluctuations exhibited by simulations as compared to experiments (Figure 2.2c inset) is even less clear. We speculate that such difference may arise from minor defects in the experimentally assembled hinges or from effects arising from their surface deposition for imaging that might affect the hinge angle distributions.

2.3.2 Structural stability

We evaluated the structural integrity of each hinge design by computing its internal structural fluctuations from the MD simulations, specifically, the root mean square fluctuation

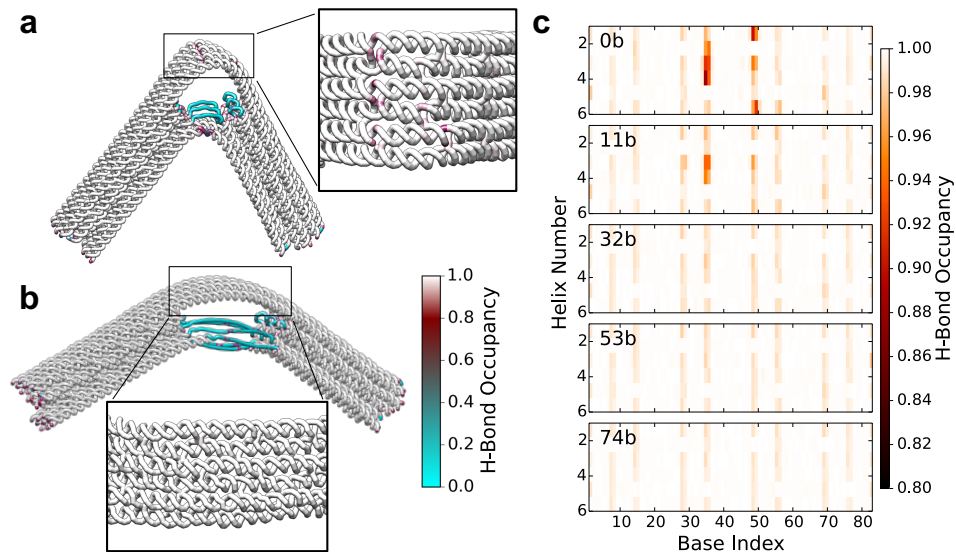


Figure 2.3: Stability of DNA base-pairing interactions within the origami hinges. (a–b) DNA-backbone representation of the hinges with (a) 0b-long springs and (b) 74b-long springs, colored according to the fraction of time their nucleotide bases remain bonded to their complementary bases (H-bond occupancy). Cyan-, red-, and white-colored regions indicate unpaired, weakly paired, and strongly paired bases. (c) Two-dimensional map showing H-bond occupancy of base pairs of the dsDNA helices comprising the hinge joints of all five hinge designs.

(RMSF) of the entire hinge as well as of its stiff components (hinge arms) alone. The results, shown for the 0b hinge in Figure 2.14, demonstrate that the stiff components of the hinges exhibit small structural deviations from the “mean” structure ($\text{RMSF} \approx 5\text{\AA}$) and even the entire hinge exhibit relatively small fluctuations ($\text{RMSF} \approx 10\text{\AA}$) primarily arising from fluctuations in their dsDNA joints and ssDNA springs. These results suggest that the two hinge arms can be essentially treated as rigid bodies, and therefore the hinge angle Φ could indeed be robustly defined based on the angle subtended between the two arms.

To investigate the local stability of the hinges, we computed the fraction of time each nucleotide base remains paired to another base within the hinge across all simulations; bases are considered as “paired” when their mutual interaction energy is negative and has a magnitude greater than the thermal energy $k_B T$, where k_B is the Boltzmann constant and T is the temperature. This fraction termed “H-bond occupancy” provides a local measure of the stability of double-

stranded portions of the hinge (arms and joint), and it also provides a measure of potentially disruptive non-specific interactions between single-stranded portions of the hinge (springs). The H-bond occupancies of the 0b and 74b hinges are shown mapped onto their corresponding structures in Figure 2.3a and 2.3b, and the occupancies of the remaining three designs are provided in Figure 2.15. Apart from some fraying observed at the open ends of the hinge arms, as indicated by red and cyan spots in the figure, the dsDNA helices of the arms in all five hinge designs remain base-paired most ($> 95\%$) of the time, as noted from the uniformly white color of the arms in the figures. We also observe that the hinge joints remain fully base-paired in most hinges except the 0b-hinge, where some unpairing of bases is observed at locations where the joint undergoes sharp bending. The ssDNA springs, whose sequences were designed to exhibit minimal interactions amongst each other, remain largely unpaired as expected, except for some base-pairing at intermittent locations along the springs, likely due to self-folding of ssDNA strands. Also as expected, the 4- and 18-bases long ssDNA loops lining the inner ends of the two hinge arms (as required by DNA origami) remain unpaired. Figure 2.3c provides a more detailed base-wise map of H-bond occupancy in each of the six dsDNA helices making up the joints in the five hinge designs. The maps confirm the stronger unpairing of bases in the 0b hinge joint, and to some extent the 11b hinge joints. The maps further reveal streaks of base unpairing, albeit small, at 7-base intervals in all five hinge designs whose locations correspond to the crossover junctions. These locations naturally lead to weak stacking interactions between adjacent bases on the DNA backbone (Figure 2.14). Taken together, all hinge designs are structurally stable and do not seem to contain any obvious unstable regions that could trigger more global instabilities.

To further investigate differences in the conformation of the joints across the different hinge designs, we evaluated the local bending of the dsDNA helices comprising the joints. As depicted in Figure 2.4a, the local bending was characterized in terms of the angle θ_i (at each base i) subtended by the displacement vectors $(\mathbf{r}_i - \mathbf{r}_{i-1})$ and $(\mathbf{r}_{i+1} - \mathbf{r}_i)$ connecting positions \mathbf{r}_{i-1} , \mathbf{r}_i , and \mathbf{r}_{i+1} of the center of masses of three adjacent base pairs along a DNA helix. The

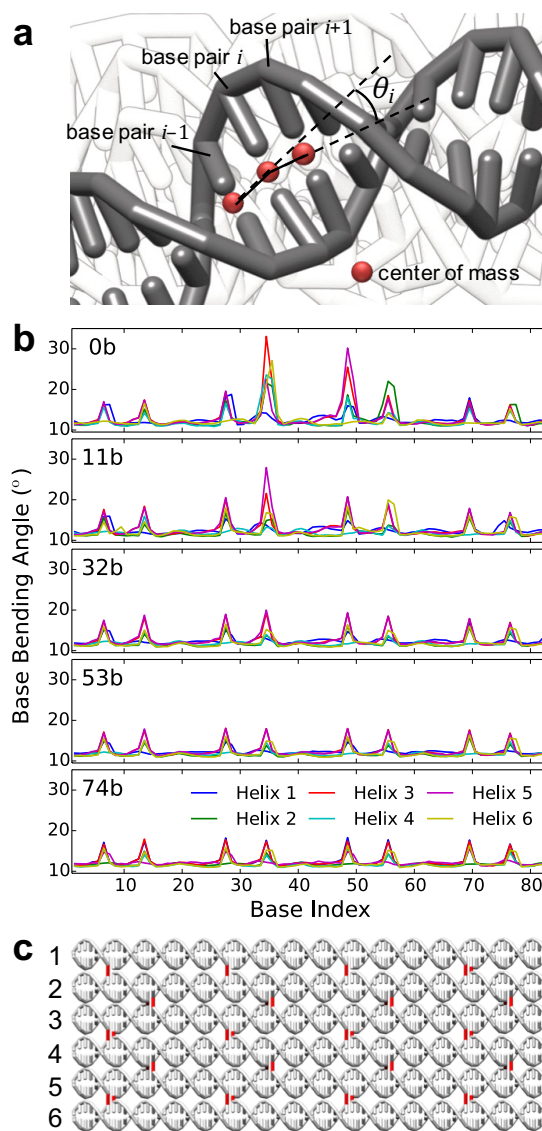


Figure 2.4: Local bending of the hinge joints. (a) Schematic illustrating the calculation of basewise bending angle of the dsDNA helices comprising the joints. (b) Bending-angle profiles of the six dsDNA helices comprising hinge joints, plotted for the five hinge designs. (c) Schematic of the 6-helix joint design showing helix numbering and the position of crossovers between dsDNA helices as marked by red lines.

resulting bending angle profiles for each of the six dsDNA helices comprising a joint are plotted in Figure 2.4b. The profiles reveal a uniform bending angle of $\sim 12^\circ$ interspersed with near-periodic, sharp peaks suggesting strong bending (kinking) of dsDNA helices at specific locations along

the joint helices. Examination of the topology of the layer of 6 helices in the joint (Figure 2.4c) reveals that these kinks occur at the locations of the crossover junctions, where the staple ssDNA strands cross over from one dsDNA helix to another. These inter-helix connections effectively result in nicks in the joint, making those locations easier to bend; These junctions are also responsible for the near-periodic streaks of base unpairing observed in Figure 2.3c. We also note that the bending angle peaks are especially large for the 0b and 11b hinges close to the middle of the joint, obviously occurring due to the more constricted hinge angle Φ exhibited by these two hinges with short springs (Figure 2.2c). As discussed in other studies (21), dsDNA subjected to strong bending forces can more effectively relax (minimize its free energy) by forming sharp kinks rather than bending uniformly across its entire length. Similar kinks were also observed experimentally in the case of 0b hinges (18). Interestingly, as the joints become increasingly bent (due to springs becoming shorter), the “baseline” bending angle of $\sim 12^\circ$ remains largely constant, suggesting that all the bending deformation is essentially accommodated at such kinks, especially those in the middle of the joints.

2.3.3 Global motions

To reveal the most important, large-scale (collective) motions exhibited by the DNA hinges, we carried out principal component analysis (PCA) of the hinge trajectories obtained from MD simulations. This approach decomposes the complex motion of a large molecule such as the hinge into principal components, or modes, each of which is specified by an eigenvector describing the direction of translational motion of that mode and a corresponding eigenvalue describing the amount of structural variance of the molecule captured by that mode. By projecting the simulated conformational dynamics of the hinge onto the eigenvector defined by the few largest principal components, one can obtain a lower-dimensional description of the conformational dynamics of each hinge design.

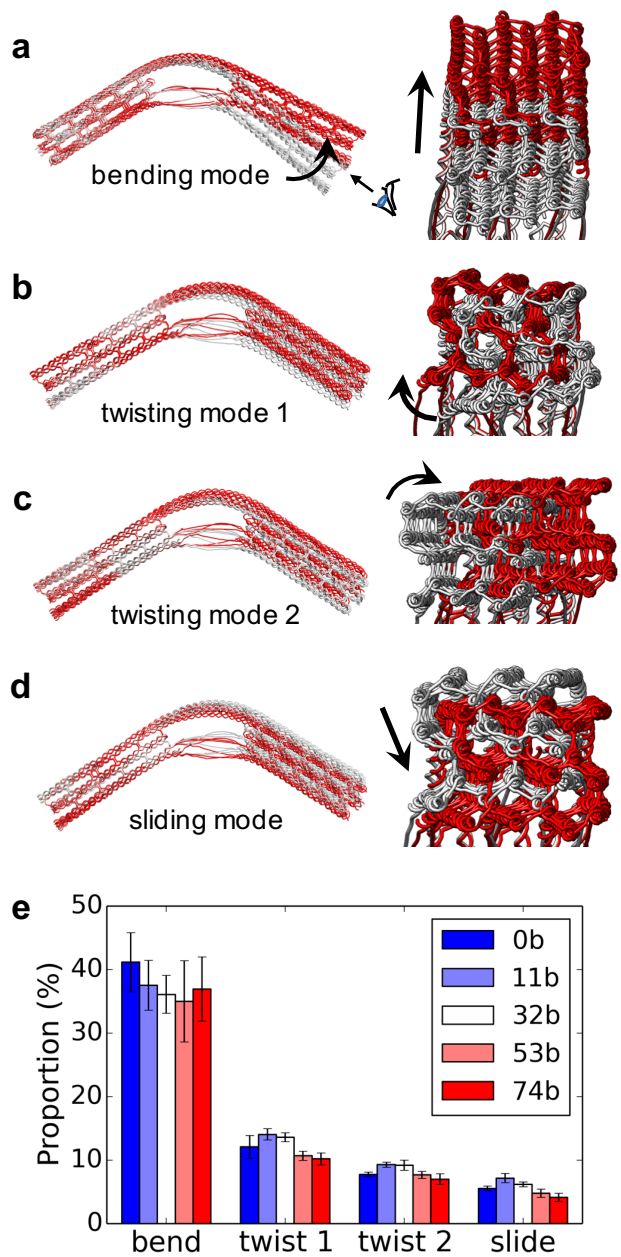


Figure 2.5: Principal component analysis (PCA) of the five hinges. Visualization of the four essential motions exhibited by the hinges revealed by PCA: (a) bending mode, (b,c) two twisting modes, and (d) sliding mode. The hinges are represented by lines joining the center of masses of the DNA bases with the largest and the smallest projections along the principal components depicted in white and red lines. The left and right columns show the front and side views of the four modes. (e) Bar chart showing the relative contribution of each mode towards the dynamics exhibited by each of the five hinges.

The PCA analysis reveals that over 70% of the internal variance of the hinges can be described by four principal components (Figure 2.5e). We confirmed that these dominant modes are relatively uncoupled from each other by computing correlations across them; Representative correlation plots for the 74b-hinge are provided in Figure 2.17. The most dominant principal component is the bending mode (Figure 2.5a), contributing about 38% of the hinge variance, followed by two twisting modes (Figure 2.5b,c) and a sliding mode (Figure 2.5d), each of which contribute about 5–12% of the variance. Visualization of the four modes, *via* projection of hinge dynamics along the eigenvectors corresponding to each mode, reveals that the bending mode represents in-plane, flexion-extension of one arm relative to the other while maintaining the end-to-end extension of the springs or the joint fixed, and it thus represents the mode most responsible for altering the hinge angle Φ . The two twisting modes are visualized as off-centered clockwise orbiting of a hinge arm relative to the other about different centers, motions that lead to only minor changes in Φ and in the joint and spring extensions. Finally, the sliding mode is visualized as a diagonal shift in the position of one arm relative to the other, with some change in the length of the springs and the joint but minor changes in Φ . These mode projections further reveal that the stiff arms preserve their internal structure across all four modes, consistent with our earlier RMSF analysis (Figure 2.14). The projections also reveal that, on average, the springs belonging to the 74b-hinge extrude out much more significantly as compared to those of the 0b-hinge, evidently due to strong electrostatic and entropic repulsive interactions between the longer springs (Figure 2.18). We also note that the net proportion of variance accounted by these four modes is smaller for the long-spring hinges compared to the hinges with short springs, which is also consistent with fact that hinges with longer springs have higher flexibility in general (Figure 2.5e).

Given that the bending mode is most responsible for the variations in hinge angle Φ , the PCA projections of hinge dynamics along this mode provide an excellent opportunity to more extensively study the bending of the joints; Such projections also have the potential to

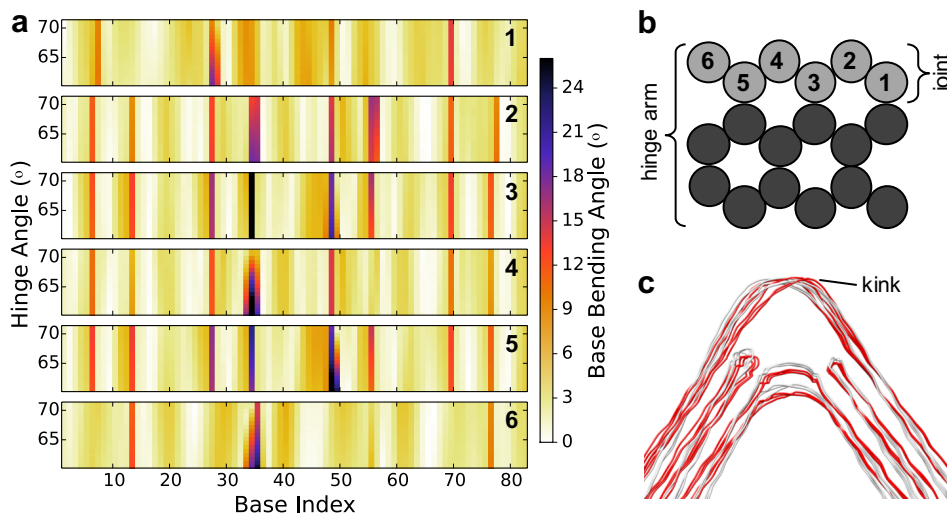


Figure 2.6: Local bending of 0b hinge joint from projections of hinge conformations along the bending-mode principal component (PC). (a) Maps of the basewise bending angle as a function of the hinge bending angle for the six joint helices numbered 1 through 6. (b) Hinge cross section showing the numbering scheme of the six joint helices (gray), and their connections amongst themselves and with the *remaining* helices comprising the hinge arms (black). (c) Minimum (white) and maximum hinge angle (red) projections along the bending mode PC illustrating the formation of a sharp kink in the joint. Only the dsDNA axes are shown for clarity.

reveal trends that are often difficult to glean from the raw MD trajectories where large thermal fluctuations mask subtle variations in global conformations and motions. We therefore carried out bending-angle calculations on these bending mode projections similar to those carried out earlier on the hinge conformations obtained from MD simulations. The results for 0b hinges are plotted in Figure 2.6a and show that the locations of the kinks coincide with those of the crossover junctions (Figure 2.4c) and relate well to the results obtained from MD trajectories (Figure 2.4b). Accordingly, the middle-four joint helices, which carry more crossover junctions than the two end helices (Figure 2.4c), exhibit a larger number of kinks. Since the bending deformation is now distributed over a larger number of kinks, the kinks in the middle helices are expectedly weaker than those in the end helices. Among the two end helices numbered 1 and 6, helix 1 exhibits a smaller increase in the bending angle as compared with helix 6. The reason is that the former is connected to two neighboring helices, while the latter is connected only to a single

neighboring helix, making the conformation of helix 1 somewhat more restricted compared to helix 6 (Figure 2.6b). Interestingly, this analysis could also reveal that the kinks in the joint helices become sharper with decreasing hinge angle Φ , as noted from the increase in the bending angles of several of the kinks in going from large to small angles. This effect is easily visualized in Figure 2.6c, which displays two extreme projections of the 0b-hinge, where one of the kinks is found to become extremely sharp at small hinge angles. Finally, we note subtle differences in local bending deformations across the six helices composing the hinge joints, also observed in local bending angle profiles Figure 2.4b, which likely arise from the additional twisting and sliding degrees of freedom exhibited by the hinges.

Large deformation behavior. Our MD simulations indicate that all hinge designs undergo relatively small fluctuations in the hinge angle at equilibrium, with full-width-at-half-maximum (FWHM) values in the range $\sim 10\text{--}20^\circ$. However, it is conceivable that future applications of such structures may require them to be subjected to strong external forces that considerably deform them beyond their equilibrium conformations. To investigate the behavior of the hinges under larger deformations that result in more strongly bent or flexed arms (beyond equilibrium fluctuations), we performed “restrained” MD simulations. In these simulations, the deformations were enforced by applying a stiff harmonic potential to the two hinge arms that strongly constrained their center-of-mass separation distance. By performing multiple such simulations, each constraining the hinge arms to different distances, we were able to obtain hinge conformations at different extents of deformation, spanning both smaller and larger hinge angles Φ than the equilibrium angle. We then monitored how the ensuing equilibrated end-to-end distances of the joint and the springs varied with respect to the enforced hinge angle (Figure 2.7a).

Figure 2.7b presents these variations in the joint and spring end-to-end distances as a function of hinge angle for the five hinge designs. We observe several kinds of behaviors: In the case of the 0b hinge, an increase in hinge angle results in a visible decrease in the joint end-to-end distance and a marginal decrease in the spring end-to-end distance. For the 11b hinges, the spring

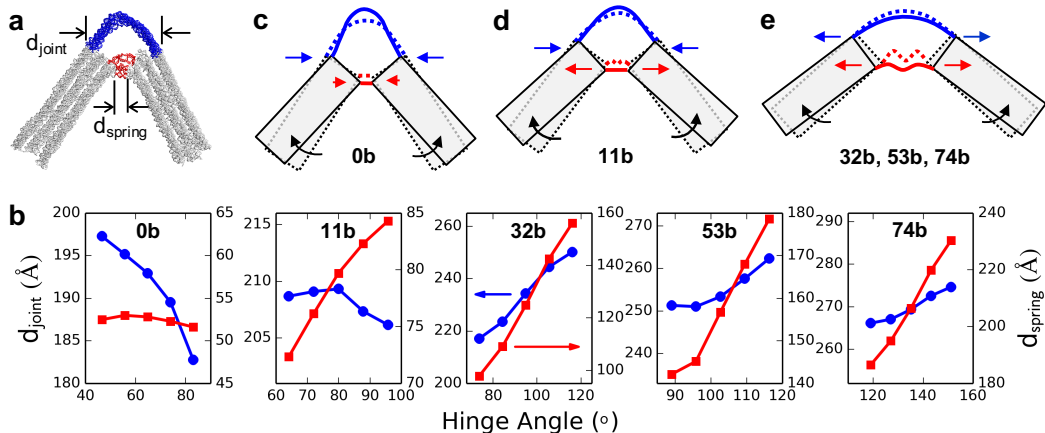


Figure 2.7: Hinge bending behavior under large deformations. (a) CG hinge highlighting the end-to-end distances d_{joint} and d_{spring} of the joint (blue) and the springs (red). (b) Variations in d_{joint} (blue) and d_{spring} (red) with hinge angle for each of the five hinge designs. (c-e) Schematics explaining differences in the bending behavior of (c) 0b, (d) 11b, and (e) 32b, 53b, and 74b hinges. Blue and red arrows depict direction of changes in d_{joint} and d_{spring} in response to the increase in hinge angle depicted by the curved black arrows; Small arrows imply minor changes. Dashed and solid lines show initial and final configurations of the hinge for increasing hinge angle.

end-to-end distance increases with increase in hinge angle, but the joint end-to-end distance shows a biphasic response, where the distance shows a rising trend with increasing angle for small angles ($\Phi < 80^{\circ}$) but a decreasing trend for larger angles. For the remaining hinges (with longer 32b, 53b, and 74b springs), both the joint and spring end-to-end distances increase with an increase in the hinge angle.

The above differences in hinge-bending behavior are intrinsically related to the length of ssDNA springs and the hinge angle. When the springs are sufficiently long, as in the case of the 32b, 53b, and 74b hinges, the hinge arms behave like two rigid bodies rotating about the center of the joint, as shown schematically in Figure 2.7e, which leads to the *simultaneous* extension (or compression) of the springs and joints observed in Figure 2.7b. The joint helices are weakly bent in these hinges and hence the joint is expected to bend uniformly like a Euler elastic beam, as suggested earlier (18). Moreover, the springs undergo appreciable stretching with increasing angle, which suggests that the springs in these hinges exhibit a somewhat loose conformation at

the equilibrium bending angle, as confirmed by the representative structures shown in Figure 2.2a.

The situation is fundamentally different in 0b hinges, where the springs are entirely double-stranded and thereby effectively incapable of stretching or shrinking. Consequently, all changes in hinge angle occur through rotation of the hinge arms about these dsDNA springs, and hence an increase in Φ leads to shrinkage in the joint end-to-end distance, as depicted schematically in Figure 2.7c. Such end-to-end compression of the joint, along with the additional constraint on the tangential emergence of joint helices from the hinge arms, leads to strong kinking of the joint helices that are already significantly bent as a result of the short springs. Such strong kinking of the joint helices cannot be treated using continuum mechanical Euler elastic beam model.

Lastly, the 11b hinges behave intermediate to the above two sets of hinges in that they exhibit a switch from one bending behavior to the other (Figure 2.7b). At small hinge angles, the springs are relatively loose and are capable of some stretching and the increase in bending angle occurs through rotation of hinge arms through the joint center, leading to simultaneous increase in both joint and spring distances. However, at large angle, the springs become taut and incapable of stretching further, leading to the rotation of hinge arms through the springs rather than the joint center and a subsequent decrease in the joint distance, as depicted in Figure 2.7d. This also leads to introduction of a kink in the joint, albeit of smaller magnitude than that observed in 0b hinges.

2.3.4 Hinge angle predictions from force-balance

In classical mechanics, a multicomponent system is considered to be at mechanical equilibrium when the net force and torque acting on all components is zero. The equilibrium conformation of the system can then be determined from “force-balance” and “torque-balance” conditions, that is, the force and torque one component exerts on another component through their connection point(s) is equal and opposite to the force and torque the second component exerts on the first component. We examined if such a force- and torque-balance formalism could be used to

predict the equilibrium conformations of our nanoscopic DNA hinges, that is, the equilibrium bending angles plotted in Figure 2.2c denoted by Φ_0 . To this end, we divided the hinge into two components: (i) the six ssDNA springs that connect the lower portions of the two hinge arms, and (ii) the rest of the hinge without springs consisting of the joint and the rigid hinge arms (Figure 2.8a). The first component, the springs, experience outward-pointing forces (tension) at their ends due to the bent joint attempting to straighten out the hinge arms. Though electrostatic repulsion between the arms may also contribute to this force, our calculations suggest that the repulsion is minimal (Figure 2.19), likely due to the high salt concentration used in simulations and experiments that essentially screens most electrostatic interactions. The second component, the springless hinge, experiences inward-pointing forces (compression) on the hinge arms at locations of spring attachment due to stretching of the springs. Interestingly, the torque-balance condition is automatically satisfied as the two components exert zero torque on each other due to symmetry: the springs exert equal and opposite forces on the two hinge arms at exactly opposite points and the springless hinge also exerts equal and opposite forces to the ends of the springs. Hence, only the force-balance condition is required, and the equilibrium angle Φ_0 of the hinges may be determined from the individual force-deformation behavior of the two hinge components, regardless of the origin of the forces, as the angle at which the corresponding deformations of the two components yield exactly the same force.

The force-deformation behavior of the springless hinges were determined by substituting each spring with a pair of forces applied to the DNA bases on the two hinge arms connected to the springs in the original design (Figure 2.8a top). However, all springs are *not* alike, as the three springs connected to the upper set of hinge arm helices are 24 bases longer than the three connected to the lower set of helices (except for the 74b hinges where the two sets of springs are of lengths 74 and 84 bases). Thus, the forces replacing the two sets of springs should be treated separately, which we denote by $F_{h,l}$ and $F_{h,u}$ for the lower and upper set of springs (depicted by red and blue arrows in Figure 2.8a). The force-deformation behavior was obtained by performing

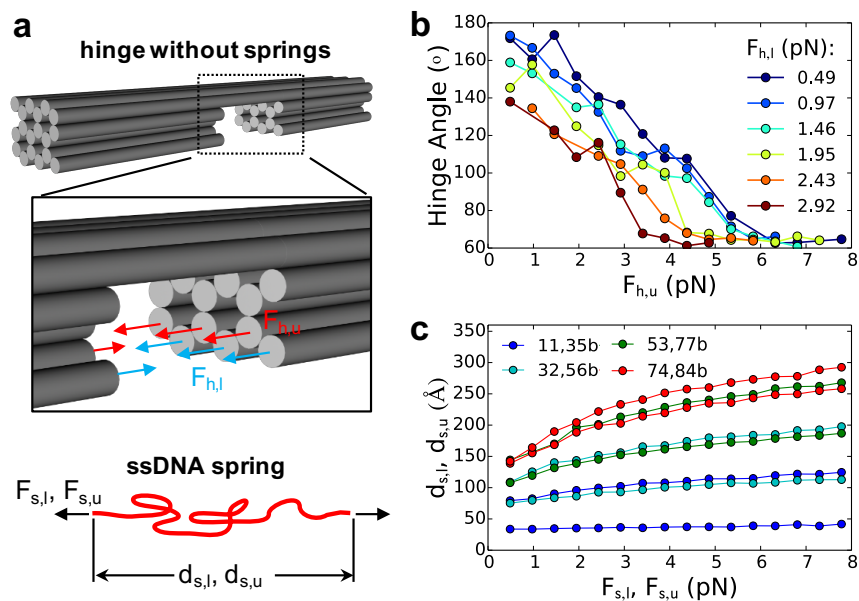


Figure 2.8: Force-deformation behavior of the joint and spring components of the hinge. (a) Schematic showing partitioning of the hinge into its two load-bearing components—the joint (hinge without springs) and the springs—whose force-deformations are treated separately. (b) Force-deformation profiles of the springless hinge for different combinations of force loads $F_{h,u}$ and $F_{h,l}$ applied to the upper and lower layer of dsDNA helices, which substitute the effects of the springs. (c) Force-extension behavior of the lower and upper ssDNA springs corresponding to the 11b, 32b, 53b, and 74b hinges.

a series of MD simulations mapping through various possible combinations of applied forces $F_{h,l}$ and $F_{h,u}$ and the resulting deformation was characterized in terms of the hinge angle Φ , as defined earlier. Figure 2.8b presents these force-deformation curves $\Phi(F_{h,l}, F_{h,u})$ as a function $F_{h,u}$ for different fixed values of $F_{h,l}$ showing the expected trend of decreasing hinge angle with increase in either force.

The force-deformation behavior of the lower and upper set of springs corresponding to each hinge design can also be determined from MD simulations by applying a stretching force to the individual springs and measuring their end-to-end distance (Figure 2.8a bottom). To distinguish between the behaviors of the two kinds of springs, we denote their end-to-end distances by $d_{s,l}$ and $d_{s,u}$ and the applied forces by $F_{s,l}$ and $F_{s,u}$. Figure 2.8c shows the computed force-extension behaviors $d_{s,l}(F_{s,l})$ and $d_{s,u}(F_{s,u})$ for the two sets of springs corresponding to the

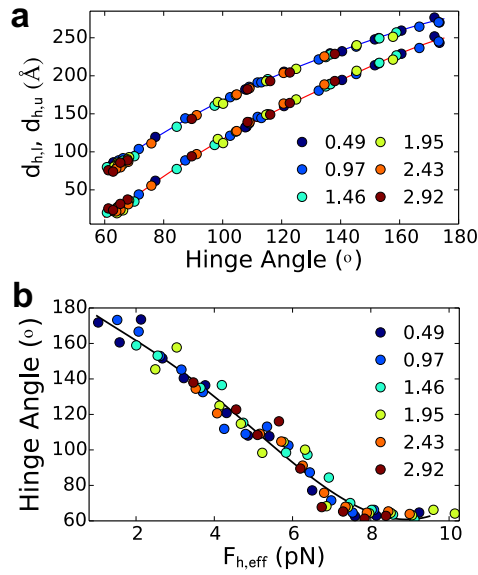


Figure 2.9: Additional relationships required for transforming or simplifying the force-deformation behavior of the springs and the joint. (a) Geometrical relationship between the end-to-end distances of the upper and lower spring-connection points and the hinge angle. (b) Force-coupling relationship $F_{h,eff} = F_{h,l} + \lambda F_{h,u}$ with $\lambda = 1.124$ allows collapse of the joint force-deformation curves in Figure 2.8b onto a single master curve. Symbols, with the same color scheme as in Figure 2.8, represent data measured from simulations of the springless hinge conducted at different $F_{h,u}$ and $F_{h,l}$, whereas lines represent polynomial fits to data.

11b, 32b, 53b, and 74b hinges (the hinge labeling corresponds to the length of the shorter spring). Note that this approach cannot be applied to 0b hinges, which do not contain any ssDNA springs. The profiles show behavior characteristic of polymer stretching that is typically modeled using the worm-like-chain model. As expected, the shorter, lower springs exhibit sharper force-extension behavior compared to the longer, upper springs.

The simulations of the springless hinge also reveal a strong relationship between distances $d_{s,l}$ and $d_{s,u}$ across the two sets of spring attachment points on the hinge arms and the hinge angle Φ (Figure 2.9a). These two geometrical relationships denoted by $d_{s,l}(\Phi)$ and $d_{s,u}(\Phi)$ are slightly nonlinear, suggesting some deformation of the spring attachment points upon application of force. We also note that hinges cannot contract beyond $\Phi \approx 60^\circ$, whereupon the distance between the spring connections points becomes smaller than the length of a single base pair, corresponding to

the case of the 0b hinge.

Lastly, the force-balance condition stipulates that at mechanical equilibrium, the magnitude of the spring and hinge forces are identical, *i.e.*,

$$F_{h,u} = F_{s,u}, \quad (2.1)$$

$$F_{h,l} = F_{s,l}. \quad (2.2)$$

The force-deformation profiles $\Phi(F_{h,l}, F_{h,u})$, $d_{s,l}(F_{s,l})$, and $d_{s,u}(F_{s,u})$ along with the geometrical relationships $d_{s,l}(\Phi)$ and $d_{s,u}(\Phi)$ and the force-balance constraints (Eqs. 1 and 2) results in a system of 7 relationships (equations) with 7 unknown variables. Solving these equations then yields the equilibrium hinge angle Φ_0 we seek. An underlying assumption here is that the springs do not interact with each other, and hence the force-extension behavior of the sets of three springs belonging to one layer can be obtained from the behavior of a single spring using the springs-in-parallel formulation. However, in cases where the springs interact with each other, it may be more correct to simulate groups of springs and computed their collective force-extension behavior.

Due to the dependence of the hinge angle on *two* variables ($F_{s,l}$ and $F_{s,u}$) and the need to satisfy *two* force-balance conditions (Eqs. 1 and 2), solving for the equilibrium angle Φ_0 becomes convoluted and requires an iterative numerical approach. To simplify the solution process, we investigated whether the two sets of forces could be combined into a single effective force. The rationale is that even though the effects of the lower and upper layer of springs are treated separately using two different forces, the equilibrium hinge angle results from their combined effect on the hinge arms. Specifically, $F_{h,l}$ and $F_{h,u}$ exert separate moments on the joint ends *via* the hinge arms, with the former exerting a larger moment due to the larger moment arm associated with that force. Hence, we proposed that the two forces could be coupled together through a

factor λ , resulting in an effective force

$$F_{h,\text{eff}} = F_{h,u} + \lambda F_{h,l}, \quad (2.3)$$

which, when applied to the upper layer of helices, should produce the same hinge deformation as the two separate forces applied to both layers of helices. Geometrically, the coupling factor should be 1.181 according to the ratio of the moment arms of the two force loads with respect to the joint-arm connection point. However, other factors could affect the coupling of forces, such as the deformation of the hinge arms near the springs, as mentioned earlier, and differences in the orientation of the terminal bases of the springs, both of which affect the length of the moment arm. The coupling factor is therefore obtained as a fitting parameter that best collapses all the distinct force-deformation profiles presented in Figure 2.8b onto a single “master” curve. The fitted value $\lambda = 1.124$ is quite close to the geometric prediction, implying that the aforementioned factors affecting the moment arms of the two force loads are not significant. Figure 2.9b shows the collapsed force-deformation $F_{h,\text{eff}}-\Phi$ plot demonstrating that the effect of the two applied forces (two sets of springs) can indeed be treated in terms of a single effective force.

This ability to couple the two spring forces applied to the hinge arms into a single effective force load greatly simplifies the solution of Φ_0 . First, the original 2D force-deformation landscape $\Phi(F_{h,l}, F_{h,u})$ of the springless hinge is now replaced by a 1D force-deformation master curve $\Phi(F_{h,\text{eff}})$, where the effective force is obtained *via* Eq. 3. Second, the original two force-balance conditions (Eqs. 1 and 2) are now replaced by a single effective force-balance condition

$$F_{h,\text{eff}} = F_{s,\text{eff}}, \quad (2.4)$$

where $F_{s,\text{eff}}$ represents the effective force exerted by the two sets of springs based on the coupling

factor determined earlier as given by

$$F_{s,\text{eff}} = F_{s,u} + \lambda F_{s,l}. \quad (2.5)$$

In this revised setup, one needs to solve a different set of 7 single-variable equations with 7 unknowns, namely, the force-deformation curves $\Phi(F_{h,\text{eff}})$, $d_{s,l}(F_{s,l})$, and $d_{s,u}(F_{s,u})$; the geometrical relationships $d_{s,l}(\Phi)$ and $d_{s,u}(\Phi)$; the effective force-balance condition given by Eq. 4, and the coupling relationship given by Eq. 5. Once the force-deformation curves of the springless hinge $F_{h,\text{eff}}(\Phi)$ and of the two sets of springs and $F_{s,l}(d_{s,l})$ and $F_{s,u}(d_{s,u})$ have been obtained, the protocol for obtaining Φ_0 becomes fairly straightforward: The $F_{s,l}(d_{s,l})$ and $F_{s,u}(d_{s,u})$ curves are first converted to $F_{s,u}(\Phi)$ and $F_{s,l}(\Phi)$ curves *via* the geometrical relationships $d_{s,l}(\Phi)$ and $d_{s,u}(\Phi)$. The two curves are then combined into a single $F_{s,\text{eff}}(\Phi)$ curve *via* the coupling factor (Eq. 5). The intersection between the resulting $F_{s,\text{eff}}(\Phi)$ and $F_{h,\text{eff}}(\Phi)$ curves, signifying the use of the force-balance constraint (Eq. 4), then yields the equilibrium hinge angle Φ_0 .

Figure 2.10a presents the force-deformation master curve $F_{h,\text{eff}}(\Phi)$ of the springless hinge along with the transformed force-deformation curves $F_{s,\text{eff}}(\Phi)$ of the springs corresponding to the 11b, 32b, 53b, and 74b hinges. The intersections of the two curves allows us to estimate the equilibrium hinge angle for the hinges with the certain ssDNA spring length. The predicted results shown in Figure 2.10b are in excellent agreement with both the experimentally measured hinge angles and those computed earlier from simulations of entire hinges. The promising nature of these results suggests that it may indeed be possible to predict the equilibrium conformation of a multicomponent DNA nanostructure from the force-deformation behavior of its individual components. In this study, we obtained such behavior from MD simulations of the components in isolation though, in principle, the components-level behavior could also be obtained experimentally.

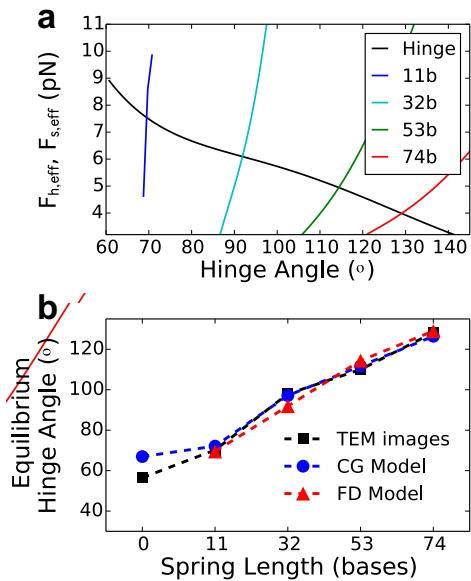


Figure 2.10: Equilibrium hinge angle from force-deformation (FD) behavior. (a) Transformed FD curves of the springless hinge and of the 11b, 32b, 53b, and 74b springs. (b) Equilibrium hinge angles as obtained from the intersection points of the transformed spring and hinge FD profiles compared to those obtained from simulations and experiments. Statistical uncertainties in Φ_0 are smaller than the symbol size.

2.4 Discussion

This study provides a detailed picture of the nanoscopic structural dynamics exhibited by a set of mechanically-compliant nanostructures fabricated *via* DNA origami—hinges with tunable bending angle designed by combining rigid DNA bundles with semirigid and flexible DNA elements. Our approach involved performing MD simulations of the DNA hinges treated using the *oxDNA* CG force field developed by the Ouldridge, Doye, and Louis labs. One of the goals of this study was to determine whether such a modeling approach could even capture the overall conformations of the hinges determined experimentally from electron microscopy. Our results show that the *oxDNA* model does reasonably well in reproducing the experimentally measured distributions of hinge bending angles for a range of hinge designs, especially the equilibrium angles denoted by the peaks in the angle distributions. This result is significant because the hinges are flexible and exhibit thermal fluctuations, and are thus not amenable

to modeling *via* continuum-mechanics approaches that have found success in modeling other more rigid DNA nanostructures. At the same time, the hinges are too large and undergo slow bending dynamics, making all-atom MD simulations computationally prohibitive for probing such dynamics. Hence, coarse-grained models that ignore fine-scale features and degrees of freedom while still accounting for important geometrical features, molecular interactions, and thermal fluctuations offer the only practically viable solution for probing the dynamics of such structures. Indeed, the oxDNA simulations required 14 hours CPU time on NVIDIA GPUs to simulate 100 μ s-long dynamics of the hinges, almost five orders of magnitude faster than all-atom MD simulations of the hinges in explicit solvent. The promising predictions made by the oxDNA model here suggests that such a CG modeling and simulation approach could be a useful tool for elucidating and predicting the dynamics of devices created *via* DNA nanotechnology and that such a tool could become an important component of computer aided design of such DNA devices. Needless to say, the approach would first have to be thoroughly tested and validated against other DNA nanostructures undergoing more complex dynamics or other kinds of conformational changes. Also, the approach would need to become more readily accessible to researchers in DNA nanotechnology who might not be experts in MD simulations.

Nevertheless, having established the predictive capability of oxDNA for the DNA hinges, we next used it to probe their intricate structure and dynamics. We found that in all hinge designs, the hinge arms composed of DNA helix bundles remained structurally intact during the simulations while exhibiting $\pm 5\text{--}8^\circ$ fluctuations about their equilibrium bending angle. By computing the fraction of time DNA nucleotide bases remain paired, we determined regions of local instability within the double-stranded portions of the hinge. Apart from obvious fraying of bases at the open ends of the hinge-arm helices, the dsDNA helices in both the hinge arms and the joints remained fairly stable throughout the simulations. Interestingly, the hinge joints display localized, near-periodic streaks of slightly less stable base-pairing interactions that coincide with the crossover points of the DNA staples. Analysis of the local bending of the joint helices revealed

that the helices bend more-or-less uniformly across their length, except at crossover junctions where they exhibit a relatively larger bending angle. These “kinks” in the joints become very sharp near the midpoint of the joint, especially for the 0b hinges designed to exhibit a small bending angle. Such strong kinking of the dsDNA helices in strongly bent joints is reminiscent of the kinks observed in the dsDNA wrapped around the histone octamer within nucleosomes, where the strong histone/DNA interactions lead to very strong superhelical bending of DNA (22).

Principal component analyses of the simulation trajectories of the hinges allowed us to extract their most dominant global motions. Our results show that while the dynamics of the hinges are dominated by the planar bending of arms relative to each other, other modes such as relative twisting and sliding of arms are also significant. While such secondary modes could be considered as a disadvantage in applications where precise motion along a single degree of freedom is required, the modes may also be considered as a unique advantage of these soft DNA-based devices, and this type of analyses could enable specific design of thermal fluctuations along multiple degrees of freedom. Indeed most naturally occurring nanomachines such as protein enzymes and molecular motors exhibit some degree of flexibility or softness along multiple degrees of motion that is often a critical part of the mechanical function. In the macroscopic world, the observed flexibility of hinges is remarkably similar to the knee joint in humans, which has primarily evolved to exhibit the bending degree of freedom, though other smaller rotations and sliding motions also occur that are in fact critical for the functionality and strength of the knee joint.

Examining the behavior of hinges subjected to strong deformation revealed that the hinges with sufficiently long ssDNA springs (>11 bases) exhibit bending behavior typical of joints, that is, extending the hinge angle leads to an increase in the end-to-end extension of both the joint and the springs, typical of the hinge arms rotating about the joint center to extend or flex. However, the 0b hinges, and to some extent the 11b hinges, exhibit fundamentally different behavior with the end-to-end extension of the joint decreasing, rather than increasing, with increasing hinge

angle. This effect arises due to the near-inextensible nature of short ssDNA springs that forces the hinge arms to flex or extend about the ssDNA connection points rather than the joint center. Due to the constraint on the orientation of the two ends of the joints as a result of their connection to the hinge arms, their opening up causes counterintuitive stronger-than-usual bending of the joints, leading to sharp kinking of the joint helices. Interestingly, such “auxetic” behavior with expansion in one dimension leading to expansion in the other dimension (as opposed to contraction, typical of most materials) could serve as a basis for the design of materials that exhibit in-plane or 3D negative Poisson’s ratio.

We also investigated if the equilibrium bending angles of the hinges could be predicted by combined analysis of its individual components using the force-balance principle commonly applied in continuum mechanics. To this end, we divided the hinge into two simpler mechanical components, the ssDNA springs and the remaining hinge minus the springs, and computed their individual force-deformation behaviors. By invoking the force balance conditions along with the geometric relationship between spring and hinge deformation, we were able to make excellent predictions of the hinge angle. Apart from demonstrating the applicability of a key principle of classical mechanics to a strongly fluctuating nanoscale device, the ability to predict the mechanical behavior of DNA devices from the behavior of their individual components would benefit the design of complex devices. In addition to simplifying the design process, it would save significant computational effort, for instance, when examining the behavior of device designs obtained from combinations of components with different properties. In the context of hinge design, predicting the behavior of all hinges assembled from m possible joint designs and n possible spring designs would nominally require $m \times n$ MD simulations of the full hinges, whereas the components-level design would require only $m + n$ simulations of the components, that is, fewer simulations of smaller systems. This framework is also amenable to a modular design framework where interchangeable components can be screened through a mechanical system to produce the desired overall mechanical behavior. Note that springs and joint design parameters are not just

restricted to their lengths, as examined in this work, but also changes in the material itself. For instance, the ssDNA springs could be replaced by ssDNA-dsDNA segments, azobenzene-tethered DNA segments (23), or other polymers (24).

2.5 Conclusions

We have examined the ability of CG modeling approach in revealing the conformational dynamics of DNA origami hinges. A good agreement between the CG model and the experimentally measured hinge angle was observed and further examination on various properties including local stability, principal motions, and design-dependent bending mechanism. Lastly, we proposed an approach for predicting equilibrium hinge angles from the individual force-deformation behaviors of different components, providing rapid, quantitative predictions with combination of molecular-scale approaches and macroscopic principles of mechanical equilibrium. This work lays the foundation for future studies dealing with understanding and predicting the mechanical behavior of other dynamic DNA nanostructures where continuum mechanics and all-atom models become inapplicable or computationally expensive. This work also sets ground for future work on designing mechanisms to actuate such structures for nanoscale sensing and mechanical engineering applications. For instance, the DNA hinges studied here could be engineered to trigger bending angle changes *via* design of displacement ssDNA strands that hybridize with the ssDNA springs to either flex or extend the hinges or *via* other responsive entities such as azobenzene-tethered DNA that respond to light to trigger a conformational change in the springs or the joints. The CG modeling approach tested here should aid in the design and optimization of such actuation mechanisms, and the components-level modeling strategy introduced here should further help speed up the process of design.

2.6 Methods

2.6.1 Hinge designs

The five DNA origami hinge designs, referred to as 0b, 11b, 32b, 53b, and 74b hinges, were built on a honeycomb lattice in the caDNAno package (11); The designs are provided in the Supporting Information (Figure 2.20–2.24). The joint DNA helices in each of the five hinge designs are 84 bp long. The two layers of springs are of lengths 0 and 24 bases in the 0b hinge; 11 and 35 bases in the 11b hinge; 32 and 56 bases in the 32b hinge; 53 and 77 bases in the 53b hinge; and 74 and 84 bases in the 74b hinge. Since the 18-helix DNA bundles composing the hinge arms essentially behave like rigid components and also exhibit negligible electrostatic repulsion between them (Figure 2.18), the length of the two hinge arms were reduced from ~ 220 bases in the experimental design to ~ 96 bases in our simulations; This allowed us simulate the hinges and predict their properties at significantly reduced computational costs.

2.6.2 Generation of initial hinge 3D conformations

The caDNAno hinge designs were used to generate initial 3D structures of the hinges in which their arms were completely flexed to 180° . However, such initial configurations resulted in abnormal stretching of the centermost phosphate bond in each spring of the hinge. To relax these stretched bonds, the bonds were cut and substituted with harmonic potential restraints of strength $0.4 \text{ kcal/mol/\AA}^2$ on the distance between the two bonded nucleotides during structural relaxation; In this process, the equilibrium distance of the restraints was shortened in 6 \AA steps every 600,000 MD simulation time steps until the equilibrium bond length was reached through gradual bending of the hinge arms, whereupon the broken bonds were reinstated.

2.6.3 MD simulations

The MD simulations were performed using the oxDNA package at a temperature of 298 K and a monovalent salt concentration of 500 mM Na⁺. The high salt regime were chosen to reproduce the strong electrostatic screening from 14–20 mM Mg²⁺ concentrations used to assemble and stabilize the hinges. While oxDNA2 can capture electrostatic screening effects of Mg²⁺ through the use of the Debye-Hückel formalism at high Na⁺ concentrations, the model is unable to capture finer-scale effects of Mg²⁺ ions such as their ability to form coordination complexes. However, such effects do not seem to be critical for DNA hinges, as the hinge angle distributions obtained from simulations conducted at lower Na⁺ concentrations (150 mM) were quite similar to those presented here (Figure 2.25). Furthermore, recent unpublished experiments by Castro and coworkers on a different set of hinges yield quite similar distributions in hinge angle for structures prepared using 600 mM Na⁺ and using 25 mM Mg²⁺.

2.6.4 Principal component analysis

This analysis was performed using the software package *bio3D* (25). Specifically, we inputted ~500 configurations (snapshots) of the hinge for each design, collected at equal time intervals from the entire 900 ns-long simulation trajectory. Each configuration of the hinge was described using the centers of masses of its DNA nucleotides; Note that each nucleotide is represented by two interaction sites in the oxDNA model.

2.6.5 Large deformation behavior

A harmonic restraint $U = 1/2k(d - d_0)^2$ of spring constant $k = 0.4 \text{ kcal mol}^{-1} \text{ \AA}^{-2}$ was applied to the distance d between the centers of mass of the two arms to restrain the hinge fluctuations around a target distance d_0 . By performing 150 ns-long MD simulations at different values of d_0 , we were able to generate differently-bent configurations of the hinges, well beyond

the bending angles exhibited by the hinge at equilibrium. Each simulation also yielded average hinge bending angle Φ and the average spring and joint end-to-end distances d_{joint} and d_{spring} associated with that angle.

2.6.6 Force-deformation curves

The force-deformation behavior of the ssDNA springs were investigated by applying an equal and opposite force to their two ends (terminal beads representing the two end phosphate groups in the oxDNA model) along their end-to-end vector (see Figure 2.8a, bottom). The force-extension curve was obtained by averaging the end-to-end distance measured over a 100 ns-long MD simulation at different applied forces. Similarly, the force-deformation behavior of the springless hinge was investigated by applying inward-pointing forces to the ends of the dsDNA helices at locations where they were connected to springs in the original hinge. The hinge bending angle was averaged over 100 ns-long MD simulations at each combination of forces applied to the three lower and upper layers of dsDNA helices (see Figure 2.8a, top).

2.6.7 Simulation codes and data

Files related to oxDNA simulations of the DNA hinges are provided at our github clone (<https://github.com/gauravarya77/DNA-hinge-simulations>). These include: caDNAno design files of the hinges; Python scripts for converting caDNAno designs into initial oxDNA models and for substituting stretched bonds with harmonic restraints to generate relaxed configurations of the hinges; input option files for carrying out the relaxation procedure and the MD simulations; input topology and configuration files for the five hinges; and movie showing 100- μ s-long dynamics of a 0b hinge captured from an MD simulation.

2.7 Acknowledgements

Chapter 2, in full, is a reprint of the material as it appears in ACS Nano 2017, Shi, Ze; Castro, Carlos E.; Arya, Gaurav. The dissertation author was the primary investigator and author of this paper.

2.8 Appendix

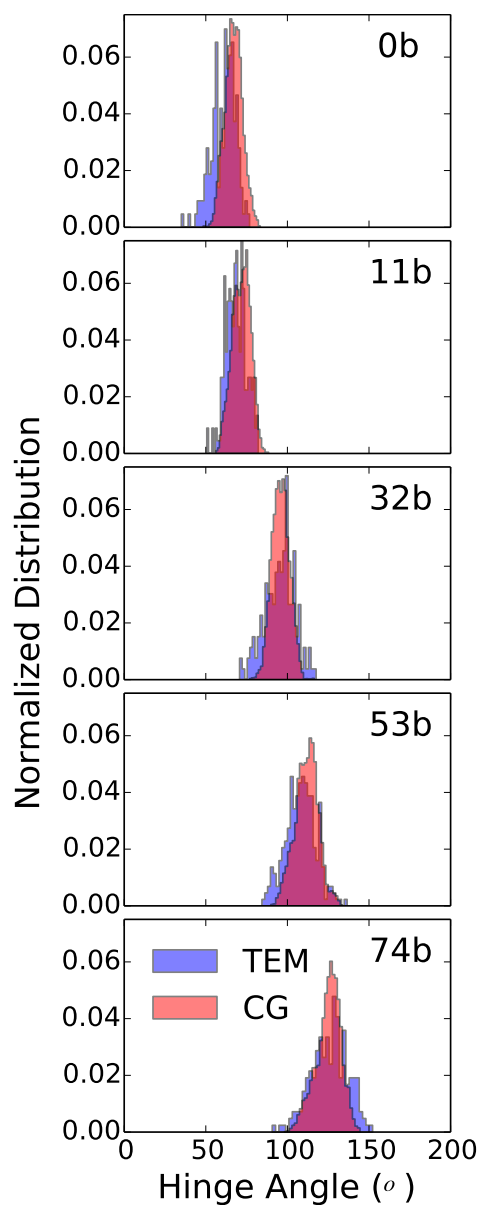


Figure 2.11: Normalized distributions of hinge angles Φ for the five hinge designs from CG modeling (red) and compared against those obtained from experimental TEM images (blue).

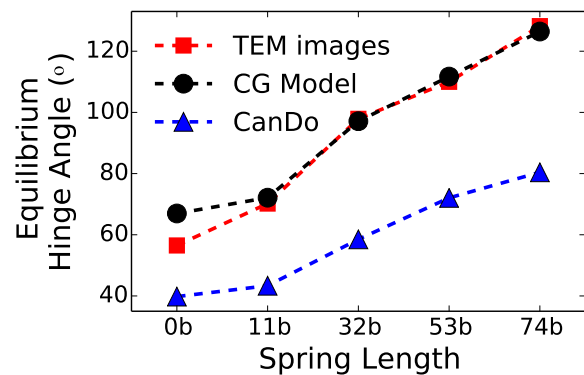


Figure 2.12: Equilibrium hinge angles Φ_0 for the five hinge designs predicted using the software CanDo. The angles predicted from the CG model and those obtained from experiments are shown as reference.

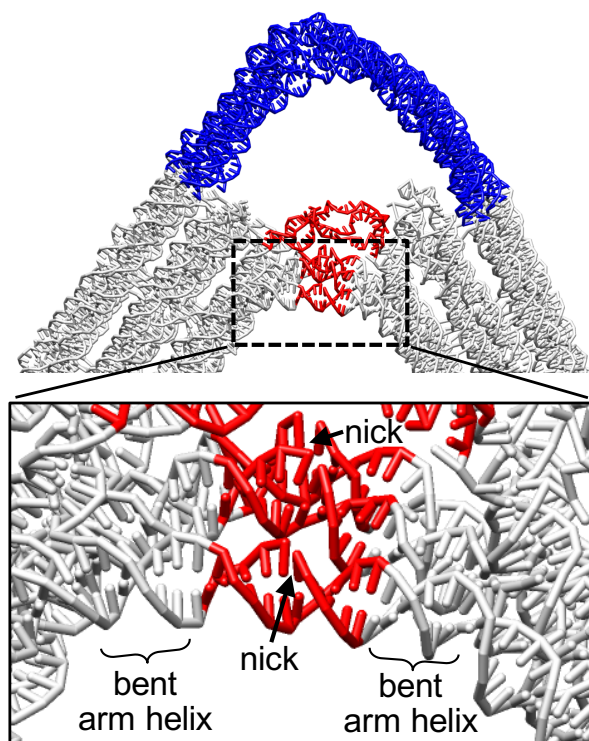


Figure 2.13: Representative snapshot of the joint (blue) and the springs (red) for the 0b hinge obtained from MD simulations illustrating how the three springs connecting the lower layer of hinge arm helices are effectively dsDNA helices containing single nicks and how the strong bending stress in these nicked dsDNA connections force the hinge arm helices to deform.

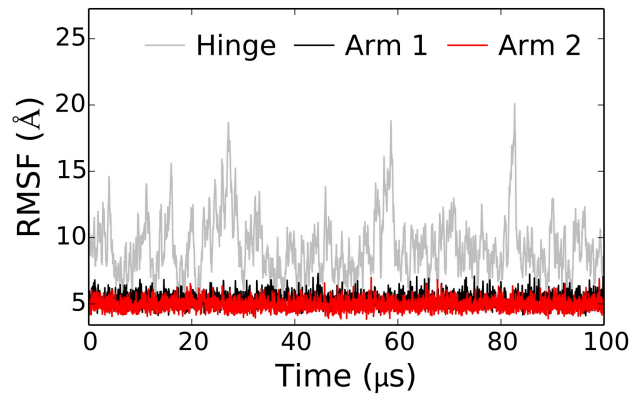


Figure 2.14: Root mean square fluctuations (RMSF) of the entire 0b hinge and of its two arms individually. The RMSFs are calculated relative to the average structures obtained over the entire MD trajectory.

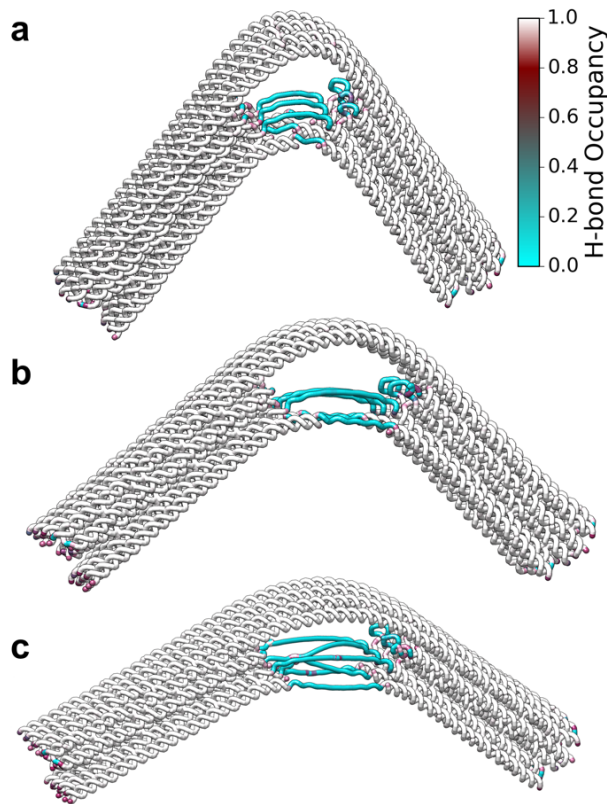


Figure 2.15: DNA-backbone representation of (a) 11b, (b) 32b, and (c) 53b hinges, colored according to the fraction of the time their nucleotide bases remain bonded to their complementary bases (H-bond occupancy). Cyan-, red-, and white-colored regions indicate unpaired, weakly paired, and strong paired bases.

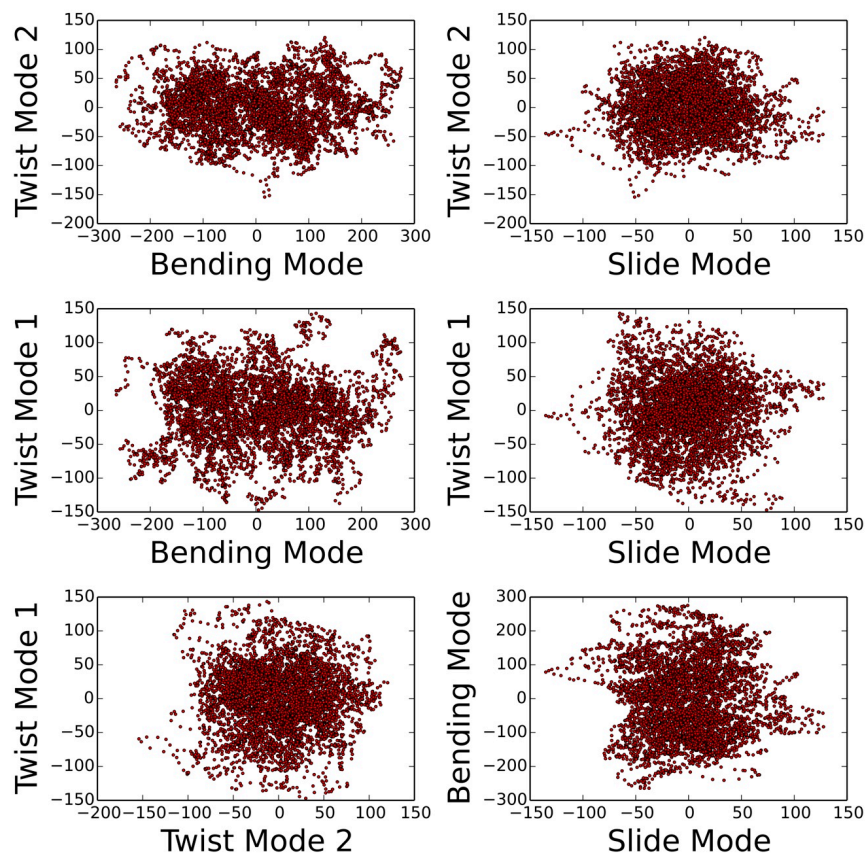


Figure 2.17: Correlation between the four largest dynamic modes of the 74b hinge obtained from principal component analysis. The x - and y -axes show the magnitude of the projections.

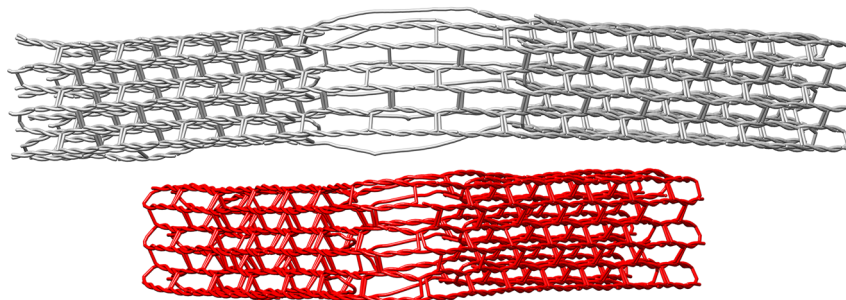


Figure 2.18: Average structure of the 74b (top) and 0b hinge (bottom) depicting the expulsion of the ssDNA springs in the former due to electrostatic repulsion. Hinges are represented by lines connecting the center of masses of the DNA bases and only their top view is shown.

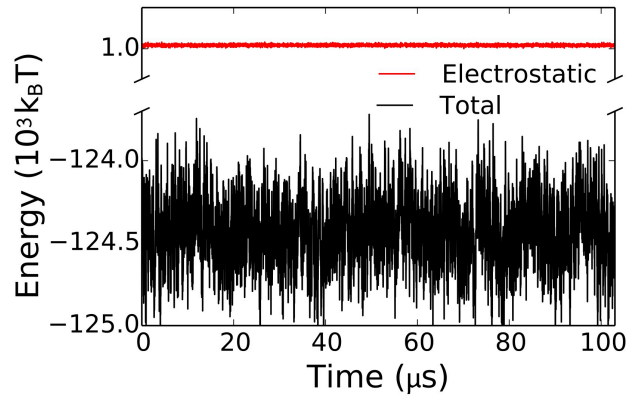


Figure 2.19: Total potential energy and the component of this energy arising purely from electrostatic repulsion plotted as a function of simulation time for the 0b hinge.

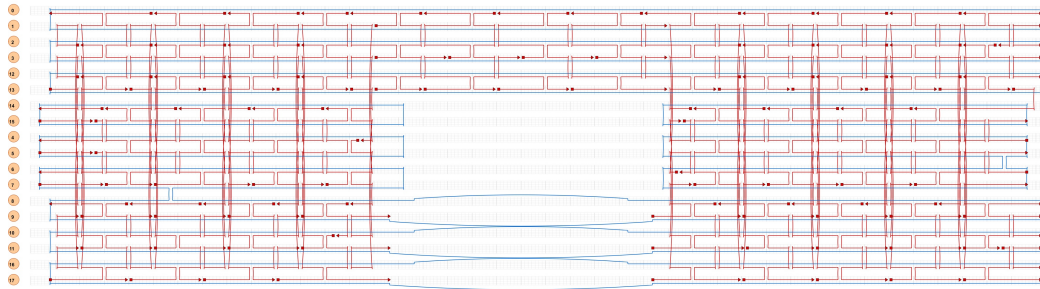


Figure 2.20: caDNANO design of the 0b hinge. The ssDNA scaffold and staple strands are shown in blue and red, respectively. The dsDNA helices are labeled 0 to 17 on the left.

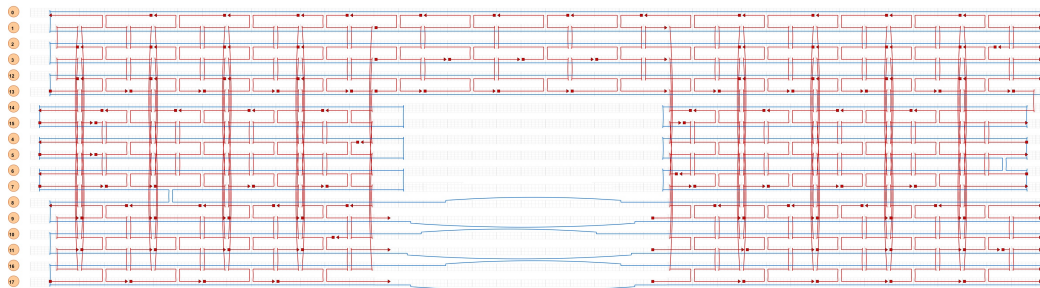


Figure 2.21: caDNANO design of the 11b hinge. The ssDNA scaffold and staple strands are shown in blue and red, respectively. The dsDNA helices are labeled 0 to 17 on the left.

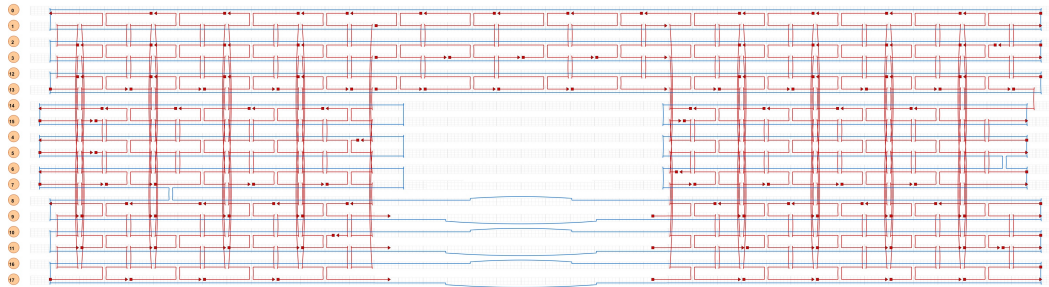


Figure 2.22: caDNAno design of the 32b hinge. The ssDNA scaffold and staple strands are shown in blue and red, respectively. The dsDNA helices are labeled 0 to 17 on the left.

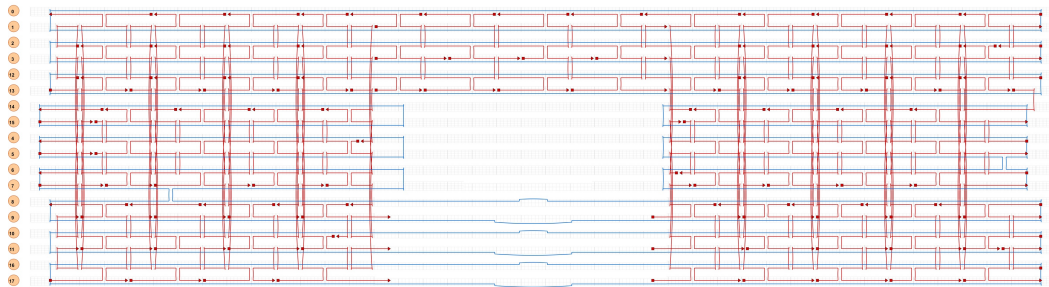


Figure 2.23: caDNAno design of the 53b hinge. The ssDNA scaffold and staple strands are shown in blue and red, respectively. The dsDNA helices are labeled 0 to 17 on the left.

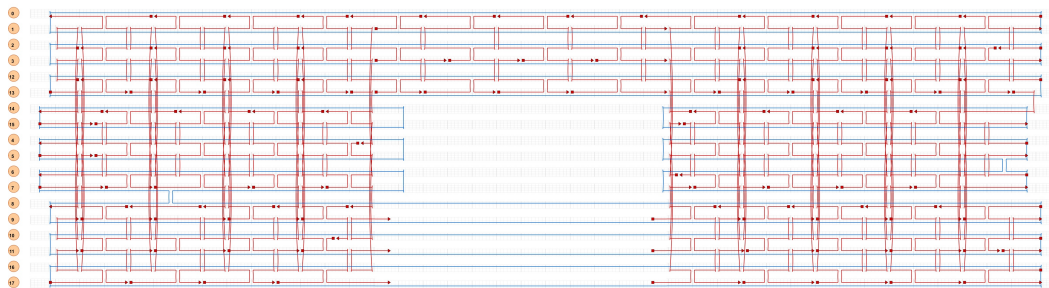


Figure 2.24: caDNAno design of the 74b hinge. The ssDNA scaffold and staple strands are shown in blue and red, respectively. The dsDNA helices are labeled 0 to 17 on the left.

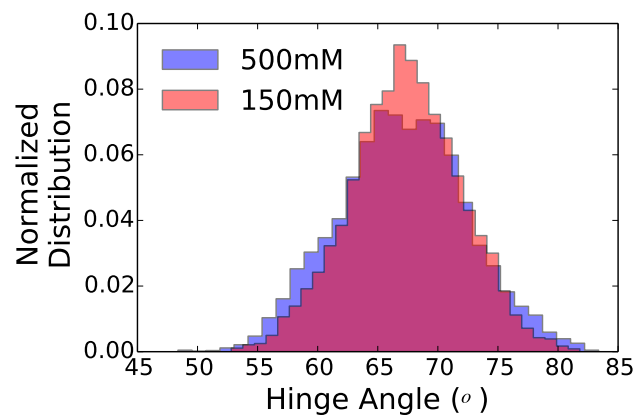


Figure 2.25: Hinge angle distribution of the 0b hinge obtained from CG MD simulations at two different monovalent salt concentrations: 150 mM (red) and 500 mM (blue).

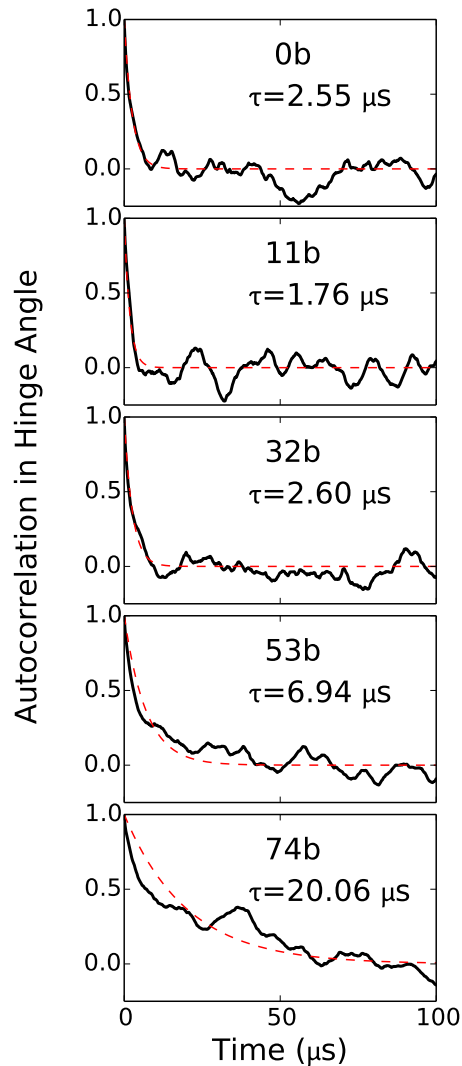


Figure 2.26: Autocorrelations $\langle(\Phi(t) - \Phi_0)(\Phi(0) - \Phi_0)\rangle$ in the hinge angle computed from CG MD simulations for the five hinge designs (solid black lines) along with exponential fits to the decaying portion of the curves (dashed red lines). The characteristic decay time constants obtained from the fits are also specified in each figure.

2.9 References

- [1] P. W. K. Rothmund, “Folding DNA to Create Nanoscale Shapes and Patterns.,” *Nature*, vol. 440, no. 7082, pp. 297–302, 2006.
- [2] D. Liu, S. H. Park, J. H. Reif, and T. H. LaBean, “DNA nanotubes self-assembled from triple-crossover tiles as templates for conductive nanowires.,” *Proc. Natl. Acad. Sci. U. S. A.*, vol. 101, no. 3, pp. 717–722, 2004.

- [3] H. Joshi, A. Dwaraknath, and P. K. Maiti, “Structure, stability and elasticity of DNA nanotubes.,” *Phys. Chem. Chem. Phys.*, vol. 17, no. 2, pp. 1424–1434, 2014.
- [4] R. Jungmann, M. Scheible, A. Kuzyk, G. Pardatscher, C. E. Castro, and F. C. Simmel, “DNA origami-based nanoribbons: assembly, length distribution, and twist.,” *Nanotechnology*, vol. 22, p. 275301, jul 2011.
- [5] S. Hernández-Ainsa, K. Misiunas, V. V. Thacker, E. a. Hemmig, and U. F. Keyser, “Voltage-dependent properties of DNA origami nanopores,” *Nano Lett.*, vol. 14, pp. 1270–1274, 2014.
- [6] H. Bui, C. Onodera, C. Kidwell, Y. Tan, E. Graugnard, W. Kuang, J. Lee, W. B. Knowlton, B. Yurke, and W. L. Hughes, “Programmable periodicity of quantum dot arrays with DNA origami nanotubes,” *Nano Lett.*, vol. 10, no. 9, pp. 3367–3372, 2010.
- [7] B. Ding, Z. Deng, H. Yan, S. Cabrini, R. N. Zuckermann, and J. Bokor, “Gold Nanoparticle Self-similar Chain Structure Organized by DNA Origami.,” *J. Am. Chem. Soc.*, vol. 132, no. 10, pp. 3248–3249, 2010.
- [8] W. Sun, E. Boulais, Y. Hakobyan, W. L. Wang, A. Guan, M. Bathe, and P. Yin, “Casting inorganic structures with DNA molds.,” *Science (80-.)*, vol. 346, no. 6210, p. 1258361, 2014.
- [9] R. M. Zadegan, M. D. E. Jepsen, K. E. Thomsen, A. H. Okholm, D. H. Schaffert, E. S. Andersen, V. Birkedal, and J. Kjems, “Construction of a 4 zeptoliters switchable 3D DNA box origami.,” *ACS Nano*, vol. 6, no. 11, pp. 10050–10053, 2012.
- [10] S. M. Douglas, I. Bachelet, and G. M. Church, “A Logic-Gated Nanorobot for Targeted Transport of Molecular Payloads,” *Science (80-.)*, vol. 335, p. 831, feb 2012.
- [11] S. M. Douglas, A. H. Marblestone, S. Teerapittayanon, A. Vazquez, G. M. Church, and W. M. Shih, “Rapid prototyping of 3D DNA-origami shapes with caDNAo,” *Nucleic Acids Res.*, vol. 37, no. 15, pp. 5001–5006, 2009.
- [12] S. Williams, K. Lund, C. Lin, P. Wonka, S. Lindsay, and H. Yan, “Tiamat: A three-dimensional editing tool for complex DNA structures,” *Lect. Notes Comput. Sci. (including Subser. Lect. Notes Artif. Intell. Lect. Notes Bioinformatics)*, vol. 5347 LNCS, pp. 90–101, 2009.
- [13] C. E. Castro, F. Kilchherr, D.-N. Kim, E. L. Shiao, T. Wauer, P. Wortmann, M. Bathe, and H. Dietz, “A primer to scaffolded DNA origami.,” *Nat. Methods*, vol. 8, no. 3, pp. 221–229, 2011.
- [14] D.-N. N. Kim, F. Kilchherr, H. Dietz, and M. Bathe, “Quantitative Prediction of 3D Solution Shape and Flexibility of Nucleic Acid Nanostructures.,” *Nucleic Acids Res.*, vol. 40, no. 7, pp. 2862–2868, 2012.

- [15] R. Veneziano, S. Ratanalert, K. Zhang, F. Zhang, H. Yan, W. Chiu, and M. Bathe, “Designer nanoscale DNA assemblies programmed from the top down.,” *Science* (80-.), vol. 352, p. 1534, jun 2016.
- [16] T. Liedl, B. Högberg, J. Tytell, D. E. Ingber, and W. M. Shih, “Self-assembly of three-dimensional prestressed tensegrity structures from DNA.,” *Nat. Nanotechnol.*, vol. 5, no. 7, pp. 520–524, 2010.
- [17] A. E. Marras, L. Zhou, H.-J. Su, and C. E. Castro, “Programmable motion of DNA origami mechanisms.,” *Proc. Natl. Acad. Sci. U. S. A.*, vol. 112, no. 3, pp. 713–718, 2015.
- [18] L. Zhou, A. E. Marras, H. J. Su, and C. E. Castro, “DNA origami compliant nanostructures with tunable mechanical properties,” *ACS Nano*, vol. 8, no. 1, pp. 27–34, 2014.
- [19] L. Zhou, A. E. Marras, H. J. Su, and C. E. Castro, “Direct design of an energy landscape with bistable DNA origami mechanisms,” *Nano Lett.*, vol. 15, no. 3, pp. 1815–1821, 2015.
- [20] E. F. Pettersen, T. D. Goddard, C. C. Huang, G. S. Couch, D. M. Greenblatt, E. C. Meng, and T. E. Ferrin, “UCSF Chimera - A visualization system for exploratory research and analysis,” *J. Comput. Chem.*, vol. 25, pp. 1605–1612, oct 2004.
- [21] R. M. Harrison, F. Romano, T. E. Ouldridge, A. A. Louis, and J. P. K. Doye, “Coarse-grained modelling of strong DNA bending I: Thermodynamics and comparison to an experimental molecular vice,” *arXiv Prepr. arXiv1506.09008*, vol. 1, 2015.
- [22] W. K. Olson and V. B. Zhurkin, “Working the kinks out of nucleosomal DNA,” *Curr. Opin. Struc. Biol.*, vol. 21, no. 3, pp. 348–357, 2011.
- [23] H. Asanuma, X. Liang, H. Nishioka, D. Matsunaga, M. Liu, and M. Komiyama, “Synthesis of azobenzene-tethered DNA for reversible photo-regulation of DNA functions: hybridization and transcription,” *Nat. Protoc.*, vol. 2, no. 1, pp. 203–212, 2007.
- [24] J. M. Abendroth, O. S. Bushuyev, P. S. Weiss, and C. J. Barrett, “Controlling Motion at the Nanoscale: Rise of the Molecular Machines,” *ACS Nano*, vol. 9, no. 8, pp. 7746–7768, 2015.
- [25] B. J. Grant, A. P. C. Rodrigues, K. M. ElSawy, J. A. McCammon, and L. S. D. Caves, “Bio3d: An R package for the comparative analysis of protein structures,” *Bioinformatics*, vol. 22, no. 21, pp. 2695–2696, 2006.

Chapter 3

Cation-Activated Avidity for Rapid Reconfiguration of DNA Nanodevices

3.1 Abstract

The ability to design and control DNA nanodevices with programmed conformational changes has established a foundation for molecular scale robotics with applications in nanomanufacturing, drug delivery, and controlling enzymatic reactions. The most commonly used approach for actuating these devices, DNA binding and strand displacement, allows devices to respond to molecules in solution, but this approach is limited to response times of minutes or greater. Recent advances have enabled electrical and magnetic control of DNA structures with sub-second response times, but these methods utilize external components with additional fabrication requirements. Here, we present a simple, broadly applicable, actuation method based on the avidity of many weak base-pairing interactions that respond to changes in local ionic conditions to drive large-scale conformational transitions in devices on sub-second timescales. To demonstrate such ion-mediated actuation, we modified a DNA origami hinge with short, weakly complementary single-stranded DNA overhangs whose hybridization is sensitive to cation concentrations in solu-

tion. We triggered conformational changes with several different types of ions including mono-, di-, and tri-valent ions, and also illustrated the ability to engineer the actuation response with design parameters, such as number and length of DNA overhangs and hinge torsional stiffness. We developed a statistical mechanical model that agrees with experimental data, enabling effective interpretation and future design of ion-induced actuation. Our results advance capabilities for rapid control of DNA nanodevices, expand the range of triggering mechanisms, and demonstrate DNA nanomachines with tunable analog responses to the local environment.

3.2 Introduction

Controlling the motion of nanoscale structures is an essential step towards developing functional nanodevices and nanorobots that can have broad applications in fields ranging from nanomanufacturing to medicine. Recent advancements in DNA nanotechnology have led to complex nanoscale machinery and controllable dynamic devices including DNA walkers(1; 2; 3; 4), reconfigurable structures(5; 6; 7; 8; 9), mechanical joints with well-defined rotational or translational degrees of freedom(10; 11; 12; 13; 14; 15; 16; 17; 18; 19; 20; 21; 22; 23), and multi-joint mechanisms (10; 20; 24; 25). In some cases, these devices can be moved along a predefined motion path(13; 3; 13; 18; 20) or flipped between conformations(13; 16; 17; 20; 24), showing promise for complex controllable DNA-based nanomachines.

While dynamic devices have rapidly evolved in structural and dynamic complexity over the last decade, methods for controlling such devices in a rapid and reproducible manner are lagging behind. The most commonly used method to control DNA devices, DNA strand displacement(7), involves mixing devices with single-stranded DNA (ssDNA) that reconfigures a device by selectively displacing strands. This displacement releases double-stranded DNA (dsDNA) connections between components on a device (*e.g.* a container and a lid). Often, the addition of another ssDNA strand that hybridizes to the displacement site can re-establish the dsDNA connection

enabling reversible and repeatable actuation(7; 26). The main advantages of strand displacement include the sequence-specificity, the relative ease of integrating DNA sites for actuation on a wide range of devices, and the potential to interface with molecular computation that relies on similar displacement reactions(10; 21; 26; 27). However, this approach is limited by the relatively slow time-scales of actuation, typically minutes or longer. To address these challenges and to broaden the range of triggering mechanisms, recent efforts have demonstrated actuation using various biomolecules(16; 27; 28; 29; 30; 31), often using DNA aptamers for target specificity(16; 27; 30; 32). Applying forces through optical traps, atomic force microscopy, and centrifuge force microscopy have also been explored as possible mechanisms for manipulating DNA structures(33; 32; 34; 35; 36; 37). In addition, electrical(38) and magnetic(39) actuation methods have been implemented to enable control at sub-second timescales and in the case of the electrical actuation control at speeds up to tens of Hz. These approaches require external inputs and some advanced system or assay fabrication.

Many applications, for instance in biomedicine, may require less invasive approaches for actuation or devices that can respond to a variety of cues in the local environment. Indeed, emerging studies have begun to actuate DNA nanostructures using light and environmental changes such as temperature, pH, and ion concentrations, through the incorporation of azobenzene moieties(40; 41), DNA base-stacking interactions(13), G-quadruplexes(16), and DNA triplex-forming motifs(42) into the DNA nanostructures. In particular, Kuzyk *et al.* developed a pH-triggered mechanism demonstrating the ability to engineer range of sensitivity, and Gerling *et al.*(13) developed ion-based actuation of dynamic devices that mediated base-stacking interactions within the devices. Both studies used bulk fluorescence methods to demonstrate response on 10 second timescales.

Here we introduce a simple and tunable strategy for rapid actuation of DNA nanostructures featuring sub-second transitions and second-scale temporal resolution of repeated actuation as revealed by single-molecule measurements of triggered conformational changes. Our method

combines an engineered response to environmental changes with sequence- specificity of DNA hybridization for reconfiguring structures. We achieve this by modifying DNA structures with short ssDNA sticky ends that rapidly hybridize or de-hybridize in response to changes in concentration of specific cations, enabling large-scale reconfiguration of structures within short timescales. We demonstrate the utility of this approach by actuating DNA hinge nanodevices using several different cations, achieving reversible and repeatable opening and closing of hinge arms within sub-second timescales. We further show the ability to tune the actuation response, and to quantitatively model its behavior as a function of cation concentration and a number of design parameters, thereby providing a rational means to engineer the sensitivity and range of the actuation response. Given the straightforward and inexpensive incorporation of ssDNA overhangs, this approach is readily extendable to a variety of devices. In addition to actively actuating nanodevices, this approach may also be used in a passive form, for instance, as calibrated sensors to measure ion concentrations. The method presented here should therefore provide a valuable tool for researchers aiming to introduce dynamical mechanisms into otherwise static DNA nanostructures.

The overarching principle of our actuation method, similar to that of many existing approaches, is a switchable affinity between structural components that can be turned on or off via addition or removal of an external trigger, enabling structures to be actuated between conformations with well-separated (open state) and latched together components (closed states). In our approach, the affinity is generated by introducing a number of short, mutually complementary ssDNA strands (overhangs) across the surfaces of the components to be actuated. The overhang sequence can be added to the end of an existing staple at the appropriate spatial position and helical twist orientation to ensure that the overhangs protrude from the surface in an appropriate location and direction to bind to its complementary strand on the opposing surface. In contrast to prior approaches that leverage base-pairing interactions, we use short overhang sequences, that individually are too weak to stably hybridize at room temperature. However, the collec-

tive binding energy of many distributed overhang binding sites (*i.e.* avidity) allows these short sequences to form connections between components that become thermodynamically stable at cation concentrations that are high enough to sufficiently screen electrostatic repulsions between the phosphate backbones of the interacting overhangs(43). Thus, by raising or lowering the cation concentration, the structure can be actuated to close or open, respectively. There are two key aspects of this approach that enable rapid actuation response. First, the actuating strands remain localized on the device, so they effectively remain at very high local concentrations. Second, the low affinity of individual strands means that they should quickly dissociate upon lowering cation concentrations without any need for strand displacement, which is a relatively slow process. This enables significantly faster actuation rates compared to methods where actuating strands are introduced into the solution, typically at sub-micromolar concentrations, and have to undergo a diffusive search process before hybridizing with their target. The only diffusive mechanism at play in our approach is that of the cations, which occurs at a faster timescale than strand diffusion due to their small size and much higher concentrations (mM instead of nM). Furthermore, the overhangs are likely to exhibit collective hybridization since they are aligned across the actuated components.

To demonstrate and characterize our ion-based actuation method, we applied it to a set of previously reported DNA origami hinges(20). The hinges are composed of two stiff arms, each a rectangular bundle of 18 dsDNA helices organized in a 3×6 square lattice cross-section(44). The arms are connected by several flexible ssDNA scaffold connections arranged in a line to form the hinge rotation axis. We previously showed 20 that the hinge arms rotate flexibly over a range of angles, exhibiting largely open conformations. To enable ion-triggered actuation between such open conformations and a closed conformation, we modified these hinges to include short ssDNA staple overhangs distributed along the inner face of each arm at complementary locations (Figure 3.1). In this study, we used a range of cationic triggers, and explored the use of 10 to 30 overhangs on each arm with sequence lengths ranging from 4 to 6 bases for both hinge designs

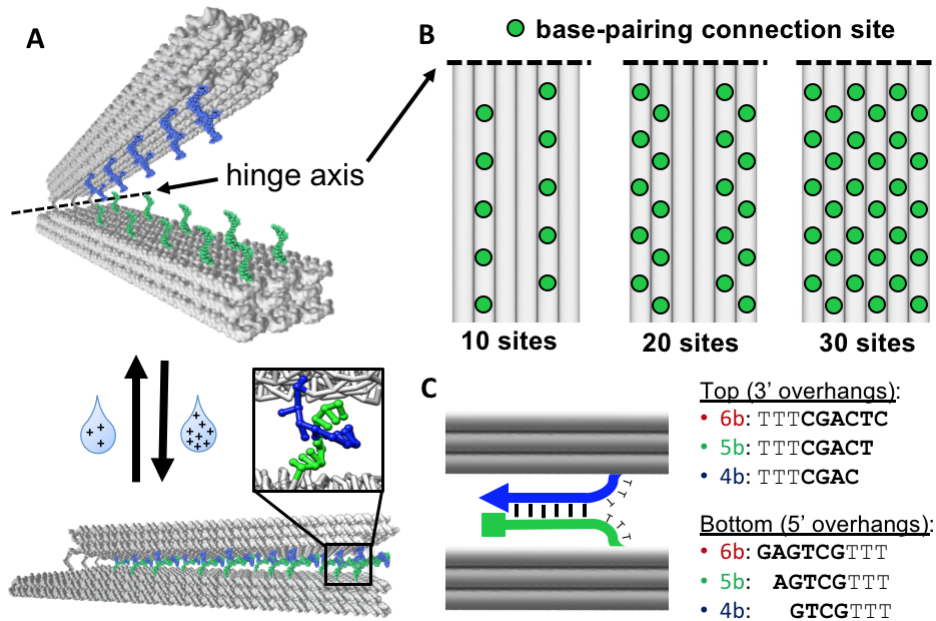


Figure 3.1: (A) Short ssDNA overhangs (blue and green) protrude from the hinge arms. Overhang sequences are complementary to each other but their free energy of hybridization is weak at low cation concentrations. Overhang hybridization is stabilized with increased cation concentration and the overhangs collectively bind to close the hinge. (B) Overhang locations on the hinge arms for the three designs containing different number (10, 20, and 30 pairs) of connections. (C) All overhangs include a TTT linker for separation from the hinge. Square represents the 5 end of the overhang, while the triangle represents the 3 end. Three different overhang lengths (4, 5, and 6 bases) were explored in this study.

(Figure 3.1). We also explored two versions of the hinges termed Hinge1 and Hinge2 that we previously showed(20) to differ in torsional stiffness of the hinge joint, with Hinge1 exhibiting a higher resistance to closing than Hinge2.

3.3 Cation-Activated Actuation.

The actuation behavior of the overhang-modified hinges is studied as a function of varying ion concentrations. Four design variables that modulate the actuation response of our devices are considered: the number of overhang connections, the strength of these connections (number of complementary base pairs across overhangs), the torsional stiffness of the hinge (Hinge1 versus

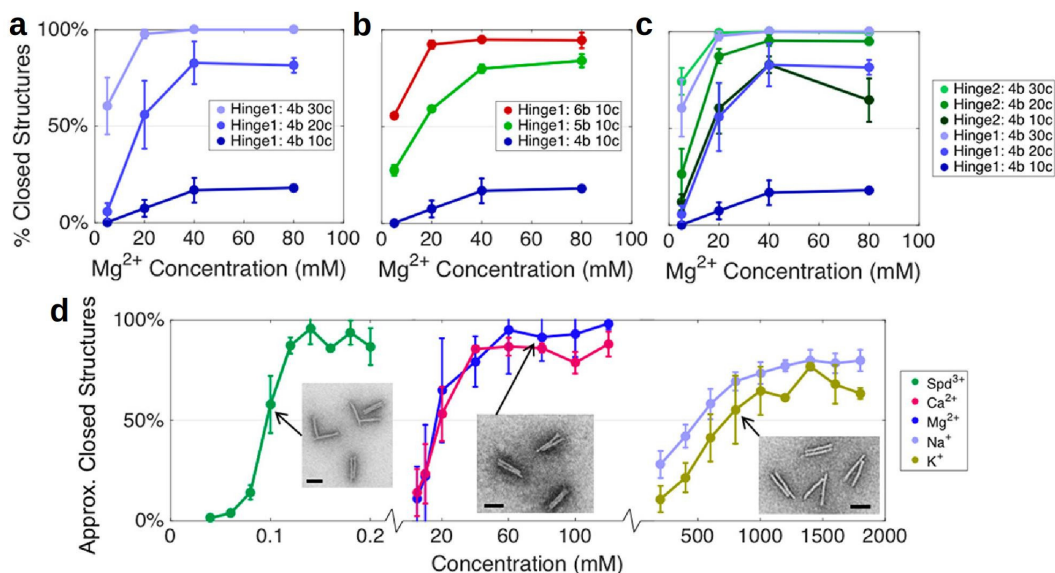


Figure 3.2: Experimental actuation responses measured as percentage of closed hinges vs ion concentration for a range of hinge designs and ions. The actuation responses are sensitive to **a** the number of overhang connections, **b** the length of overhangs, **c** the hinge stiffness, and **d** the valence charge of the cation. The first number in the data legends corresponds to the hinge design number, with Hinge1 being rotationally stiffer than Hinge2, the second number corresponds to the length of the overhangs (e.g., 4b \equiv 4 bases), and the last number denotes the number of connections (e.g., 10c implies 10 overhangs on the top arm and 10 complementary overhangs on the bottom arm). All hinges in panel D are Hinge2 with a total of 10 4-base connections. Data in panels a-c was measured via TEM. Data in panel d were obtained via ensemble FRET, while select samples were also counted from TEM. The TEM data were used to calculate a linear relationship between FRET efficiency and closed hinge fraction. Scale bars: 50 nm.

Hinge2), and the cation used. Magnesium was chosen to demonstrate the effects of the first three parameters because it is the most commonly used ion for stabilizing DNA origami (45; 46) and because it does not influence the energy landscape of the hinges as shown by our analysis above. Importantly, when constructing hinges with varying numbers and lengths of overhangs, we used the same base hinge design with the only changes being the selection of staple strands with and without overhang extensions at appropriate locations. We quantified the equilibrium actuation response of each of these hinges through TEM analysis by measuring the fraction of hinges that close as a function of varying ion concentrations in solution. Because completely

closed hinges are rarely achieved without overhangs, hinges that were actuated into a completely closed conformation were easy to distinguish from un-actuated hinges in TEM images.

Figure 3.2a shows the impact of changing the number of connections distributed across the hinge arms. These hinges all have 4-base overhangs and explore the full spectrum of conformational compositions ranging from 0% to 100% closed structures with 10 to 30 connections and 5 to 80 mM MgCl₂ concentrations. For each hinge, the fraction of closed structures rises sharply with increasing ion concentration at low concentrations before slowing down and saturating at higher concentrations to a plateau value indicative of the maximum yield of closed hinges attainable with that particular number and arrangement of weak connections. The actuation responses become sharper (*i.e.*, more sensitive to ion concentration) and yield higher fractions of closed structures (at all ion concentrations including saturation values) with increasing number of connections. Another design parameter that alters the sensitivity to ion concentrations is the length of the overhangs. Figure 3.2b shows this effect for various 10-connection hinges, where adjusting the overhang length from 4 to 6 bases leads to a sharper actuation response and higher yield of closed structures, effects similar to those obtained with increasing number of connections. Interestingly, the hinge with 10 5-base connections yields a similar saturation yield of closed hinges as the hinge with 20 4-base connections, but the 20 4-base connections exhibit a different sensitivity to ion concentration at low salt conditions. These results reveal an ability to engineer both the sensitivity and range of the actuation response.

Changing the number or length of connections are simple design parameters that are easily adjusted by substituting several staples in the hinge design during the self-assembly reaction. We also studied the effect of the torsional stiffness of the hinge, which determines its resistance to closing. Torsional stiffness was varied by altering the ssDNA joint connections using a different hinge design.⁽²⁰⁾ Figure 3.2c illustrates the effect of hinge stiffness on actuation using structures having four-base overhangs on each arm. Our results show that Hinge2, which has a lower stiffness than Hinge1, yields a steeper actuation response that is also shifted to lower ion

concentrations, suggesting that hinge stiffness is an additional design parameter that controls the range and sensitivity of the actuation response. In addition, these results illustrate that mechanical properties are a key consideration in determining device functional response.

3.4 Theoretical model of actuation response.

To explain the observed actuation behavior and its dependence on the hinge design parameters studied above, we developed a quantitative model that relates the probability, P_{closed} of observing a closed hinge to the ionic concentration c . The model classifies the ensemble of hinge conformations in terms of two states: a closed state describing conformations with sufficiently small hinge angles that permit overhang hybridization, and an open state describing all remaining conformations. According to equilibrium statistical mechanics, $P_{\text{closed}} = Z_{\text{closed}} / (Z_{\text{closed}} + Z_{\text{open}})$, where Z_{closed} and Z_{open} are the partition functions associated with the two states. Assuming that the n overhangs on each hinge arm are indistinguishable and that each overhang interacts only with its complementary counterpart on the opposite arm, Z_{closed} and Z_{open} can *each* be partitioned into two terms. The first is a bare-hinge partition function related to conformations of the hinge without overhangs in the two respective states. The second is a product of n identical overhang partition functions related to conformations of each pair of overhangs, *i.e.*, partly- to fully-hybridized conformations in the closed state and unassociated conformations in the open state. Relating the bare-hinge and overhang partition functions to free energy changes associated with bare-hinge rotation and strand hybridization then yields the following relationship:

$$P_{\text{closed}}(c) = \frac{\left[1 + \exp\left(-\frac{\Delta G_{\text{hyb}}(c) + \Delta G_{\text{fix}}}{RT}\right)\right]^n}{\left[1 + \exp\left(-\frac{\Delta G_{\text{hyb}}(c) + \Delta G_{\text{fix}}}{RT}\right)\right]^n + \exp\left(-\frac{\Delta G_{\text{bh}}}{RT}\right)}. \quad (3.1)$$

where $\Delta G_{\text{hyb}}(c)$ is the free energy of hybridization of each overhang pair *in solution*, ΔG_{fix} is a correction to this free energy that accounts for entropy loss due to the confinement from the

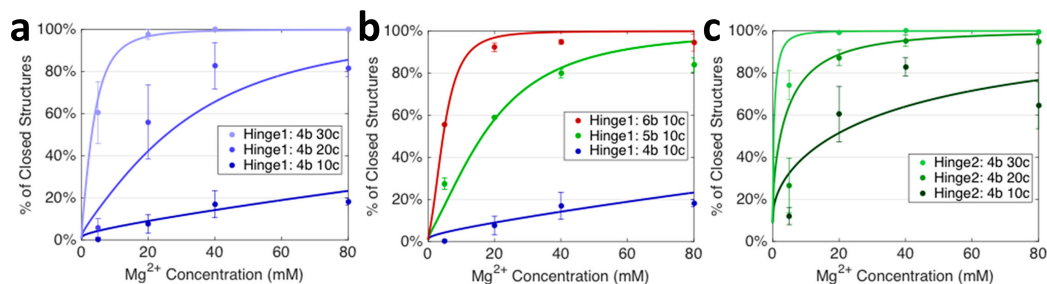


Figure 3.3: Model fits to experimental actuation response curves. Experimental data for different hinge designs are shown in symbols, and the model fits are shown as solid lines of same color as the fitted data. The data legends format is identical to that in Figure 2, where the three numbers correspond to the hinge design, the length of the overhangs, and the number of connections. The fitting procedure yielded $\Delta G_{bh} = 2.80$ and 1.39 kcal/mol for hinges with joint designs 1 and 2 and $\Delta G_{fix} = 6.07$, 6.12 , and 5.99 kcal/mol for hinges with 10, 20, and 30 overhang pairs, each with 4 complementary bases, and $\Delta G_{fix} = 7.35$ and 8.24 kcal/mol for hinges with 10 overhang pairs with 5 and 6 complementary bases, respectively.

hinge arms, ΔG_{bh} is the free energy change of a *bare* hinge undergoing transition from an open to a closed state, R is the universal gas constant, and T is the temperature. A detailed derivation of this relationship is provided in the model development section. Based on known logarithmic dependence of ΔG_{hyb} on ion concentration (47; 48), the above model predicts that the fraction of closed hinges rises from a value of $P_{closed} = [1 + \exp\left(-\frac{\Delta G_{bh}}{RT}\right)]^{-1}$ at $c = 0$ to the asymptotic value of 1 at $c \rightarrow \infty$. This prediction agrees well with the shape of the experimentally observed actuation responses. The functional form of the model further predicts that strongly negative $\Delta G_{hyb} + \Delta G_{fix}$ (long overhangs), large n (many overhangs), and small ΔG_{bh} (small energy barrier for bare hinge closing) all contribute to increasing ion-sensitivity of the hinges, also consistent with the experimentally observed trends.

Finally, the model suggests that to shift the range of the actuation response to higher ion concentrations, the energy barrier between the closed and open state of the bare hinge should be sufficiently large. The functional form of our model is thus already capable of qualitatively explaining the observed actuation behavior and demonstrating the crucial roles of both the hinge joint and the overhangs in sharpness and range of the actuation responses.

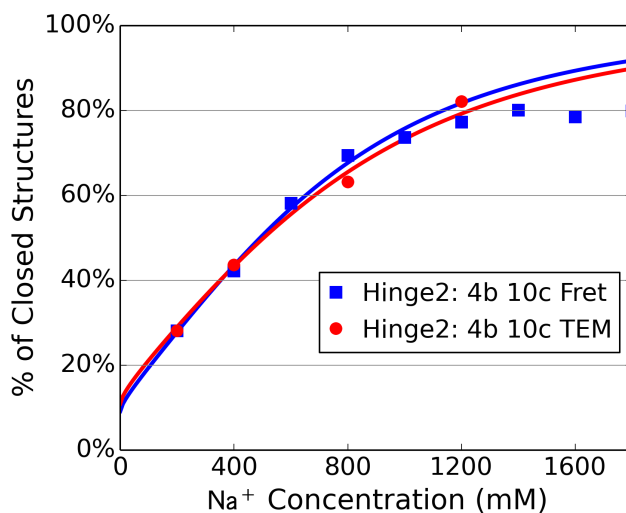


Figure 3.4: Model fits to actuation responses obtained with NaCl. Data collected via FRET and TEM visualization are both shown and fitted separately. Different sets of ΔG_{hyb} data are obtained from UNAFold for Na^+ ions. The fitting procedure yielded $\Delta G_{\text{bh}} = 1.24$ and 1.36 kcal/mol and $\Delta G_{\text{fix}} = 6.18$ and 6.11 kcal/mol for Hinge2 data collected from FRET and TEM data, respectively.

We next investigated the ability of this model to quantitatively fit the experimental actuation responses shown in symbols in Figure 3.3 for the eight distinct hinge designs differing in terms of the number of overhangs, overhang lengths, and hinge stiffness. This data obtained using MgCl_2 represents our broadest dataset and also shows minimal changes to the intrinsic free energy landscape across a wide range of concentrations (Figure S2). Furthermore, the solution-state free energies of hybridization ΔG_{hyb} are readily available for Mg^{2+} as a function of its concentration. In this study, we obtained these free energies from the DINAMelt server, part of the DNA/RNA secondary structure prediction software UNAFold(47; 48). We then minimized the weighted sum of squared errors between the model and experimental data, varying the two remaining unknown parameters ΔG_{bh} and ΔG_{fix} . ΔG_{bh} was kept unchanged across hinges with the same joint stiffness, and ΔG_{fix} was kept unchanged across hinges carrying the same number and length of overhangs. Figure 3.3 presents our results from simultaneous fitting of all actuation profiles. A p-value of 0.993 for the chi-square test indicates excellent agreement between model

and experiment, especially considering that the two fit parameters were fixed across groups of hinges with similar stiffness or overhang lengths. The model also accurately predicts the NaCl actuation response (Figure 3.4).

The fitted values of ΔG_{bh} and ΔG_{fix} obtained for the different hinge designs make physical sense. We obtained $\Delta G_{\text{bh}} = 2.80$ and 1.39 kcal/mol for Hinge1 and Hinge2. The positive values of ΔG_{bh} are consistent with the open state being more prevalent than the closed state in bare hinges (see Figures S2-S3), and the larger value for Hinge1 is consistent with stiffer hinges displaying a larger energetic penalty for closing. Furthermore, the free energy difference obtained for Hinge1 is close to the value of 3.59 kcal/mol estimated from our experimental angular distributions using the ratio between numbers of bare hinge configurations presenting open and closed states with a threshold of 10, *i.w.*, $\Delta G_{\text{bh}} RT \ln(N_{\text{open}}/N_{\text{closed}})$ (see Figure 3.5).

We obtained $\Delta G_{\text{fix}} = 6.07, 6.12,$ and 5.99 kcal/mol for hinges with 10, 20, and 30 overhang pairs with 4 complementary bases, and 7.35 and 8.24 kcal/mol for hinges with 10 overhang pairs with 5 and 6 complementary bases, respectively. The positive values of ΔG_{fix} are reasonable considering that the hybridization of overhangs is impaired due to confinement effects, that is, the steric constraints imposed by the hinge arms significantly reduce the configurational and rotational entropy of the overhangs in the hinge closed state. We also note that ΔG_{fix} is largely independent of the number of overhangs on each hinge arm, suggesting that the overhang length and surface density are sufficiently small that they do not interact with each other, consistent with one of the assumptions of our model. That ΔG_{fix} increases in magnitude with the degree of complementarity (length of overhangs) suggests that the entropic penalty imposed by the arms on the overhangs is stronger for longer strands.

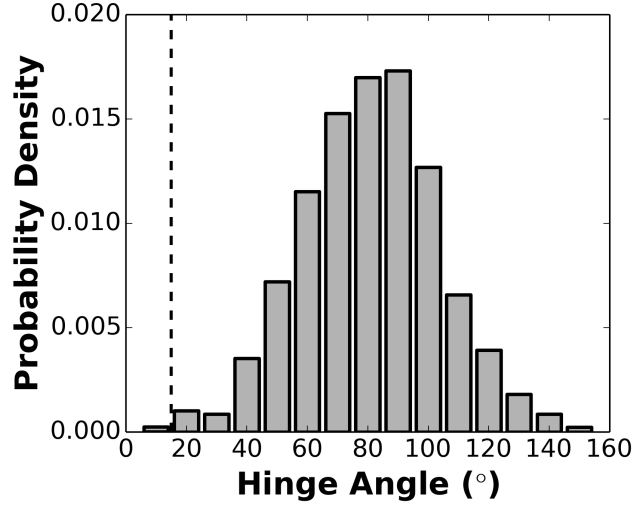


Figure 3.5: Cumulative angular distribution for Hinge1 in MgCl_2 solutions. The free energy change required to close Hinge1 is approximated from the ratio $N_{\text{open}}/N_{\text{closed}} \approx 425$ between numbers of bare hinge configurations representing open and closed states with a threshold of 10° (dashed vertical line).

3.5 Model Development

The probability P_{closed} of the hinge exhibiting a closed state may be obtained from the partition functions Z_{closed} and Z_{open} of the closed and open states: (55).

$$P_{\text{closed}} = \frac{Z_{\text{closed}}}{Z_{\text{closed}} + Z_{\text{open}}}, \quad (3.2)$$

where the two partition functions, by definition, are given by

$$Z_{\text{closed}} = \sum_{\mathbf{r}_h, \mathbf{r}_s \in \text{closed}} \exp[-E(\mathbf{r}_h, \mathbf{r}_s)/RT], \quad (3.3)$$

$$Z_{\text{open}} = \sum_{\mathbf{r}_h, \mathbf{r}_s \in \text{open}} \exp[-E(\mathbf{r}_h, \mathbf{r}_s)/RT], \quad (3.4)$$

Here, R is the gas constant, T is the temperature, and $E(\mathbf{r}_h, \mathbf{r}_s)$ is the total energy of the hinge, which is a function of the set of coordinates \mathbf{r}_h describing the conformation of the bare hinge

(without ssDNA overhangs) and the coordinates \mathbf{r}_s describing the conformation of all ssDNA overhangs. The summations in Equation 3.3 and 3.4 are carried out over the ensemble of hinge conformations belonging to the closed and open states.

We next make the assumption that the total energy of the hinge can be effectively decoupled into an energy term E_h that is the function of the bare hinge conformation alone and another energy term E_s that is a function of the ssDNA overhang conformations only:

$$E(\mathbf{r}_h, \mathbf{r}_s) \approx E_h(\mathbf{r}_h) + E_s(\mathbf{r}_s) \quad (3.5)$$

This assumption, implemented in many statistical mechanical models, allows the overall partition functions in Equation 3.3 and 3.4 to be written as the product of the partition function of the two subsystems (the bare hinges and the overhangs):

$$Z_{\text{closed}} = Z_{h,\text{closed}} \times Z_{s,\text{closed}}, \quad (3.6)$$

$$Z_{\text{open}} = Z_{h,\text{open}} \times Z_{s,\text{open}}, \quad (3.7)$$

where $Z_{h,\text{closed}}$ and $Z_{s,\text{closed}}$ are the partition functions of the closed state of bare hinge and the overhang strands, and $Z_{h,\text{open}}$ and $Z_{s,\text{open}}$ are the partition functions of the open state of the two subsystems:

$$Z_{h,\text{closed}} = \sum_{\mathbf{r}_h \in \text{closed}} \exp[-E(\mathbf{r}_h)/RT], Z_{s,\text{closed}} = \sum_{\mathbf{r}_s \in \text{closed}} \exp[-E(\mathbf{r}_s)/RT], \quad (3.8)$$

$$Z_{h,\text{open}} = \sum_{\mathbf{r}_h \in \text{open}} \exp[-E(\mathbf{r}_h)/RT], Z_{s,\text{open}} = \sum_{\mathbf{r}_s \in \text{open}} \exp[-E(\mathbf{r}_s)/RT]. \quad (3.9)$$

By recognizing that the ratio $Z_{h,\text{closed}}/Z_{h,\text{open}}$ is intrinsically related to the free energy change of the *bare hinge* undergoing transition from the open to the closed state via

$$\Delta G_{\text{bh}} = -RT \ln(Z_{h,\text{closed}}/Z_{h,\text{open}}), \quad (3.10)$$

the expression for the closed state probability in Equation 1 can now be simplified based on Equations 3.6, 3.7, and 3.10 to

$$P_{close} = \frac{(Z_{h,closed}/Z_{h,open})}{(Z_{h,closed}/Z_{h,open}) + \exp(-\frac{\Delta G_{bh}}{RT})}, \quad (3.11)$$

where the free energy change ΔG_{bh} is assumed to be largely independent of Mg^{2+} concentration, based on our experimental observations.

To estimate the ratio of the overhang partition functions in Equation 3.11, we assume that each overhang, out of a total of n overhangs per hinge arm, can interact and hybridize only with its corresponding overhang on the other hinge arm and that the n pairs of overhangs are identical but distinguishable from each other. In this ideal scenario, the partition functions $Z_{s,closed}$ and $Z_{s,open}$ for a system of n pairs of overhangs can be written down in terms of the partition functions $Z_{s,closed}^{(1)}$ and $Z_{s,open}^{(1)}$ for a single pair of overhangs:

$$\frac{Z_{s,closed}}{Z_{s,open}} = \left(\frac{Z_{s,closed}^{(1)}}{Z_{s,open}^{(1)}} \right)^n, \quad (3.12)$$

where $Z_{s,closed}^{(1)}$ sums over all possible conformations of the two overhangs in the dissociated state, while $Z_{s,open}^{(1)}$ sums over all possible conformations of the two overhangs in both hybridized and dissociated states. If one denotes the above sums over dissociated and hybridized states by Z_{dis} and Z_{hyb} , then

$$\frac{Z_{s,closed}}{Z_{s,open}} = \left(\frac{Z_{hyb} + Z_{dis}}{Z_{dis}} \right)^n, \quad (3.13)$$

where the ratio Z_{hyb}/Z_{dis} is related to the free energy of hybridization $\Delta G_{hyb,f}$ of a single pair of overhangs from the dissociated state while remaining fixed to the hinge arms:

$$\frac{Z_{hyb}}{Z_{dis}} = \exp\left(-\frac{\Delta G_{hyb,f}(c)}{RT}\right), \quad (3.14)$$

To obtain $\Delta G_{\text{hyb},f}$, one can take advantage of available DNA/RNA secondary-structure prediction algorithms that provide the free energy of hybridization of the overhangs in solution as a function of Mg^{2+} concentration, which we denote by $\Delta G_{\text{hyb}}(c)$. To account for the entropy loss due to the confinement from the hinge arms, we add a concentration-independent correction term ΔG_{fix} to this free energy, whereby

$$\Delta G_{\text{hyb},f}(c) = \Delta G_{\text{hyb}}(c) + \Delta G_{\text{fix}}. \quad (3.15)$$

Substituting Equations 3.13-15 into Equation 3.11 then yields our final expression for the closed-state probability given by

$$P_{\text{closed}}(c) = \frac{\left[1 + \exp\left(-\frac{\Delta G_{\text{hyb}}(c) + \Delta G_{\text{fix}}}{RT}\right)\right]^n}{\left[1 + \exp\left(-\frac{\Delta G_{\text{hyb}}(c) + \Delta G_{\text{fix}}}{RT}\right)\right]^n + \exp\left(-\frac{\Delta G_{\text{bh}}}{RT}\right)}. \quad (3.16)$$

with two unknown parameters ΔG_{fix} and ΔG_{bh} .

3.6 Analysis of the Range and Sharpness of Actuation

We further analyzed the analytical expression for P_{closed} and its dependence on the design parameters related to the ssDNA overhangs and bare hinges. For this purpose, we divided the solution-state hybridization free energy $\Delta G_{\text{hyb}}(c)$ into concentration-dependent and concentration-independent terms:

$$\Delta G_{\text{hyb}}(c) = -a_0 \ln c - b_0, \quad (3.17)$$

where a_0 and b_0 are positive parameters provided by the UNAFold package 48-49 related to the strength of hybridization between the two ssDNA overhangs. By defining $a \equiv a_0/RT$, $b \equiv \exp[(\Delta G_{\text{fix}} b_0)/RT]$, and $g \equiv \exp(\Delta G_{\text{bh}}/RT)$, the expression for the closed state probability in Equation 3.16 reduces to

$$P_{\text{closed}} = \frac{(1 + bc^a)^n}{(1 + bc^a)^n + g} \quad (3.18)$$

and its first derivative with respect to concentration is given by

$$\frac{dP_{\text{closed}}}{dc} = \frac{P(1-P)nab}{c^{1-a} + bc} \quad (3.19)$$

To obtain sharp actuation of the hinges, i.e., large change in P_{closed} over a small change in Mg^{2+} concentration, the derivative dP_{closed}/dc should be large. Based on the observed actuation behavior, it is reasonable to assume that the dP_{closed}/dc should be large at intermediate values of P_{closed} (e.g., 0.5). The expression in Equation 3.19 then suggests that the derivative dP_{closed}/dc is large when either n is large, i.e., the hinge arms are attached with a large number of overhangs, or when a or b are large, i.e., the hybridization between the overhangs is strong due to larger number of complementary bases on opposing strands. In addition, to obtain late actuation, i.e., sharp change in P_{closed} at large Mg^{2+} concentrations, e.g., at values higher than the 5 mM typically used for assembling the DNA origami hinges. The expression in Equation 3.18 indicates that the critical Mg^{2+} concentration associated with this sharp increase in P_{closed} is controlled by the parameter g . Specifically, in order to achieve actuation at high Mg^{2+} concentrations, a large value of g is required, i.e., hinges with stiff joints exhibiting a large free energy difference (energy barrier) ΔG_{bh} between the open and closed state of their bare counterparts is required. Thus, the designs of both the hinge joint and the overhangs are critical to achieving sharp and late actuation.

3.7 Acknowledgements

Chapter 2, in full, is a reprint of the material as it appears in ACS Nano 2018, Alexander E. Marras, Ze Shi, Michael Lindell III, Randy A. Patton, Chao-Min Huang, Lifeng Zhou, Hai-Jun Su, Gaurav Arya, Carlos E. Castro. The dissertation author was one of the investigators and authors of this paper.

3.8 References

- [1] J. Bath and A. J. A. J. Turberfield, “DNA Nanomachines,” *Nat. Nanotechnol.*, vol. 2, no. Box 1, p. 275, 2007.
- [2] H. Gu, W. Yang, and N. C. Seeman, “DNA Scissors Device Used to Measure Muts Binding to DNA Mis-Pairs,” *J. Am. Chem. Soc.*, vol. 132, p. 4352, mar 2010.
- [3] T. Omabegho, R. Sha, and N. C. Seeman, “A Bipedal DNA Brownian Motor with Coordinated Legs,” *Science (80-.)*, vol. 324, pp. 67–71, apr 2009.
- [4] J. Pan, F. Li, T.-G. Cha, H. Chen, and J. H. Choi, “Recent progress on DNA based walkers,” *Curr. Opin. Biotechnol.*, vol. 34, pp. 56–64, aug 2015.
- [5] Y. Krishnan and F. C. Simmel, “Nucleic Acid Based Molecular Devices,” *Angew. Chem., Int. Ed.*, vol. 50, no. 14, p. 3124, 2011.
- [6] S. Modi, S. M. G., D. Goswami, G. D. Gupta, S. Mayor, Y. Krishnan, S. MG, D. Goswami, G. D. Gupta, S. Mayor, and Y. Krishnan, “A DNA Nanomachine That Maps Spatial and Temporal Ph Changes inside Living Cells,” *Nat. Nanotechnol.*, vol. 4, p. 325, may 2009.
- [7] B. Yurke, A. J. Turberfield, A. P. Mills, F. C. Simmel, and J. L. Neumann, “A DNA-fuelled molecular machine made of DNA,” *Nature*, vol. 406, pp. 605–608, aug 2000.
- [8] H. Yan, X. Zhang, Z. Shen, and N. C. Seeman, “A robust DNA mechanical device controlled by hybridization topology,” *Nature*, vol. 415, pp. 62–65, jan 2002.
- [9] F. A. Aldaye and H. F. Sleiman, “Modular Access to Structurally Switchable 3D Discrete DNA Assemblies,” *J. Am. Chem. Soc.*, vol. 129, p. 13376, 2007.
- [10] C. E. Castro, H.-J. J. Su, A. E. Marras, L. Zhou, and J. Johnson, “Mechanical design of DNA nanostructures,” *Nanoscale*, vol. 7, pp. 5913–21, apr 2015.
- [11] S. Dhakal, M. R. Adendorff, M. Liu, H. Yan, M. Bathe, and N. G. Walter, “Rational design of DNA-actuated enzyme nanoreactors guided by single molecule analysis,” *Nanoscale*, vol. 8, pp. 3125–3137, jan 2016.
- [12] J. J. Funke and H. Dietz, “Placing Molecules with Bohr Radius Resolution Using DNA Origami,” *Nat. Nanotechnol.*, vol. 11, p. 47, 2016.
- [13] T. Gerling, K. F. Wagenbauer, A. M. Neuner, and H. Dietz, “Dynamic DNA devices and assemblies formed by shape-complementary, non-base pairing 3D components,” *Science (80-.)*, vol. 347, pp. 1446–1452, mar 2015.
- [14] H. Gu, J. Chao, S. J. Xiao, and N. C. Seeman, “A Proximity-Based Programmable DNA Nanoscale Assembly Line,” *Nature*, vol. 465, p. 202, 2010.

- [15] P. Ketterer, E. M. Willner, and H. Dietz, “Nanoscale rotary apparatus formed from tight-fitting 3D DNA components,” *Sci. Adv.*, vol. 2, no. 2, pp. e1501209–e1501209, 2016.
- [16] A. Kuzuya, Y. Sakai, T. Yamazaki, Y. Xu, and M. Komiyama, “Nanomechanical DNA origami ‘single-molecule beacons’ directly imaged by atomic force microscopy,” *Nat. Commun.*, vol. 2, p. 449, sep 2011.
- [17] A. Kuzyk, R. Schreiber, H. Zhang, A. O. Govorov, T. Liedl, and N. Liu, “Reconfigurable 3D Plasmonic Metamolecules,” *Nat. Mater.*, vol. 13, no. July, p. 862, 2014.
- [18] J. List, E. Falgenhauer, E. Kopperger, G. Pardatscher, and F. C. Simmel, “Long-range movement of large mechanically interlocked DNA nanostructures,” *Nat. Commun.*, vol. 7, p. 12414, 2016.
- [19] A. E. Marras, L. Zhou, V. Koliopoulos, H. J. Su, and C. E. Castro, “Directing folding pathways for multi-component DNA origami nanostructures with complex topology,” *New J. Phys.*, vol. 18, no. 5, p. 55005, 2016.
- [20] A. E. Marras, L. Zhou, H.-J. Su, and C. E. Castro, “Programmable motion of DNA origami mechanisms,” *Proc. Natl. Acad. Sci. U. S. A.*, vol. 112, no. 3, pp. 713–718, 2015.
- [21] D. Mathur and E. R. Henderson, “Programmable DNA Nanosystem for Molecular Interrogation,” *Sci. Rep.*, vol. 6, pp. 1–9, 2016.
- [22] L. Zhou, A. E. Marras, H. J. Su, and C. E. Castro, “DNA origami compliant nanostructures with tunable mechanical properties,” *ACS Nano*, vol. 8, no. 1, pp. 27–34, 2014.
- [23] Z. Shi, C. E. Castro, and G. Arya, “Conformational Dynamics of Mechanically Compliant DNA Nanostructures from Coarse-Grained Molecular Dynamics Simulations,” *ACS Nano*, vol. 11, no. 5, pp. 4617–4630, 2017.
- [24] L. Zhou, A. E. Marras, H. J. Su, and C. E. Castro, “Direct design of an energy landscape with bistable DNA origami mechanisms,” *Nano Lett.*, vol. 15, no. 3, pp. 1815–1821, 2015.
- [25] Y. Ke, T. Meyer, W. M. Shih, and G. Bellot, “Regulation at a distance of biomolecular interactions using a DNA origami nanoactuator,” *Nat. Commun.*, vol. 7, p. 10935, 2016.
- [26] R. M. Zadegan, M. D. E. Jepsen, K. E. Thomsen, A. H. Okholm, D. H. Schaffert, E. S. Andersen, V. Birkedal, and J. Kjems, “Construction of a 4 zeptoliters switchable 3D DNA box origami,” *ACS Nano*, vol. 6, no. 11, pp. 10050–10053, 2012.
- [27] S. M. Douglas, I. Bachelet, and G. M. Church, “A Logic-Gated Nanorobot for Targeted Transport of Molecular Payloads,” *Science (80-.)*, vol. 335, p. 831, feb 2012.
- [28] S. Ranallo, C. Prevost-Tremblay, A. Idili, A. Vallee-Belisle, and F. Ricci, “Antibody-Powered Nucleic Acid Release Using a DNA-Based Nanomachine,” *Nat. Commun.*, vol. 8, p. 15150, 2017.

- [29] G. J. Lavella, A. D. Jadhav, and M. M. Maharbiz, "A Synthetic Chemomechanical Machine Driven by Ligand-Receptor Bonding," *Nano Lett.*, vol. 12, p. 4983, 2012.
- [30] H. K. Walter, J. Bauer, J. Steinmeyer, A. Kuzuya, C. M. Niemeyer, and H. A. Wagenknecht, "DNA Origami Traffic Lights with a Split Aptamer Sensor for a Bicolor Fluorescence Readout," *Nano Lett.*, vol. 17, p. 2467, 2017.
- [31] Z. Liu, C. Tian, J. Yu, Y. Li, W. Jiang, and C. Mao, "Self-Assembly of Responsive Multilayered DNA Nanocages," *J. Am. Chem. Soc.*, vol. 137, p. 1730, 2015.
- [32] D. Yang, A. Ward, K. Halvorsen, and W. P. Wong, "Multiplexed Single-Molecule Force Spectroscopy Using a Centrifuge," *Nat. Commun.*, vol. 7, p. 11026, 2016.
- [33] W. Bae, K. Kim, D. Min, J. K. Ryu, C. Hyeon, and T. Y. Yoon, "Programmed Folding of DNA Origami Structures through Single-Molecule Force Control," *Nat. Commun.*, vol. 5, p. 5654, 2014.
- [34] K. C. Neuman and A. Nagy, "Single-Molecule Force Spectroscopy: Optical Tweezers, Magnetic Tweezers and Atomic Force Microscopy," *Nat. Methods*, vol. 5, p. 491, 2008.
- [35] M. Iwaki, S. F. Wickham, K. Ikezaki, T. Yanagida, and W. M. Shih, "A Programmable DNA Origami Nanospring That Reveals Force-Induced Adjacent Binding of Myosin Vi Heads," *Nat. Commun.*, vol. 7, p. 13715, 2016.
- [36] L. H. Li, X. J. Tian, Z. L. Dong, L. Q. Liu, O. Tabata, and W. J. Li, "Manipulation of DNA Origami Nanotubes in Liquid Using Programmable Tapping-Mode Atomic Force Microscopy," *Micro Nano Lett.*, vol. 8, p. 641, 2013.
- [37] M. Siavashpouri, C. H. Wachauf, M. J. Zakhary, F. Praetorius, H. Dietz, and Z. Dogic, "Molecular Engineering of Chiral Colloidal Liquid Crystals Using DNA Origami," *Nat. Mater.*, vol. 16, p. 849, 2017.
- [38] E. Kopperger, J. List, S. Madhira, F. Rothfischer, D. C. Lamb, and F. C. Simmel, "A Self-Assembled Nanoscale Robotic Arm Controlled by Electric Fields," *Science (80-.)*, vol. 359, p. 296, 2018.
- [39] S. Lauback, K. R. Mattioli, A. E. Marras, M. Armstrong, T. P. Rudibaugh, R. Sooryakumar, and C. E. Castro, "Real-Time Magnetic Actuation of DNA Nanodevices Via Modular Integration with Stiff Micro-Levers," *Nat. Commun.*, vol. 9, p. 1446, 2018.
- [40] Y. Yang, R. Tashiro, Y. Suzuki, T. Emura, K. Hidaka, H. Sugiyama, and M. Endo, "A Photoregulated DNA-Based Rotary System and Direct Observation of Its Rotational Movement," *Chem. - Eur. J.*, vol. 23, p. 3979, 2017.
- [41] A. Kuzyk, Y. Yang, X. Duan, S. Stoll, A. O. Govorov, H. Sugiyama, M. Endo, and N. Liu, "A Light-Driven Three-Dimensional Plasmonic Nanosystem That Translates Molecular Motion into Reversible Chiroptical Function," *Nat. Commun.*, vol. 7, p. 10591, 2016.

- [42] A. Kuzyk, M. J. Urban, A. Idili, F. Ricci, and N. Liu, “Selective Control of Reconfigurable Chiral Plasmonic Metamolecules,” *Sci. Adv.*, vol. 3, p. e1602803, 2017.
- [43] J. SantaLucia, “A Unified View of Polymer, Dumbbell, and Oligonucleotide DNA Nearest-Neighbor Thermodynamics,” *Proc. Natl. Acad. Sci. U. S. A.*, vol. 95, p. 1460, 1998.
- [44] Y. Ke, S. M. Douglas, M. Liu, J. Sharma, A. Cheng, A. Leung, Y. Liu, W. M. Shih, and H. Yan, “Multilayer DNA origami packed on a square lattice,” *J. Am. Chem. Soc.*, vol. 131, pp. 15903–8, nov 2009.
- [45] T. G. Martin and H. Dietz, “Magnesium-Free Self-Assembly of Multi-Layer DNA Objects,” *Nat. Commun.*, vol. 3, p. 1103, 2012.
- [46] S. M. Douglas, A. H. Marblestone, S. Teerapittayanon, A. Vazquez, G. M. Church, and W. M. Shih, “Rapid prototyping of 3D DNA-origami shapes with caDNAno,” *Nucleic Acids Res.*, vol. 37, no. 15, pp. 5001–5006, 2009.
- [47] N. R. Markham and M. Zuker, *Bioinformatics*, vol. 1 of *Methods in Molecular Biology*. Totowa, NJ: Humana Press, 2008.
- [48] N. R. Markham and M. Zuker, “DINAMelt web server for nucleic acid melting prediction,” *Nucleic Acids Res.*, vol. 33, no. SUPPL. 2, pp. 577–581, 2005.

Chapter 4

Free Energy Landscape of Cation-mediated Actuation of Overhang-modified DNA origami Nanostructures

4.1 Abstract

Achieving rapid, noninvasive actuation of DNA structures is critical to expanding the functionality of DNA nanotechnology. A promising approach for actuation involves introducing multiple, weakly-complementary pairs of single-stranded DNA overhangs to components of the structure, and triggering hybridization-dissociation of the overhangs via changes in solution ionic conditions to drive large-scale structural transitions. Here we provide the molecular underpinnings of this new approach in terms of free energy landscapes obtained via simulations for the example of a DNA origami hinge whose arms are actuated between open and closed states. A novel free-energy decomposition strategy is devised to enable these calculations while retaining accurate

descriptions of global hinge motions and local base-pairing events. Our results reveal that compared to free overhangs that do not hybridize, those attached to hinge arms exhibit a sharp free energy minimum at small hinge angles separated by an energy barrier at intermediate angles. The depth of the minimum and the height and width of the barrier are found to vary with ion concentration and the length, sequence, and attachment position of the overhangs. We show how these landscape features and trends arise from the interplay between the hybridized and dissociated states of the overhangs whose stabilities depend on ion screening effects and angular confinement effects imposed by the arms. The overall free energy, including contributions from the bare hinge and all overhangs, reveals a sharp minimum in the closed state with a broad energy barrier separating the open and closed states. We discuss how hinge actuation efficiency and rates, related to these two features of the landscape, can be tuned by modulating the design and location of the overhangs. The mechanistic understandings and design rules revealed here should be applicable to many other systems involving DNA strand hybridization in confined media.

4.2 Introduction

Rapid advancements in DNA nanotechnology over the past decade have enabled the fabrication of structures with controllable motions (1; 2; 3; 4; 5; 6), an important step to creating the next generation of dynamic DNA nanodevices. One strategy for actuating DNA structures involves the binding of external biomolecules to reconfigure DNA devices (7; 8; 9). A popular method here is the toehold-mediated strand displacement method, where one strand of an existing DNA duplex is displaced by a longer, externally provided strand that can form a more stable duplex (10). In this manner, hybridized connections between device components may be released, or reestablished to enable reversible actuation. This method offers the benefits of sequence specificity of displacement strands and ease of introducing displacement sites within devices. However, due to the need for external strands, release of waste strands, and slow kinetics of the

displacement reaction, the method can be invasive and slow. Another actuation strategy involves integrating stimuli-responsive molecular entities into the devices, which also makes the actuation less invasive and more responsive to environmental stimuli. These entities include base-stacking motifs, DNA triplexes, azobenzene moieties, and I-motifs that respond to environmental cues like light, temperature, pH, and ions to establish or disrupt interactions between device components (11; 12; 13; 14; 15). A third strategy involves external forces to reconfigure devices. These forces may be applied via electrical or magnetic fields (16; 17), via depletants (18), or via optical traps and atomic force microscope tips (19; 20). As these forces are applied directly to the structures and can be modulated fairly rapidly with existing capabilities, these methods can achieve rapid actuation response times, albeit with advanced fabrication and instrumentation requirements.

Recently, Marras et al.(21) proposed a promising actuation method that combines the non-invasiveness of environmental triggers with the specificity of DNA hybridization to enable rapid reconfiguration of devices with response times comparable to force-based methods. The approach involves introducing multiple, weakly complementary pairs of single-stranded DNA overhangs to the device components to be actuated, and using changes in solution cation concentration to trigger rapid hybridization or dehybridization of the overhangs to drive conformational transitions in the device. Because this method involves collective hybridization of many short strands, and also does not involve any diffusion of strands or displacement of one hybridized strand with another, it exhibits much faster response times compared to the strand-displacement method. As demonstration, the approach was applied to a DNA origami hinge that nominally exhibits open conformations with its arms subtending large angles about the vertex (**Fig. 4.1**). By introducing short, complementary overhangs to the inner surfaces of the two hinge arms, the modified hinges could be efficiently actuated between conformations with open and closed arms using a variety of cations, including mono-, di- and trivalent ions. The actuation responses (fraction of hinges exhibiting closed arms vs. cation concentration) were characterized as a function of various design parameters, such as the number and length of overhangs and the bending stiffness of the hinge

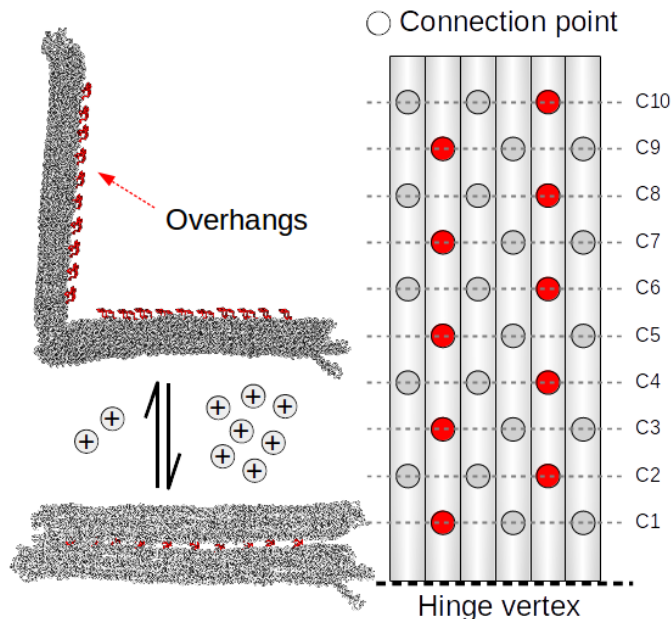


Figure 4.1: DNA origami hinge design. Single-stranded DNA overhangs are attached on the hinge arms at connection points with 10 different distances from the vertex. There are 30 connection points in all on the hinge arm, and the connection points used for 10-connection design is colored in red. When the ion concentration changes, the hinge will be reversibly actuated to closed states.

joint. The results revealed strong, intriguing variations with respect to the design parameters, suggesting high tunability of the actuation responses.

Based on our current understanding, the actuation mechanism may be explained as a competition between (1) the intrinsic predisposition of the “bare” device (minus overhangs) to exhibit open conformations, and (2) the hybridization of overhangs that favors closed conformations. The former effect stems from the underlying structural design of the bare device which dictates intra- and intermolecular interactions between components, and hence their preferred conformations. For instance, in DNA hinges, the open conformation appears to arise from the mechanics of the DNA joint connecting the hinge arms, and not from electrostatic repulsion between them, given that the bare hinges exhibited similar hinge-angle distributions across a wide range of cation concentrations. The latter effect provides the driving force necessary for the device to overcome its natural propensity for open conformations and transition to a closed

conformation. Importantly, the strength of this driving force depends on cation concentration. At low ion concentrations, the overhangs prefer to remain unhybridized, and the device retains the open conformation it exhibits without overhangs. As ion concentration is raised, the hybridized state of the overhangs becomes increasingly stabilized, causing an increasingly larger fraction of structures to exhibit closed conformations. In the original study (21), we expressed both these effects in thermodynamic terms, the former in terms of a free energy difference ΔG_{bare} between the open and closed states, and the latter in terms of a hybridization free energy $\Delta G_{\text{hyb}}(c)$ that depends on ion concentration c . Assuming that all overhang pairs are indistinguishable, we formulated a simple, two-state thermodynamic model for the probability of observing closed hinges as a function of ion concentration and the two free energies. Since the hybridization free energy of the tethered, confined overhangs must be distinct from that of free strands in solution, we cast $\Delta G_{\text{hyb}}(c)$ as an additive correction ΔG_{corr} to the *solution*-state hybridization free energy obtained from secondary-structure prediction algorithms. Using the unknowns ΔG_{bare} and ΔG_{corr} as fitting parameters, we were able to obtain good agreement with the experimentally measured actuation responses. While this description was useful for establishing the importance of bare-device mechanics and overhang hybridization in actuation and for fitting experimental data, our knowledge of the actuation mechanism remains very qualitative. For instance, the free energies contributed by the device and the overhangs, and how they vary with the reaction coordinate and ion concentration to “tilt” the overall free energy towards the open or closed conformation remain unknown. How these free energies change with the various design parameters and the associated molecular mechanisms also are not known. Elucidating such energetics and molecular mechanisms would be crucial to facilitate future design and optimization of actuation devices and responses.

Here we provide such a molecular and energetic foundation for this actuation method through calculation of free energy landscapes via molecular-scale simulations, using the DNA hinge as our model system. Ideally, all-atom simulations should provide the most accurate de-

scription of the hinges. However, due to the large system size and slow timescales of hybridization and dissociation, such simulations would require prohibitive computational costs. To this end, we use the coarse-grained model, *oxDNA* (22; 23), to represent the hinges. *oxDNA* now been applied to a variety of structures, (24; 25; 26; 27; 28; 22; 29; 30) and shown to yield accurate descriptions of their mechanics, conformational dynamics, ion-dependent hybridization thermodynamics, suggesting that this model should provide reasonable predictions for the ion-actuated DNA hinges studied here. To further alleviate computational costs, we use a novel strategy that involves splitting the system into bare hinge, a large structure with short relaxation time, and overhangs, a small system with long relaxation time, and computing their free energies separately using efficient simulation approaches. In this manner, we were able to obtain not only the overall free energy landscape of the overhang-modified DNA hinges as a function of its conformation (hinge angle), but also the free energy contributions arising from the hinge joint and each of the overhang pairs. By computing such energy landscapes for a range of ionic conditions and overhang design parameters, analyzing the conformations of the overhangs, and relating features of the energy landscape to actuation responses and rates, we were able to provide a quantitative, molecular-level understanding of the actuation mechanism that could be used as “design rules” for achieving and optimizing actuation responses. The results obtained here would be important not only for hinge actuation, but many other systems involving DNA hybridization in confined media, including DNA microarrays, DNA-tethered nanoparticles (31), and assembly of DNA origami tiles.

4.3 Results and discussion

Computational Strategy

In simulations, even with coarse-grained models, exploring long time scale processes such as the DNA hybridization and dissociation is still challenging. To address this computational challenge, we split the system into two parts: the DNA hinge without overhangs, or the bare hinge,

and the overhangs on the hinge arms (Figure 4.2). For the bare hinge, the rotational relaxation time of the hinge arms is much shorter than the hybridization and dissociation of overhangs (Figure S1), which makes the simulation less computational demanding. For the overhangs, the system size is significantly reduced, enabling adequate sampling of all the hybridization states. As the distance between adjacent overhang connection points is large, therefore we could keep the same assumption we proposed in our previous work that each overhang interacts only with its complementary counterpart on the opposite arm. In this way, the total free energy of the system can then be calculated as $G_{tot}(\theta) = G_{bh}(\theta) + G_{oh}(\theta)$, where G_{tot} , G_{bh} , and G_{oh} are the free energies of the system, bare hinge, and overhang pairs, respectively. Hinge angle θ is defined as the angle between two hinge arms.

The free energy landscape of the bare hinge G_{bh} was obtained through umbrella sampling MD simulations. Ideally, the order parameter of umbrella sampling should be the hinge angle θ . While the hinge angle in simulations is calculated as the angle between the two fitted axes of the two hinge arms, applying restraints on this order parameter become tedious as it involves derivative of the fitting equation in calculating the restraint force. To simplify this problem, umbrella sampling were performed with respect to the distance between the two arms' center of mass given that this distance exhibits a correlation with hinge angle (Figure 4.12).

In the simulations of the overhangs, the bare hinge was substituted with repulsion planes to mimic the steric constraint imposed by the hinge arms, and the angle between the repulsion planes was considered as the hinge angle, as shown in Figure 4.2. Since all the overhangs are identical except for the location of the overhangs, the total free energy of the overhangs was calculated as the sum of free energy of individual pairs of overhangs located at different positions: $G_{oh} = \sum_{i=1}^n G_{oh,i}(\theta)$. Because of the double helical structure of B-DNA, the overhangs can only be positioned at specific connection points, where the distance between adjacent connection points of overhangs on each side is the multiple of 10.6 nm, the length of 16 base pairs, or 1.5 turns in square lattice DNA origami.

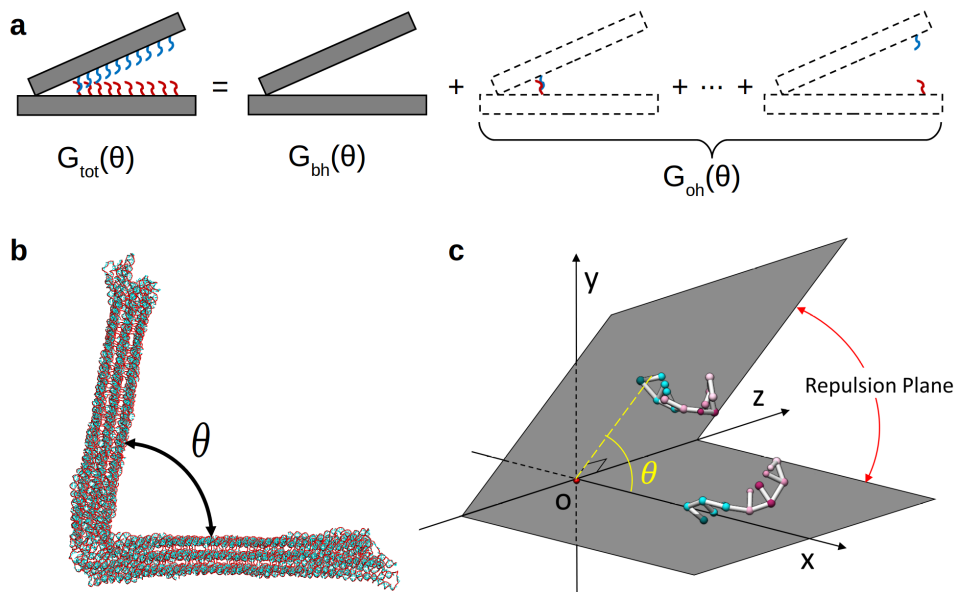


Figure 4.2: Computational strategy for efficiently computing hinge actuation free energies. **a:** hinge can be divided into two parts: the bare hinge and the overhangs. The total free energy G_{tot} can be written as the sum of the free energy of bare hinge (G_{bh}) and overhangs (G_{oh}). **b** and **c:** The free energy landscape of the bare hinge is calculated with MD simulation, while the free energy landscape of the overhangs is calculated with VMMC simulations.

To simplify the problem, one of the repulsion plane, was set up as the x - z plane, and the other only rotated about the y axis to ensure that the overhangs were always connected to the plane while sampling strand conformations during the simulations. Therefore, the hinge angle could be calculated as the projected angle onto x - y plane between the two ends of the overhangs, which are designed to be connected to the hinge, and the origin point, as shown in Figure 4.2. Stiffer springs are used to confine the movement of the overhang into the hinge's movement To investigate how the overhangs “close” the hinge with increasing ionic strength, simulations under different ion concentrations were performed to examine how the free energy landscape of the system is modulated by ionic conditions. Since oxDNA is only parameterized with Na^+ ions, simulations under ion concentrations of 0.2M, 0.4M, and 1.2M Na^+ were performed to study how the ion concentration affect the free energy landscape of the hinge.

During the simulations, the free energy difference between different hybridization states

causes severe sampling issues. Therefore, sampling of the hybridization states was enhanced through a bias on the transition probability in virtual move Monte Carlo (VMMC) simulations. After recovering the 2D free energy landscape with weighted histogram analysis method, the free energy landscape along the hinge angle could be constructed by combining the states with the same hinge angle but with different numbers of base pairs formed after a modified 2D weighted histogram analysis method. Most of our simulations were performed with 7-base long overhangs (surface-TTTCGAC-5' and 3'-GTCGTTT-surface) with only the terminal four bases contributing to hybridization across two hinge arms.

Free energy landscape of the overhangs

The free energy landscape for a representative pair of overhangs with 4 complementary bases at the first connection point is plotted in Figure 4.3. What is shown as background in the same graph is the 2D free energy landscape of the overhangs plotted with respect to the number of base pairs formed together with the hinge angle. The collapsed free energy landscape with respect to the hinge angle is calculated from the sum of probability of all the states with different hybridization states, or different number of base pairs formed, in the same hinge angle bin. The free energy landscape (black curve in Figure 4.3) displays a large barrier in between the plateau at large hinge angle and the deep free energy minimum at short angles. At large hinge angles, the overhangs are unable to associate, but as the hinge angle decreases, the strands begin to form unstable base pairs (e.g., at 41° angle), which seems to correlate with an increase in the free energy. At the barrier, which we believe is due to confinement from the hinge arm, there appears to be a more or less equal probability of observing hybridized and dissociated overhangs. As the hinge angle is further decreased, the hybridized state becomes prevalent and is maximized at the minimum. Thereafter, the hinge angle becomes severely constricted and the free energy shoots up. These results show a clear transition in dominant states from hybridized to dissociated states.

The free energy landscape of overhangs at different connection points and under different

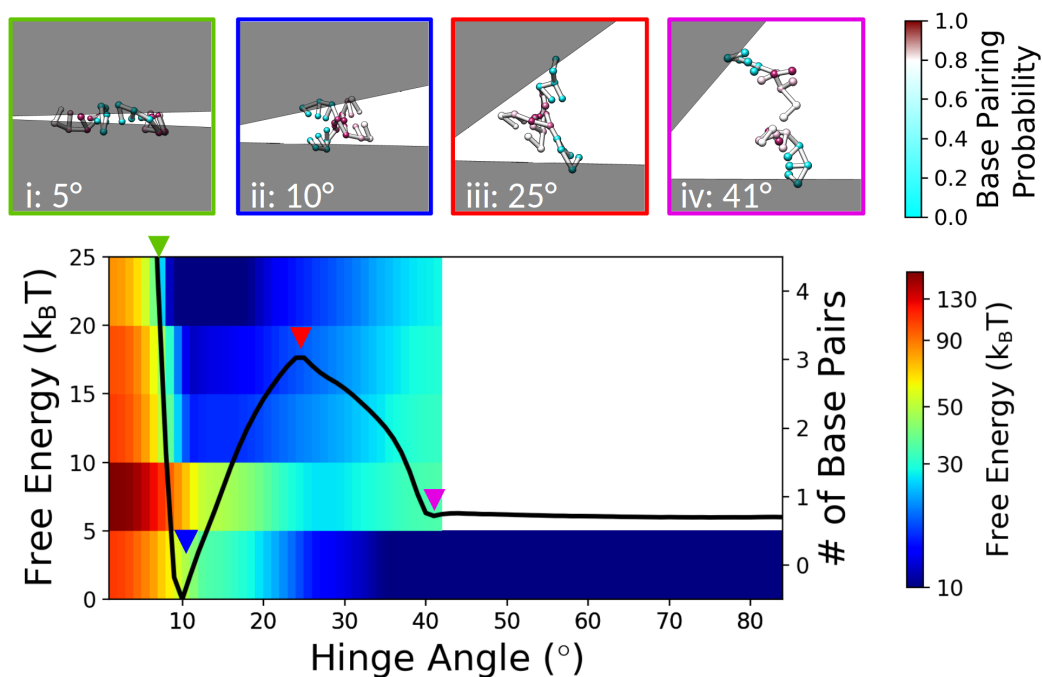


Figure 4.3: Representative free energy landscape of a single overhang pair. The energy landscape is plotted with respect to the hinge angle and the background is the energy landscape of different hybridization states for the first connection of strand with 4 complementary bases at 0.2 M Na^+ . Representative snapshots of the overhang conformations at different points along the energy landscape are from the simulation of the window is attached, which shows how the overhangs transition changes from extremely confined to fully hybridized then to dissociated states and non-interaction states. All nucleotides are colored according to the percentage of hybridized states in each biased simulation run.

ion concentrations are shown in Figure 4.4 and Figure 4.14. It can be observed that the free energy landscapes are quite different between overhangs at different connection points (Figure 4.4a) and the effect of ion concentration change on free energy landscape of overhangs is also different for overhangs at different connection points, as shown in Figure 4.4c-f. The free energy gain for the first to the third connection point is barely affected by the ion concentration change (Figure 4.4c,d), while the landscape of those at the fourth connection point or farther away from the hinge vertex will have more free energy gain at small hinge angle under higher ion concentrations (Figure 4.4e,f). When plotted with respect to the distance between connection points, or the end-to-end distance, as shown in Figure 4.4b, the width and height of the barrier

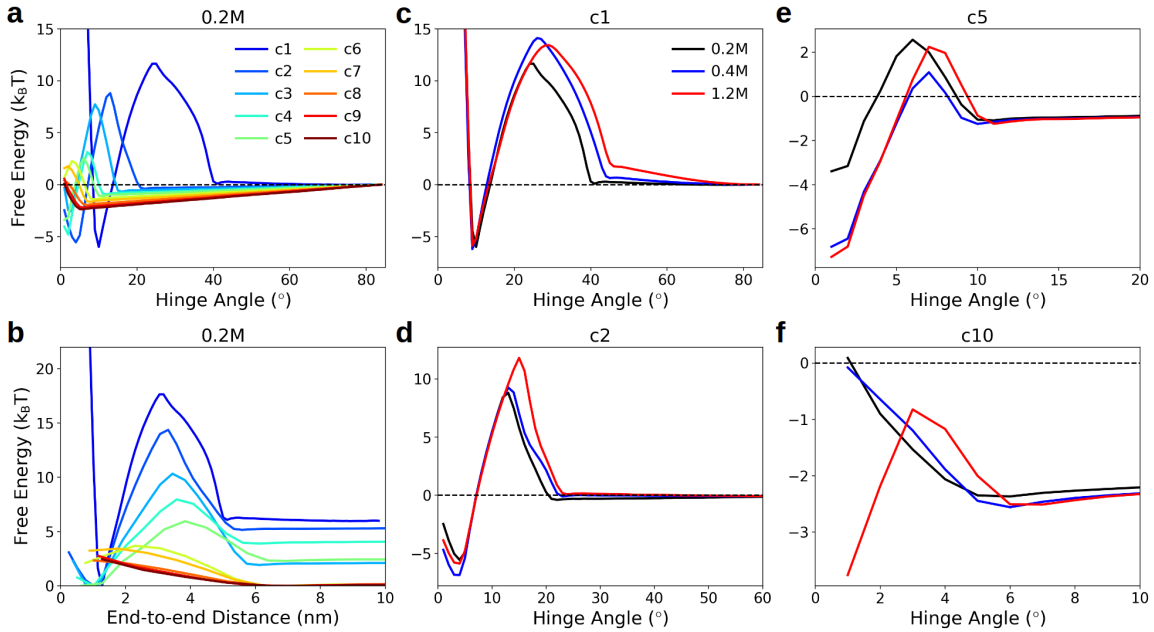


Figure 4.4: Total free energy landscape of overhang strands with 4 complementary bases. Free energy landscapes of overhangs at 10 different connection points under 0.2M ion concentration are plotted with respect to hinge angle (a) and with respect to end-to-end distance (b). The free energy landscape of overhangs at 1st, 2nd, 5th, and 10th connection points under different ion concentrations are plotted in c-f

between the plateau and free energy minimum will also change at different connection points. If the overhangs is farther away from the hinge vertex, the barrier will be lower and wider.

Ion concentration effects and origin of barrier

To elucidate the origin of the barrier and how the ion concentration affect the free energy landscape, the ensemble of overhangs was decomposed into two sub-ensembles: the hybridized base pairs (G_{hyb}) states and fully dissociated strands (no base pairs; G_{dis}), where only the hybridized ensemble free energy is expected to be affected by the ion concentration change. The free energy of the two sub-ensembles are plotted separately in Figure 4.5 together with the free energy of the overall ensemble as given by $G_{\text{tot}} = -k_B T \ln[\exp(-G_{\text{hyb}}/k_B T) + \exp(-G_{\text{dis}}/k_B T)]$. To explain the above effects, we pick two extreme locations in the nanodevice design: the first

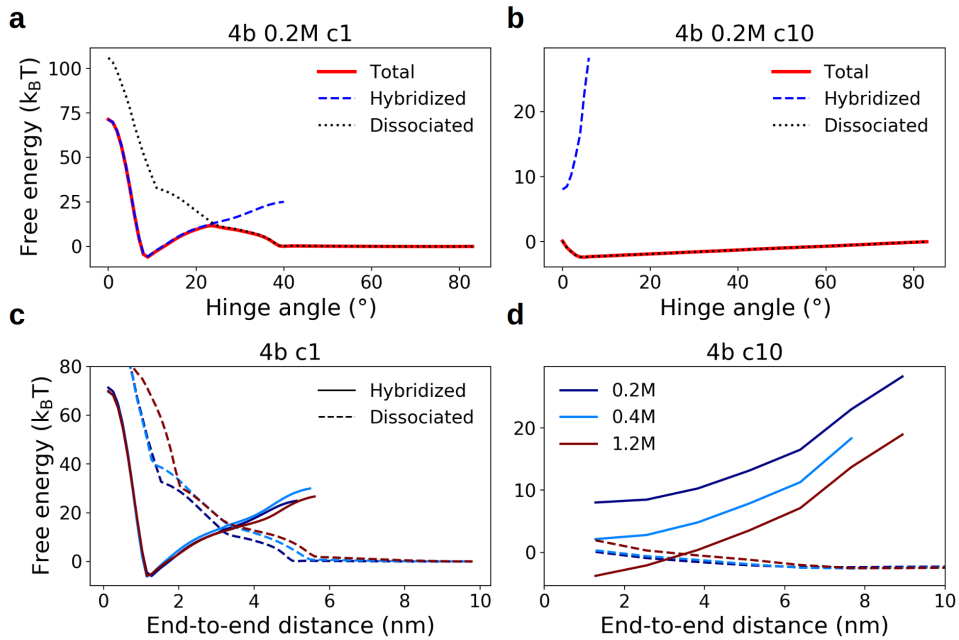


Figure 4.5: The effect of ion concentration change on free energy landscape of overhangs. **a** and **b** are the free energy landscape of overhangs with 4 complementary bases at the first and the 10th connection point under 0.2 M sodium ions, respectively. **c** and **d** are how the hybridized and dissociated components of the free energy landscape at the first and the 10th connection point under different ion concentrations.

(Figure 4.5a and c) and the tenth (Figure 4.5b and d) connection points, the closest and the farthest from the hinge vertex.

In Figure 4.5a, according to the free energy contributions, the free energy landscapes of overhangs near the vertex can be split into two regions: one before the peak, where the hybridized states dominate, and one after the peak, where the dissociated states dominate. The free energy of the dissociated sub-ensemble increases with decreasing hinge angle because of the increasing electrostatic repulsion interaction between overhangs and more entropy loss under stronger confinement. The increasing trend in total free energy will stop and reach the peak of the free energy barrier when the two overhang strands begin to form base pairs and fall into the condition that the hybridized states dominate. Further decreasing hinge angle will result in smaller distance between overhangs and larger chance to form base pairs. However, when the

hinge angle is too small, the confinement becomes too severe, and even the hybridized states are not favored.

Therefore, together with the critical conformations shown in Figure 4.3 at minimums and maximums of the free energy landscape, we can further divide the free energy landscape into four regions: 1) *Steric repulsion* interaction region: (from conformation (i) to conformation (ii), where the space for overhangs is limited for duplex DNA strand, so the repulsion interaction between overhangs is strong. 2) *Fully hybridized* region (from conformation (ii) to conformation (iii)), where there are enough space for duplex DNA and the end-to-end distance is small. Hybridized states are more favorable. 3) *Dissociation* region (from conformation (iii) to conformation (iv)), where the end-to-end distance becomes a bit larger for the strands to stay in hybridized states. As a result, the dissociated states dominate, but the two strands still collide in a relative smaller space, resulting in higher electrostatic repulsion energy and lower entropy as compared to the non-interaction states. 4) *Non-interaction* region (from conformation (iv) to large hinge angle), where the end-to-end distance is so large that the two strands will not interact with each other, thus the free energy plot only results from the entropy force exerted on the hinge.

For overhangs at different connection points, when the overhangs are far away from the vertex (Figure 4.5b), even small hinge angles result in a large end-to-end distance between the two overhangs, leading to their hybridized states being less favored as compared to those in the overhangs near the vertex at the same hinge angle. In this way, the connections away from the vertex will reach the critical angle between the hybridized states dominant and dissociated states dominant region at smaller hinge angle, decreasing the ion concentration may shift the hybridized state dominant region to extremely small hinge angle. As a result, under ion concentration of 0.2M, we find that the hybridization dominant region vanishes as the whole region falls out of the sampling region (greater than 1°), which does not occur for the first connection (Figure 4.5c).

When increasing the ion concentration, the free energy gain for each base pair is larger in Figure 4.5d, therefore the hybridized states become dominant at larger hinge angle compared to the

overhangs under lower ion concentrations. However, for small angles with severe confinements, both the hybridized and dissociated states exhibit very high free energies because of the strong steric repulsion (due to the excluded volume effect) from the hinge arm confinement, therefore perturbations caused by variations in the ion concentrations are almost negligible in comparison, as shown in Figure 4.5c.

Hinge confinement effect on barrier shape

From the difference between free energy landscapes in Figure 4.5c and Figure 4.5d, we could see that the hinge confinement would greatly affect the shape of the free energy landscape apart from the end-to-end distance of the overhang pairs. To further elucidate how the steric constraint imposed by the hinge arms modify the free energy landscape of the overhangs, we also studied the free energy landscapes of overhang pairs under different confinements. Here we plot the free energy landscapes for two more systems: two free overhangs in solution without confinement (black plot in Figure 4.6a) and two overhangs confined to the hinge arms' movement (red plot in Figure 4.6a). Since the concept of the hinge angle is not present for two free strands in solution, all the free energy landscapes are plotted with respect to the end-to-end distance.

From the free energy profile in Figure 4.6a, we find that similar to the free energy landscape of single overhang pair attached to the hinge arms, there is no interaction between two strands at large end-to-end distance (greater than 7 nm). When the end-to-end distance decreases, the space that each overhang strand can explore begin to overlap, therefore the two overhangs will collide with each other, as shown in Figure 4.6b and c. For free strands in solution and the overhangs confined to the hinge arm's movement, the interaction between overhangs at dissociated states is the same. When the end-to-end distance further decreases, the overlap between the space that the two overhangs can explore will be large enough for overhang strand to form base pairs, especially at large hinge angles, e.g., compare Figure 4.6c versus Figure 4.6d.

When the repulsion plane is added to the system, the probability of observing a base at

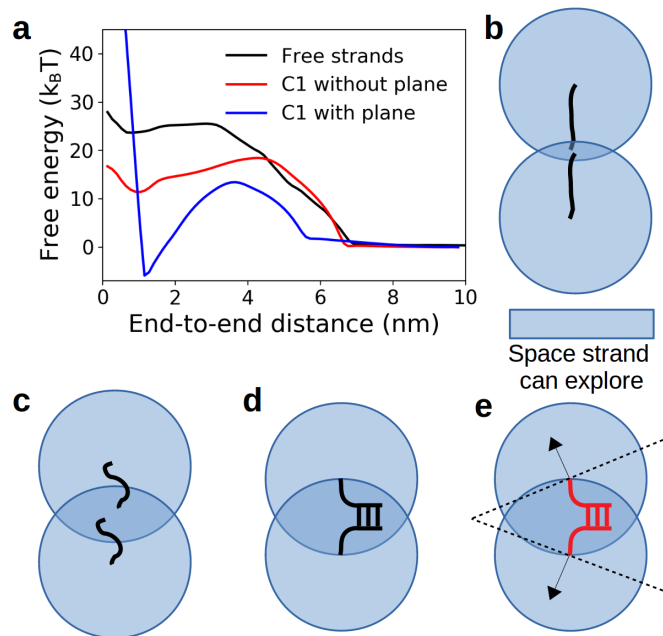


Figure 4.6: The free energy landscape of a single pair of overhangs under different levels of confinements. **a:** Free energy landscape of free strands in solutions, restricted to the hinge movements, and attached to repulsion planes. **b-e:** schematic diagram of overhangs at the first connection point free in solution (**b-d**) and confined to hinge movement (**e**)

certain position (Figure 4.7a and b) indicates that repulsion interaction of the repulsion plane will leave two unfavorable regions near the repulsion plane. Compared to the system without repulsion plane, the overlap between overhangs will be different when the unfavorable regions are involved. As shown in the probability of interaction plotted Figure 4.7c-k, when the end-to-end distance is around 5.76, the overlap will visit the region with higher probability of observing a base for overhangs confined by a repulsion plane (Figure 4.7d, g, and j). When the hinge end-to-end distance further decreases, the probability of interaction and entropy loss will increase significantly and the free energy will shoot up at a relative smaller end-to-end distance compared to the , which is also observed in Figure 4.6a. The sudden increase at smaller end-to-end distance is related to the unfavorable region caused by the repulsion plane confinement, therefore if the hinge angle is small when the space that overhang strand can explore begin to overlap, the normal region will begin to overlap first (as shown in Figure 4.7e, h, and k) so that the free energy

increase will start at larger distance (Figure 4.6). Finally, the starting distance will fall into the same end-to-end distance as free overhang strands when the angle between repulsion planes goes to 0° . In this way, overhangs away from the hinge vertex will have shallower free energy increase in the dissociation region of the the free energy landscape, since the overall entropy loss for the system is almost the same when comparing Figure 4.7f, h and i, k, but two overhangs begin to interact rigorously at larger end-to-end distance compared to the overhangs near the vertex. When it comes to the shape of free energy landscapes, the unfavorable region will result in a wider energy barrier for overhangs away from the overhangs, which is also observed in Figure 4.4. Here we call it the repulsion plane effect on the barrier shape.

When the end-to-end distance is further decreased, the overhang strands will prefer to stay in hybridized states. Since the overhang strand is relatively short, the hybridization energy gain is not large enough to overcome the entropy loss for free strands in solutions and strands confined to hinge's movement, the overhang strands will always prefer to stay in dissociated states that with large hinge angle. However, at smaller end-to-end distance, when the strands prefer to hybridize, the DNA duplex is only stretch at the tangential direction of the trajectory circle (arrow in Figure 4.6e). Compared to the free stretching for free strands in solution (Figure 4.6d), the duplex DNA strands will always be less stretched when confined to the hinge movement, therefore the hybridized states will be more stable. This means that at smaller end-to-end distance, when the hybridized states dominate, the free energy will be lower, which is also observed in Figure 4.6a. As a result, the direction of the stretching force at the end of the overhang strands will affect the free energy gain of the hybridized states, or in other words, the steepness of the left side of free energy barrier, where the hybridized states dominate. The results in Figure 4.4 show the expected result. At the same end-to-end distance, when the hinge angle is larger, or the overhangs is closer to the hinge vertex, the left side of the barrier is steeper and the free energy gain for hybridized states is larger. This is the angular effect of the confinement.

When the repulsion plane is added to the system, the unfavorable region will overlap and

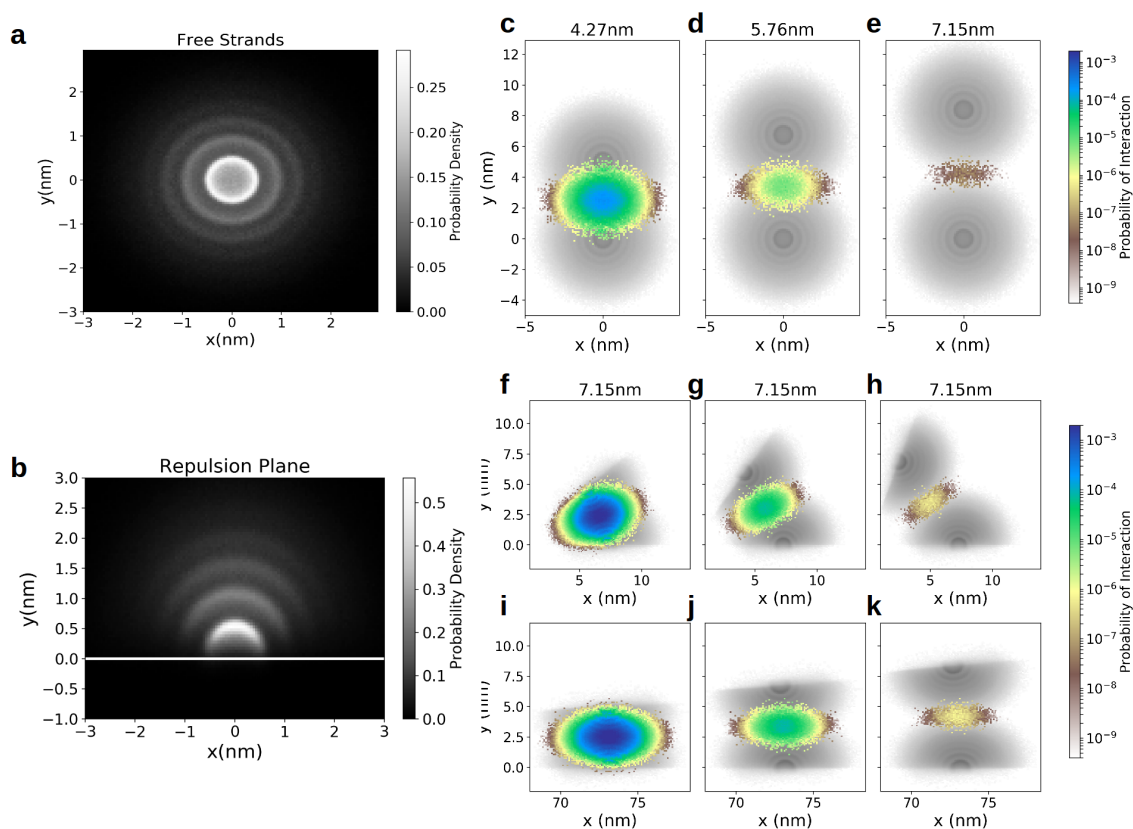


Figure 4.7: The probability of finding a base or interaction between bases. **a-b:** Probability of finding a base at different positions for free strands in solution (**a**) and overhang confined by repulsion plane (**b**). **c-k:** Probability of finding interactions between bases at different end-to-end distance for overhangs free in solution (**c-e**) and confined to hinge movement at the first (**f-h**) and the tenth (**i-k**) connection point.

restrict the strands in pretty limited space. Since the entropy of dissociated states is significantly reduced, the hybridized states will be extremely preferred before the steric repulsion interaction dominates (Figure 4.5c). To which extend the entropy is reduced will determine the final free energy gain of the overhang. Therefore, overhangs away from the vertex will have more space for dissociated states and the free energy gain of hybridized states is smaller.

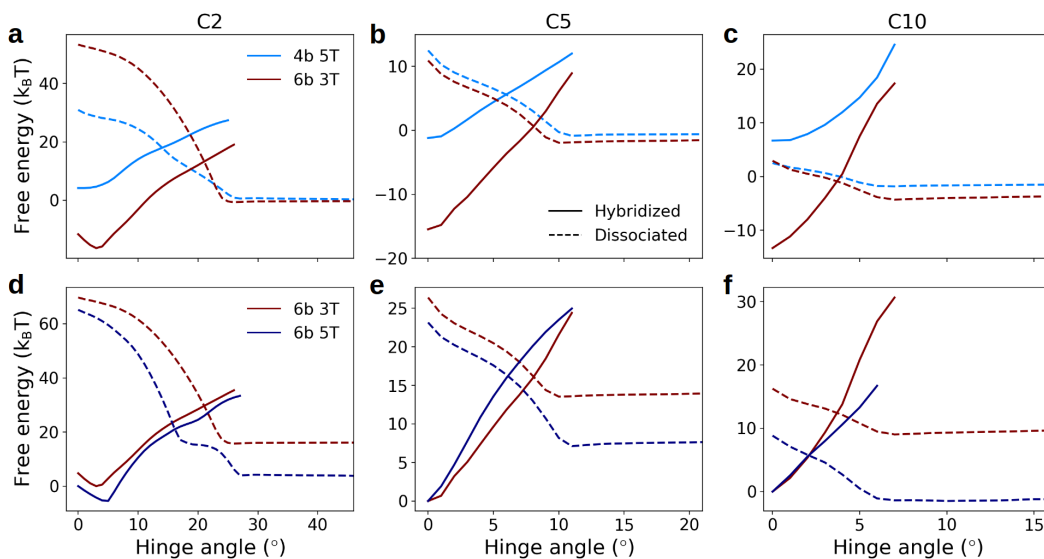


Figure 4.8: The effect of strand length and complementary base number change on free energy landscape of overhangs. The free energy landscape of overhangs at the 2nd (a,b), 5th (c,d), and 10th (e,f) connection point are plotted in two subcomponents for overhangs with 4 or 6 complementary bases and 3T or 5T tails.

4.3.1 Effect of design parameters

From the above results, tuning the repulsion plane effect and the angular effect are two possible approaches to change the free energy landscape. Compared to moving overhangs with the same sequence on the hinge arm, modifying the overhang sequence design may provide more possible changes on the response to the salt-stimuli. To further explore the design of overhangs and gain a deep understanding of the free energy landscape of the overhangs, we carried out additional studies using several different overhang designs. Apart from the overhang design shown above with 4 complementary bases and 3T (TTT) tail bases, we also increased the complementary bases number to 6 or change the tail sequence to 5T (TTTTT).

The free energy landscapes for different strand designs are shown in Figure 4.8 for overhangs at the 2nd, 5th, and 10th connection points. Clearly, the width and free energy difference of the steric repulsion, fully hybridized, dissociation and non-interaction regions changes with different designs. As shown in Figure 4.8a and d, the steric repulsion region varies with the

total strand length. The overhang with 6 complementary bases and 5T tail bases is the longest strand design, so more space is needed for the overhangs. As a result, the steric repulsion is much stronger and the free energy minimum for overhangs will also shift to larger hinge angle. For overhang design with the same number of tail bases but different number of complementary bases (Figure 4.8b and c), overhang designs with more complementary bases will have more free energy gain as the hybridization energy is larger. Therefore, the steepness of the fully hybridized region is also larger. For overhang designs with the same number of complementary bases but with different number of tail bases, the overhangs with longer tail will have larger entropy (Figure 4.8e and f). Therefore the width of the dissociation region will be larger for overhangs with longer tail. The overall free energy gain is determined by both the fully hybridized region and the dissociation region, therefore both the complementary base number and the tail length will affect the final free energy landscape. Long overhangs with short tail will always prefer to stay in hybridized states (6b 3T plots in Figure 4.8), while short overhangs with long tail will always prefer to stay in dissociated states (4b 5T plots in Figure 4.8a-c). Implementing different designs will give rise to different actuation response.

4.3.2 Zip mode and sheer mode

Apart from adding or deleting bases to the overhang sequence, we also investigated the free energy landscape of another binding mode, the “shear” mode. In shear mode, the two strands form a double helix that is perpendicular to the repulsion plane, rather than parallel as in the “zip” mode studied thus far. The free energy landscape for this new hybridization mode is plotted with respect to the end-to-end distances in Figure 4.9. The interaction zone of the shear mode (~ 28 to 40° where strand hybridization is favored) is much thinner than that of the zip mode (~ 2 to 26°), and the free energy minimum is also much shallower than the zip mode. For 4b connections, the free energy gain for the sheer mode is small since it would not feel the merit of the confinement effect in its reaction zone. When the overhang length is increased, the confinement will push the

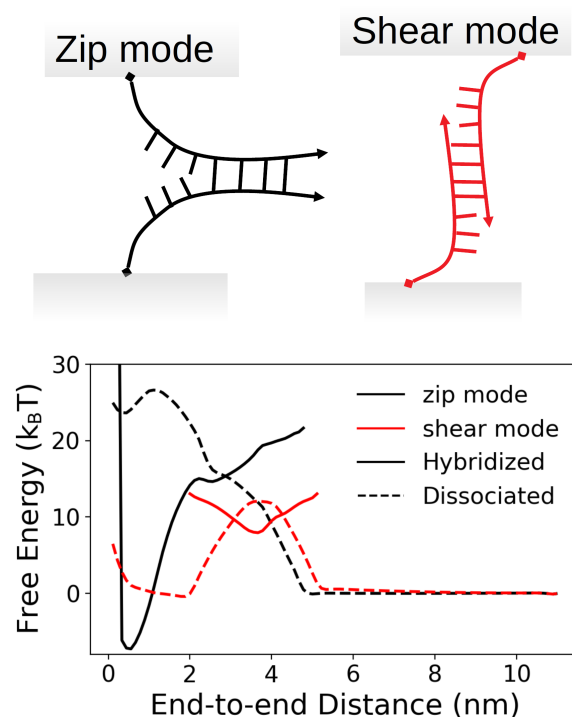


Figure 4.9: Free energy landscape of two different binding modes. The free energies of the hybridized and dissociated sub-ensembles are plotted separately.

free energy minimum down and make the hybridized states more favored.

4.3.3 Bare hinge and total free energy of the system

To calculate the total free energy landscape of the system, we simulated the most used hinge in previous experiments, which is the hinge with 2 bases/16 bases single-stranded DNA linkers at the vertex. The free energy landscape reconstructed with weighted histogram analysis method from the hinge angle distribution in each window is shown in Figure 4.10. Due to the large free energy barrier, the simulation results for extremely small angles are hard to get, and therefore a fitting result is used instead for calculating the total energy of the system. The equilibrium hinge angle from the simulation is 80° , which perfectly reproduces the experimental value. The large free energy difference between the small angle state and the equilibrium angle indicates

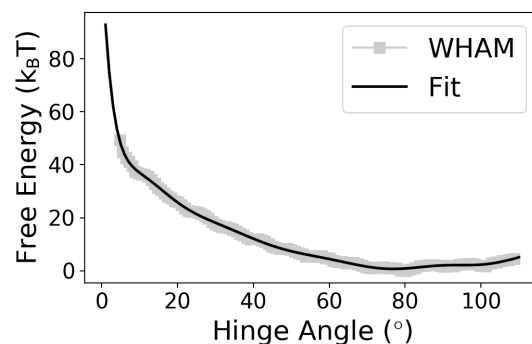


Figure 4.10: Umbrella sampling for the bare hinge. Free energy landscape of bare hinge design with 2 bases / 16 bases connection at vertex. The free energy landscape shows a minimum at 80°, which agrees with the experimental results.

that closed state is barely seen for the bare hinge, but the value of the free energy difference is much larger than the previous calculated value from the TEM image(32). This may be due to the inadequate sample number in experiments.

As both the free energy of overhangs and the free energy of the bare hinge are obtained, the total free energy landscape of the system can be calculated by summing the two free energy landscapes up, as shown in the upper row of Figure 4.11. Because of the high free energy at small hinge angle for the 1st connection, even the hinge design with 30 connections will not exhibit closed states under high ion concentration. When the overhangs are attached to the hinge, the equilibrium hinge angle of the open states also shifts to smaller hinge angle because of the entropy force exerted by the overhangs.

However, there can be deformations in the hinge arm, therefore the way of calculating the free energy landscape of the system may need to take the possible deformation into account. The exact deformation of hinge arm is hard to predict, and we assume that the deformation near the vertex may change the free energy landscape of the first connection to a landscape close to the second one. The total free energy profile after the deformation correction is shown in the lower row of Figure 4.11. It is obvious that after the correction, the closed states are preferred

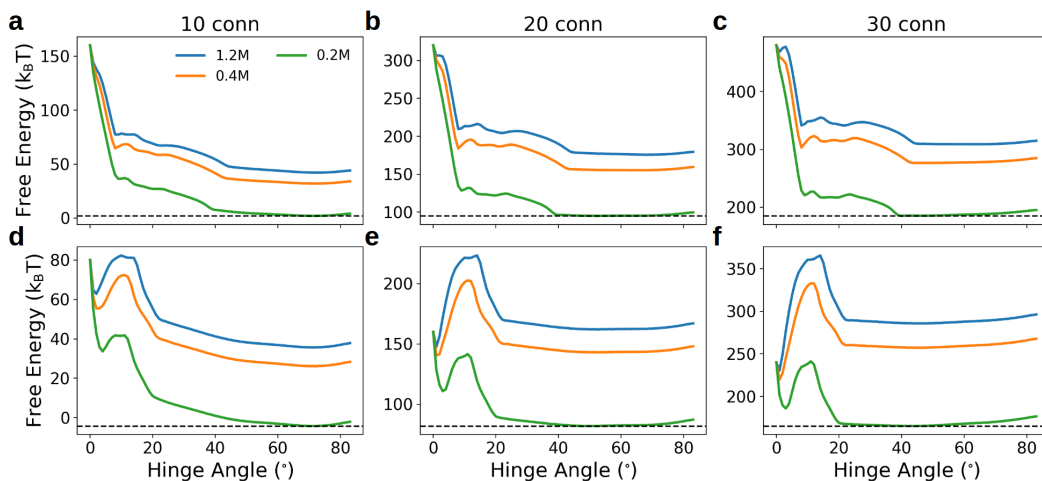


Figure 4.11: Total free energy of the system. The total free energy is calculated as the sum of the bare hinge free energy and overhang free energy with 10 connection at 10 different connection points (**a-c**) and no connection at the first but 2 at the second connection point (**d-f**)

for designs with more overhangs at higher ion concentration, which agree with the experimental results.

4.4 Discussion

From the free energy landscape of 4b connections, the overhangs can be divided into four groups:

1. the 1st connection: initiator of the closing process, will pull the two arms together towards angles near fully hybridized region of other overhangs.
2. the 2nd and 3rd connection: inhibitor of the closing process, will have strong steric repulsion interaction at small hinge angle.
3. the 4th to 6th connection: stabilizers of the closing process, will hybridize at small hinge angle and bind two hinge arms together regardless of ion concentration.
4. the 7th to 10th connection: ion concentration sensors that response to the salt stimuli,

tend to hybridize at high ion concentration but will stay in dissociated states at low ion concentration.

With the free energy landscape of the four different kinds of overhangs, we can figure out the detailed mechanism of how the hinge switch to the closed states when changing the ion concentration. Furthermore, different free energy landscapes can be obtained through changing the distribution of overhangs. If there are more overhangs located between the 4th and the 6th connection point, the free energy minimum for the closed state are much deeper, resulting in structures stable at the closed states regardless of ion concentration while more overhangs accumulated near the vertex will enhance the stability of open states regardless of the ion concentration. When overhangs are accumulated farther than the 7th connection point, the hinge will have a sharp actuation response curve when changing ion concentration. Besides, using heterogeneous design of overhangs may further enhance certain properties including the stability of hinge in the closed states and the sharpness of actuation response.

Compared to the two-state statistical model we proposed in our previous paper, which use two fitting parameters to approximate the confinement, the relation between the actuation response and the design parameters are relatively weaker and several sets of preliminary experimental results are also needed for actuation response prediction. This work implements coarse-grained modeling based on several assumptions in the statistical model to give more accurate description of the mechanics the actuation and give predictions without preliminary data to save time and resources.

However, in our simulations, there are still some defects that may cause deviation of the simulation from the experiments. 1) In simulations, we use Na^+ instead of Mg^{2+} . We could only tell how the ion concentration affect the free energy profile based on the hybridization free energy gain under different ion concentrations. 2) For the umbrella sampling of the bare hinge, the order parameter change is caused by the pulling force from the overhangs, but we treat them as harmonic potentials applied on the center of mass. 3) There can be deformations in the hinge

arm, therefore the way of calculating the free energy landscape of the system may need to take the possible deformation into account. The free energy landscape without the first connection shows the same trend as experimental results.

4.5 Conclusion

The work presented here gives relatively more accurate descriptions of the hinge energetics and mechanics under different ion concentrations and giving molecular insights into confined hybridization of DNA strands. We proposed a computational strategy for efficiently computing free energy landscapes of the actuation process through splitting the system into bare hinge and overhangs, which can significantly leverage the computational burden of extra large systems like the DNA origami hinge. From the free energy landscape of single pair of overhangs, we find out that the dominant states will change from dissociated states to hybridized states when decreasing the hinge angle. Besides, confinement from the hinge arms will affect the shape of the free energy landscape mainly through the repulsion plane effect and the angular effect, where the first one will change the energy barrier width, and the second one will change the height of the barrier. Overhangs with different sequence will also give different free energy landscape. Tail length will affect the From our results, we could see that unlike the typical free energy landscape of DNA strand hybridization in zipping mode(29), the special confinement will add a barrier to the landscape an the barrier can also be tunned by the confinement and the . When combining the free energy landscape of overhangs together with the free energy landscape of bare hinge, which is obtained from umbrella sampling simulations, the total free energy landscape still give prediction on the actuation response of the system. In this way, we link the actual design parameter, the distribution and the sequence design of the overhangs, to actuation response, which gives more straightforward instructions on optimizing the design compared to our previous statistical model.

Implementing short DNA overhangs as a trigger under ion concentration enables delicate

control over the actuation response since the distribution and sequence design of overhangs can vary in a relative larger range. Therefore, such design can be applied to a variety of DNA nanodevices that require fast conformational change response under external stimuli. In the future, exploring the behavior of overhangs under different geometry of confinement and overhang sequence design will greatly extend the application of such design strategy.

4.6 Methods

To recover the free energy landscape from the hinge angle distribution of simulations, 2D weighted histogram analysis method (WHAM) is implemented. Consider the process as an umbrella sampling with two order parameters, the hinge angle θ and the number of base pairs formed ξ , and the bias potentials are the harmonic restraint $V_k(\theta) = \frac{1}{2}(\theta - \theta_0)^2$ for the hinge angle and the bias $B_k(\xi)$ for the number of base pairs formed. Here $B_k(\xi)$ is a conditional function specifying the bias factor for each hybridization states.

$$B_k(\xi) = \begin{cases} b_{k,\xi_j} & \text{if } \xi = \xi_j, j = 0, 1, 2, \dots, 6 \\ 0 & \text{otherwise.} \end{cases} \quad (4.1)$$

For the biased simulation, the probability of state k , $\rho_k^{(b)}(\theta, \xi)$ will be proportional to $B_k(\xi)e^{-[U_0(\theta,\xi)+V_k(\theta)]/k_B T}$, where $U_0(\theta, \xi)$ is the origin free energy landscape. Therefore, the probability can be written as:

$$\begin{aligned} \rho_k^{(b)}(\theta, \xi) &= \frac{B_k(\xi)e^{-[U_0(\theta,\xi)+V_k(\theta)]/k_B T}}{\int B_k(\xi)e^{-[U_0(\theta,\xi)+V_k(\theta)]/k_B T} d\theta d\xi} \\ &= \frac{B_k(\xi)e^{-U_0(\theta,\xi)/k_B T} e^{-V_k(\theta)/k_B T}}{\int e^{-U_0(\theta,\xi)d\theta d\xi}} \times \frac{\int e^{-U_0(\theta,\xi)d\theta d\xi}}{\int B_k(\xi)e^{-[U_0(\theta,\xi)+V_k(\theta)]/k_B T} d\theta d\xi} \\ &= \rho_k(\theta, \xi) B_k(\xi) e^{-V_k(\theta)/k_B T} \times \frac{\int e^{-U_0(\theta,\xi)d\theta d\xi}}{\int B_k(\xi)e^{-[U_0(\theta,\xi)+V_k(\theta)]/k_B T} d\theta d\xi} \\ &= \frac{\rho_k(\theta, \xi) B_k(\xi) e^{-V_k(\theta)/k_B T}}{\langle B_k(\xi) e^{-V_k(\theta)/k_B T} \rangle_{U_0}}. \end{aligned} \quad (4.2)$$

Define $\left\langle B_k(\xi)e^{-V_k(\theta)/k_B T} \right\rangle_{U_0}$ as $e^{-F_k/k_B T}$, so the probability of state k without bias is:

$$\rho_k(\theta, \xi) = \rho_k^{(b)}(\theta, \xi) \left[\frac{e^{(V_k(\theta)-F_k)/k_B T}}{B_k(\xi)} \right]. \quad (4.3)$$

The $\frac{e^{(V_k(\theta)-F_k)/k_B T}}{B_k(\xi)}$ term is defined as the bias correction factor $f_i(\theta, \xi)$. Notably, from the definition of $B_k(\xi)$ (Eq. 2), one simulation run that goes through all the hybridization states (ξ) is considered as one biased simulation, therefore the bias correction factor should be the same for hinge angle distributions with the same bias potential $V_k(\theta)$ regardless of the hybridization status.

In the iteration process, the bias correction factor is updated with the estimated probability distribution:

$$e^{-F_k/k_B T} = \sum_i \left[e^{-V_{i,k}/k_B T} \sum_{\xi} \rho_{i,\xi} b_{k,\xi} \right], \quad (4.4)$$

where i is the i^{th} bin of hinge angle in WHAM. Then the probability distribution is updated through Equation 4 with the updated F_k . When the difference between the updated and the origin probability distribution is smaller than the threshold, the iteration process is terminated.

4.7 Acknowledgements

Chapter 4, in full is currently being prepared for submission for publication of the material. Shi Ze; Arya, Gaurav. The dissertation author was the primary investigator and author of this material.

4.8 Appendix

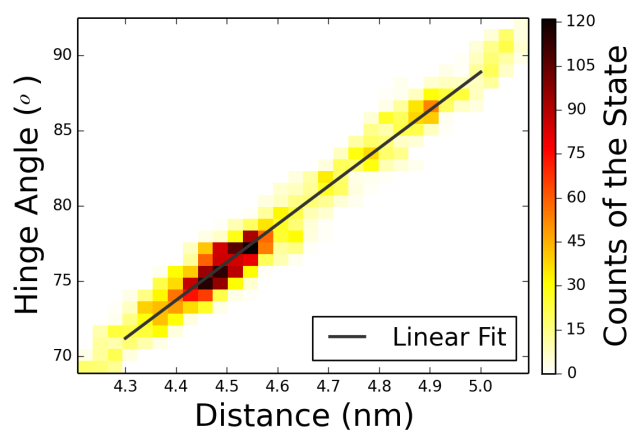


Figure 4.12: Correlation between hinge angle and distance between center of the hinge arms. The two order parameter shows good correlation.

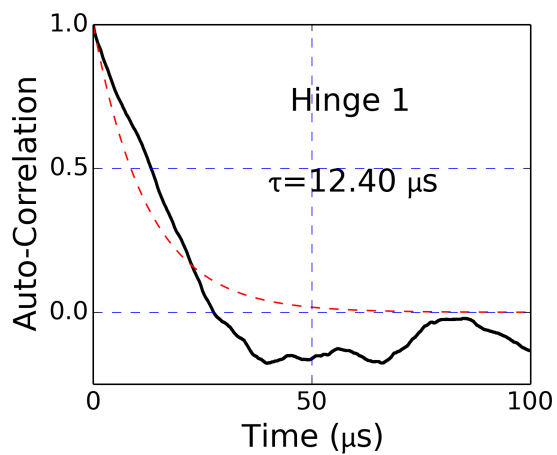


Figure 4.13: Relaxation time of the bare hinge. The conformations of the bare hinge can be well sampled in a relative short time scale.

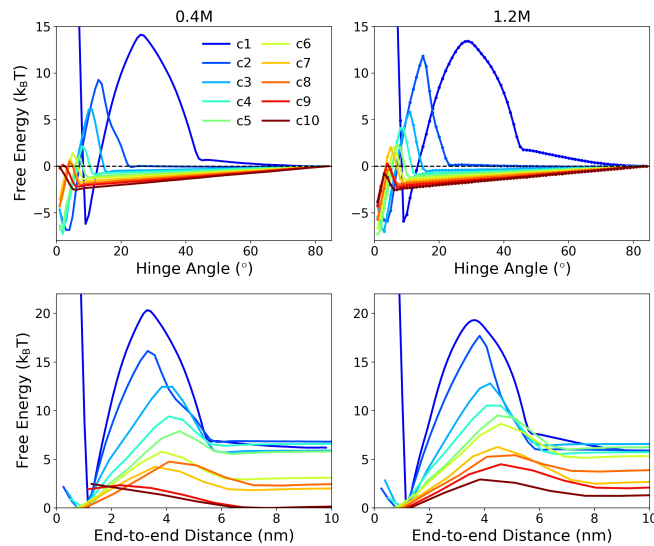


Figure 4.14: Total free energy landscape of overhang strands with 4 complementary bases under 0.4M and 1.2M Na^+ ion concentrations.

4.9 References

- [1] J. Bath and A. A. J. Turberfield, “DNA nanomachines,” *Nat. Nanotechnol.*, vol. 2, pp. 275–284, may 2007.
- [2] T. Omabegho, R. Sha, and N. C. Seeman, “A Bipedal DNA Brownian Motor with Coordinated Legs,” *Science*, vol. 324, pp. 67–71, apr 2009.
- [3] J. Pan, F. Li, T.-G. Cha, H. Chen, and J. H. Choi, “Recent progress on DNA based walkers,” *Curr. Opin. Biotechnol.*, vol. 34, pp. 56–64, aug 2015.
- [4] H. Yan, X. Zhang, Z. Shen, and N. C. Seeman, “A robust DNA mechanical device controlled by hybridization topology,” *Nature*, vol. 415, pp. 62–65, jan 2002.
- [5] C. E. Castro, H.-J. Su, A. E. Marras, L. Zhou, and J. Johnson, “Mechanical design of DNA nanostructures,” *Nanoscale*, vol. 7, pp. 5913–21, apr 2015.
- [6] A. Kuzyk, R. Schreiber, H. Zhang, A. O. Govorov, T. Liedl, and N. Liu, “Reconfigurable 3d plasmonic metamolecules,” *Nature materials*, vol. 13, no. 9, p. 862, 2014.
- [7] A. Kuzuya, Y. Sakai, T. Yamazaki, Y. Xu, and M. Komiyama, “Nanomechanical DNA origami ‘single-molecule beacons’ directly imaged by atomic force microscopy,” *Nat. Commun.*, vol. 2, no. 1, pp. 448–449, 2011.

- [8] H. Gu, W. Yang, and N. C. Seeman, “DNA Scissors Device Used to Measure MutS Binding to DNA Mis-pairs,” *J. Am. Chem. Soc.*, vol. 132, pp. 4352–4357, mar 2010.
- [9] S. Ranallo, C. Prévost-Tremblay, A. Idili, A. Vallée-Bélisle, and F. Ricci, “Antibody-powered nucleic acid release using a dna-based nanomachine,” *Nature communications*, vol. 8, p. 15150, 2017.
- [10] B. Yurke, A. J. Turberfield, A. P. Mills, F. C. Simmel, and J. L. Neumann, “A DNA-fuelled molecular machine made of DNA,” *Nature*, vol. 406, pp. 605–608, aug 2000.
- [11] P. Ketterer, E. M. Willner, and H. Dietz, “Nanoscale rotary apparatus formed from tight-fitting 3D DNA components,” *Sci. Adv.*, vol. 2, no. 2, pp. e1501209–e1501209, 2016.
- [12] T. Gerling, K. F. Wagenbauer, A. M. Neuner, and H. Dietz, “Dynamic DNA devices and assemblies formed by shape-complementary, non-base pairing 3D components,” *Science*, vol. 347, pp. 1446–1452, mar 2015.
- [13] Y. Kamiya and H. Asanuma, “Light-driven dna nanomachine with a photoresponsive molecular engine,” *Accounts of chemical research*, vol. 47, no. 6, pp. 1663–1672, 2014.
- [14] A. Kuzyk, M. J. Urban, A. Idili, F. Ricci, and N. Liu, “Selective control of reconfigurable chiral plasmonic metamolecules,” *Science advances*, vol. 3, no. 4, p. e1602803, 2017.
- [15] S. Modi, S. M. G., D. Goswami, G. D. Gupta, S. Mayor, and Y. Krishnan, “A DNA nanomachine that maps spatial and temporal pH changes inside living cells,” *Nat. Nanotechnol.*, vol. 4, pp. 325–330, may 2009.
- [16] E. Kopperger, J. List, S. Madhira, F. Rothfischer, D. C. Lamb, and F. C. Simmel, “A self-assembled nanoscale robotic arm controlled by electric fields,” *Science*, vol. 359, no. 6373, pp. 296–301, 2018.
- [17] S. Lauback, K. R. Mattioli, A. E. Marras, M. Armstrong, T. P. Rudibaugh, R. Sooryakumar, and C. E. Castro, “Real-time magnetic actuation of dna nanodevices via modular integration with stiff micro-levers,” *Nature communications*, vol. 9, no. 1, p. 1446, 2018.
- [18] M. Siavashpouri, C. H. Wachauf, M. J. Zakhary, F. Praetorius, H. Dietz, and Z. Dogic, “Molecular engineering of chiral colloidal liquid crystals using dna origami,” *Nature materials*, vol. 16, no. 8, p. 849, 2017.
- [19] W. Bae, K. Kim, D. Min, J.-K. Ryu, C. Hyeon, and T.-Y. Yoon, “Programmed folding of dna origami structures through single-molecule force control,” *Nature communications*, vol. 5, p. 5654, 2014.
- [20] L. Li, X. Tian, Z. Dong, L. Liu, O. Tabata, and W. J. Li, “Manipulation of dna origami nanotubes in liquid using programmable tappingmode atomic force microscopy,” *IET Micro & Nano Letters*, vol. 8, no. 10, pp. 641–645, 2013.

- [21] A. E. Marras, Z. Shi, M. G. Lindell, R. A. Patton, C.-M. Huang, L. Zhou, H.-J. Su, G. Arya, and C. E. Castro, “Cation-Activated Avidity for Rapid Reconfiguration of DNA Nanodevices,” *ACS Nano*, vol. 12, pp. 9484–9494, sep 2018.
- [22] P. Šulc, F. Romano, T. E. Ouldridge, L. Rovigatti, J. P. K. Doye, and A. A. Louis, “Sequence-dependent thermodynamics of a coarse-grained DNA model,” *J. Chem. Phys.*, vol. 137, p. 135101, oct 2012.
- [23] T. E. Ouldridge, A. a. Louis, and J. P. K. Doye, “Structural, mechanical, and thermodynamic properties of a coarse-grained DNA model,” *J. Chem. Phys.*, vol. 134, p. 085101, feb 2011.
- [24] P. Šulc, T. E. Ouldridge, F. Romano, J. P. K. Doye, and A. A. Louis, “Simulating a burnt-bridges DNA motor with a coarse-grained DNA model,” *Nat. Comput.*, vol. 13, pp. 535–547, dec 2014.
- [25] C. Matek, T. E. Ouldridge, A. Levy, J. P. K. Doye, and A. A. Louis, “DNA Cruciform Arms Nucleate through a Correlated but Asynchronous Cooperative Mechanism,” *J. Phys. Chem. B*, vol. 116, pp. 11616–11625, sep 2012.
- [26] J. S. Schreck, T. E. Ouldridge, F. Romano, P. Šulc, L. P. Shaw, A. A. Louis, and J. P. Doye, “DNA hairpins destabilize duplexes primarily by promoting melting rather than by inhibiting hybridization,” *Nucleic Acids Res.*, vol. 43, pp. 6181–6190, jul 2015.
- [27] F. Romano, A. Hudson, J. P. K. Doye, T. E. Ouldridge, and A. A. Louis, “The effect of topology on the structure and free energy landscape of DNA kissing complexes,” *J. Chem. Phys.*, vol. 136, p. 215102, jun 2012.
- [28] D. C. Khara, J. S. Schreck, T. E. Tomov, Y. Berger, T. E. Ouldridge, J. P. K. Doye, and E. Nir, “DNA bipedal motor walking dynamics: an experimental and theoretical study of the dependency on step size,” *Nucleic Acids Res.*, pp. 1–9, dec 2017.
- [29] S. R. Tee and Z. Wang, “How Well Can DNA Rupture DNA? Shearing and Unzipping Forces inside DNA Nanostructures,” *ACS Omega*, vol. 3, no. 1, pp. 292–301, 2017.
- [30] Z. Shi, C. E. Castro, and G. Arya, “Conformational dynamics of mechanically compliant dna nanostructures from coarse-grained molecular dynamics simulations,” *ACS nano*, vol. 11, no. 5, pp. 4617–4630, 2017.
- [31] A. P. Alivisatos, K. P. Johnsson, X. Peng, T. E. Wilson, C. J. Loweth, M. P. Bruchez, and P. G. Schultz, “Organization of ‘nanocrystal molecules’ using DNA,” *Nature*, vol. 382, pp. 609–611, aug 1996.
- [32] A. E. Marras, Z. Shi, M. G. Lindell, R. A. Patton, C.-M. Huang, L. Zhou, H.-J. Su, G. Arya, and C. E. Castro, “Cation-Activated Avidity for Rapid Reconfiguration of DNA Nanodevices,” *ACS Nano*, vol. 0, p. acsnano.8b04817, 9 2018.

Chapter 5

Additional Studies

5.1 Mechanics of the Holliday junction

The Holliday junction is one of the most important structures in DNA origami. For building analytical models of DNA-origami mechanics based on continuum approaches, the stiffness and the rupture force of the Holliday junction are important parameters. In this section, these two parameters are estimated through all-atom molecular dynamics simulation based on force-deformation behavior of Holliday junction.

Methods

All simulations were carried out using the AMBER ff99bsc0 force field (1). The initial configuration was generated from caDNAo design with two long, straight scaffold strands with sequence TTTTGGCAGATATGT and two complementary staple strands connected together (Figure 5.1). Umbrella sampling simulations were performed to calculate the potential of mean force for the stretching of the thus-assembled Holliday junction with respect to the distance between the backbone. In each window, a biased harmonic potential centered at different locations along the stretching reaction coordinate was implemented. The biased MD simulations

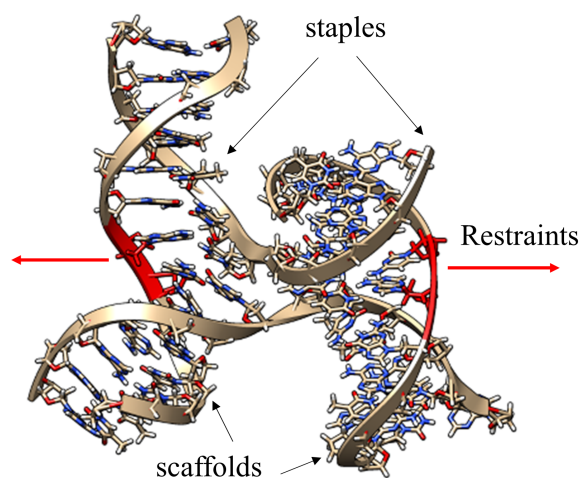


Figure 5.1: Stretching the Holliday junction. Harmonic restraints were applied according to the distance between the DNA backbones. The two straight strands are defined as scaffold strands with sequence TTTTGGCAGATATGT, and the two strands connecting the scaffold together are defined as staples. The backbone of the two center bases on the scaffold are marked in red. Harmonic restraints are applied on the center of mass of each backbone group, and the minimum of the restraint potential profile is moved in the direction shown by the red arrow.

consisted of initial minimization and equilibration followed by 101 individual 200ps-long MD simulations with restraints applied on two backbone groups in the middle of the Holliday junction (Figure 5.1). The salt concentration is 0.2M. The minimum of the restraint potential was moved along the order parameter, the distance between two backbone groups, for different simulations.

Results

The resulting free energy obtained via weighted histogram analyses is shown in Figure 5.2, with a series of snapshots from several specific MD simulations as insertions. Figure 5.2a shows the dissociation of the first base pair of the two stretched base pairs, early in the stretching process, and this dissociation event appears as the first peak in the free energy profile. Till the stretching distance increases to the point of the second peak, the second stretched base pair begins to dissociate. From this point, the backbone connecting the stretched bases and adjacent bases on the scaffold strand are stretched until the distance between backbone groups reach the point of

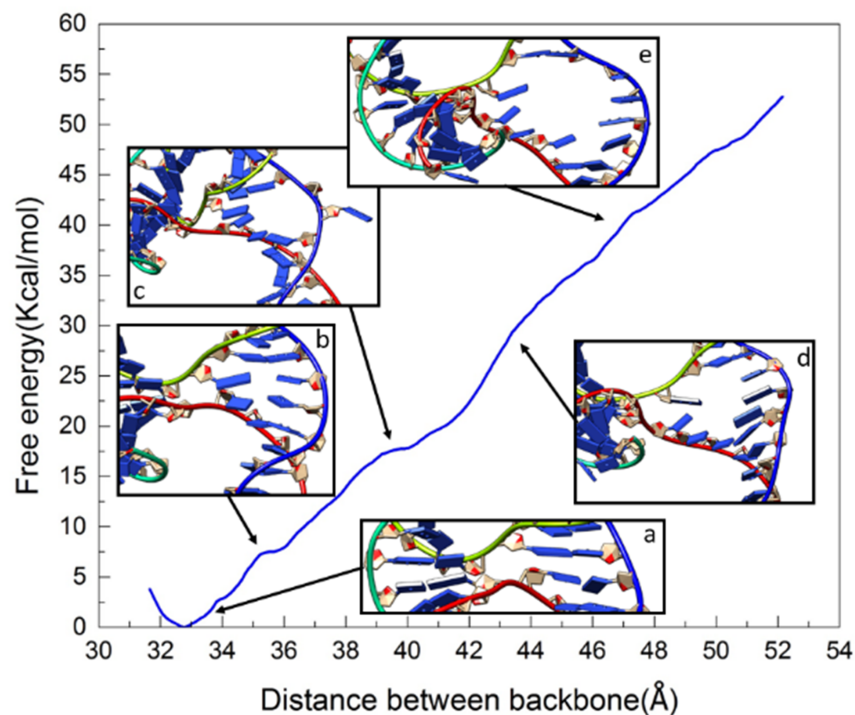


Figure 5.2: Potential mean force and five representative snapshot for peak position. The corresponding backbone group distances for insertions are: **a** 33.8Å; **b** 35.6Å; **c** 40Å; **d** 45Å; **e** 47Å.

the forth peak, as shown in Figure 5.2c, where the adjacent base pairs on the scaffold begin to fall apart. Eventually, upon stretching by more than 15Å, 4 base pairs fall apart.

To determine the base-pairing states, hydrogen bond (H-bond) analysis was performed for each MD trajectory. The distance cutoff chosen for the bond was 3.0Å, and the angle cutoff was 135°. To compare with the free energy profile, a first derivative of the free energy, which effectively gives the stretching force is also plotted. At distances smaller than the distance corresponding to an equilibrated system, the Holliday junction is compressed rather than stretched, resulting in a negative stretching force. When the distance increases, a larger force is required to stretch the base pair apart, and the maximum stretching force obtained from this simulation is roughly 385.2pN.

The H-bonds with binding rate greater than 0.1 are counted as valid. Only the emergence

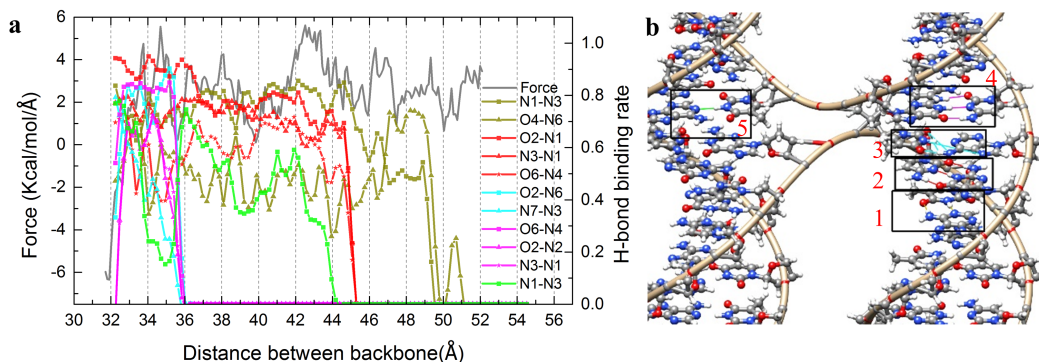


Figure 5.3: H-bond binding rate in the stretching process. **a:** Stretching force derived from the free energy profile and the H-bond binding rates for 5 base pairs marked in **b**. **b:** 5 base pairs involving the generating and expiring of H-bonds. Group 1 corresponds to the deep yellow plots in **a**, and group 2, 3, 4, and 5 correspond to the red, cyan, magenta, and green plots, respectively.

and disappearance of H-bonds are plotted in Figure 5.3a. The H-bonds can be categorized into 5 groups based on the base pair involved (Figure 5.3b). From the equilibrium position, which is 32.8\AA , to 36\AA , the H-bonds in group 3 and group 4 are broken, which corresponding to the configuration shown in Figure 5.2b, where the two middle base pairs fall apart. Interestingly, the H-bond in group 5, which is on the other side of the Holliday junction, also begins to dissociate. This indicate that there is a competition between the two sides when stretched. Since there is one less H-bonds for A-T base pair (group 3 and group 5) than the G-C base pair (group 4 and the base pair below group 5), the competition will only happen between the two A-T base pairs. In this case, group 1 H-bonds break apart first as the group 3 are fully dissociated, therefore the two staples are relaxed and the H-bond in group 5 recovered after the peak in potential mean force at 35.6\AA .

When the junction is further stretched, the H-bonds in group 2 are broken, which corresponds to another peak in the free energy plot (Fig 5.2d). For the process in between, the backbones are stretched, providing the rising background of the free energy profile, thus pulling the base pair of group 5 apart. Similarly, if one keeps stretching, the H-bonds in group 1 will dissociate where a sharp peak in the force plot occurs.

Since the binding rate of the H-bonds all drops in a sudden after a peak in the force value, the stretching process then can be divided into two parts: DNA backbone stretching and the dehybridization of Watson-Crick base pairs. As in most coarse-grained DNA models, the backbone can be modeled as a harmonic spring, and the H-bonds between Watson-Crick base pairs are extra local energy barriers. However, when a base pair breaks, the double-helical structure is destroyed, adding extra length to the spring. The free energy profile is affected by the number of base pairs formed.

To conclude, a free energy profile of the Holliday junction stretching process was obtained from umbrella sampling all-atom MD simulations. The force required to deform the Holliday junction is 385.2 pN, indicating the strength of the fundamental components of DNA origami. The H-bond analysis revealed the competition between the two A-T base pairs on the two helices at the beginning of the deformation processes. Besides, the H-bond binding rate change also indicates that the free energy profile can be divided into two parts: one is the harmonic spring potential for the DNA backbone, and the hybridization local free energy barrier.

5.2 Modeling of a DNA crystal

Crystals are structures with a translational periodicity that can be characterized with X-ray diffraction. Like in other disciplines, biologists also want to create crystalline structures composed of biomolecules because of their many potential applications. In 2006, Paukstelis (2) proposed a three-dimensional DNA crystal self-assembled from DNA tiles (Figure 5.4) in a hexagonal lattice.

We built a NAB (Nucleic Acid Builder, a high-level programming environment for nucleic acids) script and simulated the structure with all-atom molecular dynamics simulations with the AMBER ff99bsc0 force field (1) as non-Watson Crick interactions are present in the crystal. After relaxation and equilibration, the relaxed structure is shown in Figure 5.4b. The simulation results

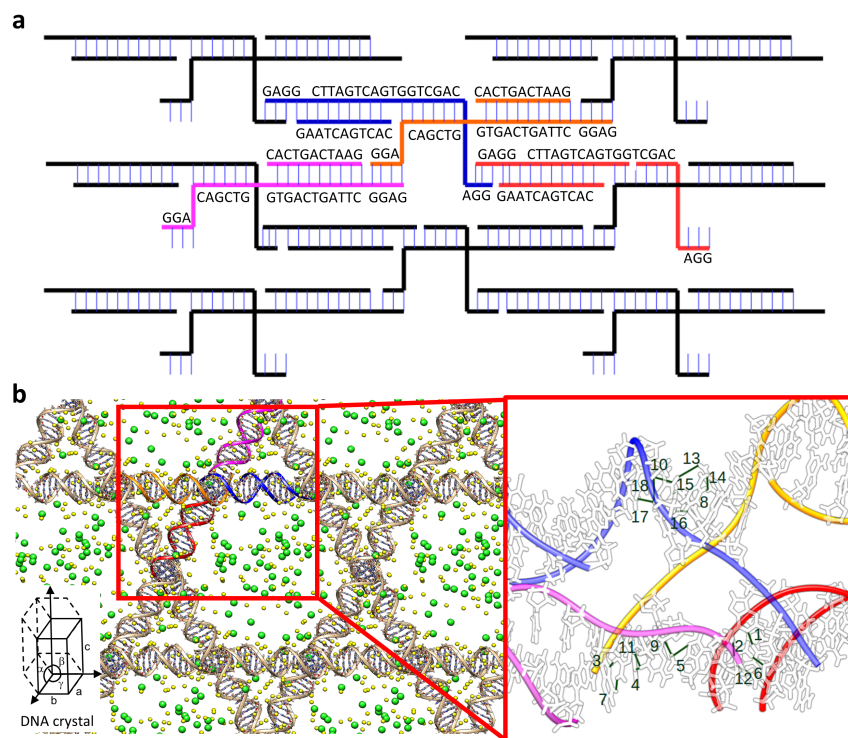


Figure 5.4: Assembly of DNA tiles into a 3D DNA crystal. **a:** DNA sequence and connections of the underlying building block of the DNA crystal. The different layers are represented in different lines. The colored strands represent a unit tile. **b:** A six-layer DNA crystal model. The unit cell parameters are: $a = 109.91$ nm, $b = 109.91$ nm, $c = 56.23$ nm, $\alpha = 90.0^\circ$, $\beta = 90.0^\circ$, $\gamma = 120.0^\circ$. H-bonds other than Watson-Crick base pairing in a connection between adjacent layers are numbered from the highest binding fraction to the lowest one.

suggest that the crystal remains stable at high monovalent salt conditions and exhibits only small structural fluctuations.

We further analyzed hydrogen bonding within DNA crystal. Apart from Watson-Crick base-pairing interactions, there are several other kinds of interactions in DNA. As shown in Figure 5.5, antiparallel G-G WC-Hoogsteen interaction (Figure 5.5b H-bond 3 and 7), parallel G-G WC-Hoogsteen interaction (Figure 5.5c, H-bond 4 and 11), parallel A-A WC interaction (Figure 5.5d, H-bond 5 and 9), parallel G-G sugar-edge interaction (Figure 5.5e, H-bond 6 and 12), and parallel A-A WC interaction (Figure 5.5f, H-bond 1 and 2) are also observed. Apart from the above interactions, there are also H-bonds that do not belong to certain interactions between

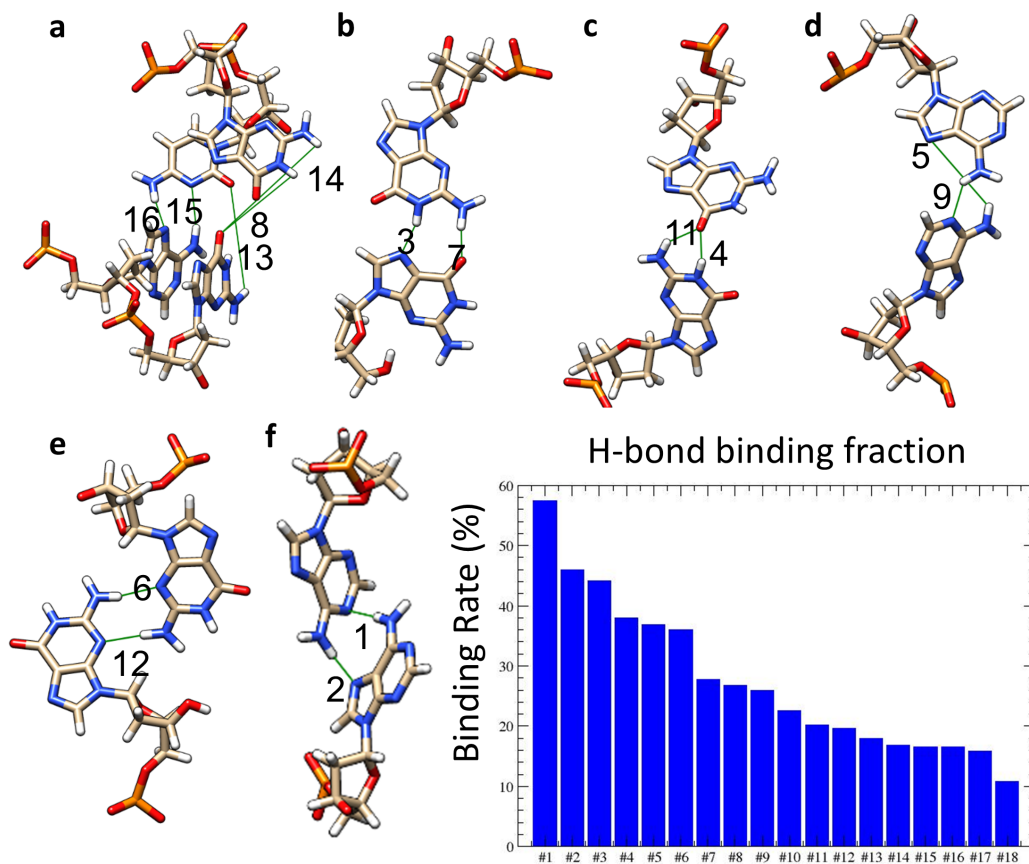


Figure 5.5: H-bonds in DNA crystal. **a-f** H-bonds for different base pairs. All the binding fraction of the non-WC H-bonds in a 5ns MD simulation are presented in chart **g**.

DNA, like H-bond 8 and 13-16, which are generally of low binding fractions. In the future, we would like to simulate proteins within such crystals for potential applications in catalysis.

5.3 References

- [1] D. A. Case, J. T. Berryman, R. M. Betz, D. S. Cerutti, T. E. Cheatham Iii, T. A. Darden, R. E. Duke, T. J. Giese, H. Gohlke, A. W. Goetz, and Others, “AMBER 2015,” *Univ. California, San Fr.*, 2015.
- [2] P. J. Paukstelis, “Three-dimensional DNA crystals as molecular sieves.,” *J. Am. Chem. Soc.*, vol. 128, pp. 6794–5, may 2006.

Chapter 6

Concluding remarks

6.1 Summary

This dissertation has laid out a possible plan for research and development efforts needed to build develop simple design rules based on molecular-scale models for predicting the conformational dynamics and actuation of mechanically compliant DNA nanostructures. As part of this plan, we first showed that molecular-scale models and simulations can indeed reproduce the dynamics and mechanical properties of such DNA nanostructures, and then used the validated models and simulations to study and propose design rules for predicting conformations and actuation responses. In particular, we proposed a force-balance approach that promises to give rapid predictions of the mechanical property of DNA nanostructures based on the force-deformation characteristics of its components. For structures involving hybridization and dissociation of DNA strands, such as those used in salt-based actuation of hinges, we proposed a method for computing the free energy landscape of complex structures involving large-scale conformational changes as well as multiple small-scale overhang hybridization processes to predict how the sequence of such overhangs affects the actuation response of the devices. Both these approaches provided good agreement with experimental results and can thus serve as part of a design tool to provide

valuable guidance on future design of complex mechanical DNA nanostructures.

Although the two methods look promising, a database for the mechanical properties of the various components of DNA devices is also necessary to provide rapid feedback on the mechanical properties of large sets of mechanical designs without the need to perform brute-force simulations for each design that can become computationally prohibitive. Therefore, to broaden the application of DNA nanotechnology design tools, more work is required to characterize the large array of possible mechanical components that may go into the final design.

6.2 Directions for future research

6.2.1 Database of DNA mechanical components

In Chapter 2, a force-balance-based method for providing efficient predictions of the dynamics of DNA nanostructures was introduced. However, we only presented the force-deformation curves of the bare DNA hinge and five spring designs. To enable predictions of a much broader variety of designs, a database of force-deformation curves of many more mechanical components is necessary. In the future, building such type of database should greatly save time in designing DNA nanodevices and sensors where mechanical responses are required. Besides, comparing different force-deformation curves in the database can also reveal how the DNA nanostructures can be actuated from one conformation to another by adding or removing DNA strands. Furthermore, simple models inspired by classical mechanics can also be built if larger data sets are obtained, enabling researchers to develop simple design rules for designing mechanical devices based on DNA.

6.2.2 Free energy landscape of DNA overhang connections

In Chapter 3, several free energy landscapes of short overhang connections were presented. However, compared to the widely used DNA linker in DNA nanotechnology, the number of designs investigated is still quite limited. In the future, longer overhangs and overhangs under different confinement can also be studied to enrich our database of dynamic DNA nanostructure design.

6.2.3 Newer actuation strategies for DNA nanodevices

Apart from the above two main projects carried out here, interactions such as the base-stacking interaction between blunt ends of double-stranded DNA can also be incorporated into the design database. Other stimuli like light or magnetic field can also be added into the database for design tool with wider applications.

6.2.4 New mechanisms for mechanical DNA nanomachines

Compared to design concepts in macroscopic structure design, mechanisms for DNA nanomachine are still limited. Through computer simulations, which involve much lower costs compared to experiments involving folding of super-large mechanical nanostructures, searching for new mechanisms for mechanical DNA nanomachines would save more time and would be easier to optimize.

6.2.5 Optimized design tools of dynamic DNA nanodevices

Till now, most of the design tools are based on concepts of double-stranded DNA, while real-life applications are more interested in the end-goals or functions such as size, shape, or dynamics. For more complicated dynamic DNA nanodevices, design tools with a top-down

approach and incorporated multiple design strategy will be a better choice for mechanical DNA nanomachine.